Performance Evaluation of a Micro Gas Turbine Centrifugal Compressor Diffuser

by
David Schabort Krige

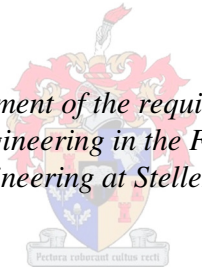

Thesis presented in fulfilment of the requirements for the degree of Masters of Science in Engineering in the Faculty of Mechanical and Mechatronic Engineering at Stellenbosch University

Supervisor: Prof T.W. von Backström
Co-supervisor: Dr. S.J. van der Spuy

March 2013

DECLARATION

By submitting this thesis electronically, I declare that the entirety of the work contained therein is my own, original work, that I am the sole author thereof (save to the extent explicitly otherwise stated), that reproduction and publication thereof by Stellenbosch University will not infringe any third party rights and that I have not previously in its entirety or in part submitted it for obtaining any qualification.

Date: March 2013

ABSTRACT

Performance Evaluation of a Micro Gas Turbine Centrifugal Compressor Diffuser

D. S. Krige

Department of Mechanical and Mechatronic Engineering, Stellenbosch University, Private Bag X1, Matieland 7602, South Africa
Thesis: MSc. Eng. (Mech)

March 2013

Micro gas turbines used in the aerospace industry require high performance with a compact frontal area. These micro gas turbines are often considered unattractive and at times impractical due to their poor fuel consumption and low cycle efficiency. This led to a joint effort to investigate and analyze the components of a particular micro gas turbine to determine potential geometry and performance improvements. The focus of this investigation is the radial vaned diffuser which forms part of a centrifugal compressor. The size of the diffuser is highly constrained by the compact gas turbine diameter. The micro gas turbine under consideration is the BMT 120 KS. The radial vaned diffuser is analyzed by means of 1-D and 3-D (CFD) analyses using CompAero and FINE^{TM}/Turbo respectively. The aim is to design a diffuser that maximizes the total-to-static pressure recovery and mass flow rate through the compressor with minimal flow losses. An experimental test facility was constructed and the numerical computations were validated against the experimental data. Three new diffusers were designed, each with a different vane geometry. The static-to-static pressure ratio over the radial diffuser was improved from 1.39 to 1.44 at a rotational speed of 120 krpm. The static pressure recovery coefficient was improved from 0.48 to 0.73 with a reduction in absolute Mach number from 0.47 to 0.22 at the radial diffuser discharge.

UITTREKSEL

Evaluering van die werksverigting van ‘n Mikro-gasturbine Sentrifugaalkompressor Diffusor

(“Performance Evaluation of a Micro Gas Turbine Centrifugal Compressor Diffuser”)

D. S. Krige

Departement van Meganiese en Megatroniese Ingenieurswese, Universiteit van Stellenbos, Privaatsak X1, Matieland 7602, Suid-Afrika
Tesis: MSc. Ing. (Meg)

Maart 2013

Mikro-gasturbines wat in die lugvaart industrie gebruik word, vereis ‘n hoë werkverrigting met ‘n kompakte frontale area. Hierdie gasturbines word menigmaal onaantreklik geag weens swak brandstofverbruik en n lae siklus effektiewiteit. Dit het gelei tot ‘n gesamentlike projek om elke komponent van ‘n spesifieke mikro-gasturbine te analiseer en te verbeter. Die fokus van dié ondersoek is die radiale lem diffusor wat deel vorm van ‘n sentrifugaalkompressor. Die deursnee van die diffusor word deur die kompakte gasturbine diameter beperk. Die mikro gasturbine wat ondersoek word is die BMT 120 KS. Die radiale lem diffusor word geanaliseer deur middel van 1-D en 3-D (BVD) berekeninge met behulp van CompAero en FINE^{TM}/Turbo onderskeidelik. Die doelwit is om ‘n diffusor te ontwerp met ‘n verhoogde massavloei en drukverhouding oor die kompressor. ‘n Eksperimentele toetsfasiliteit is ingerig om toetse uit te voer en word gebruik om numeriese berekeninge te bevestig. Die staties-tot-stasiese drukstyging oor die radiale diffusor is verbeter van 1.39 tot 1.44 by ‘n omwentelingspoed van 120 kopm. Die statiese drukherwinningskoeffisiënt is verbeter van 0.48 tot 0.73 met ‘n vermindering in die absolute Machgetal vanaf 0.47 tot 0.22 by die radiale diffusor uitlaat.

ACKNOWLEDGEMENTS

My acknowledgements go to the following individuals and institutions to whom I wish to express my sincere appreciation and gratitude for accompanying me on my MSc journey:

- First and foremost I want to thank my Lord and Savior Jesus Christ for the daily guidance and supernatural provision throughout this thesis. He knows me better than myself and definitely knows how to keep my journey interesting, exciting and challenging. The life lessons learnt in the process of this thesis are irreplaceable and I thank Him for opening my eyes to new frontiers.

- My parents, Skip and Barbara Krige, who selflessly offered up their time and finances to support me in whichever way possible. Their aid through the tough times and praise in the good times as well as their encouragement and faith in me is greatly appreciated.

- Andre Baird, for his patience, assistance and guidance in micro gas turbines. I am truly grateful to him for sharing his experience and life passion with me, as well as the provision of the BMT 120 KS gas turbine.

- My two supervisors, Prof. T. W. von Backström and Dr. S. J. van der Spuy, for their guidance, patience, invaluable advice about turbomachinery and numerous discussions that weren't always related to the topic of this thesis. I always enjoyed the meetings that involved discussions about Africa, Land Rovers, Jetpacks and travelling. I thank you for allowing me free reigns when it came to the scope of this thesis.

- CSIR project (Ballast), ARMSCOR and the South African Airforce, for the funding of this project.

- To all the staff at the Mechanical and Mechatronic Engineering Department, especially Andrew de Wet.

- To the staff in charge of the high performance cluster at Stellenbosch University.

DEDICATIONS

To André Baird…

TABLE OF CONTENTS

LIST OF FIGURES

LIST OF TABLES

NOMENCLATURE

Constants

$R =$	287	$[\mathrm{J/kg \cdot K}]$

Symbols

A	Total blade passage area	$[\mathrm{m^2}]$
A_R	Area ratio	$[-]$
a/c	Point of maximum camber	$[-]$
B	Fractional area blockage	$[-]$
b	Hub-to-shroud passage height	$[\mathrm{m}]$
C	Absolute velocity	$[\mathrm{m/s}]$
C_d	Discharge flow coefficient	$[-]$
C_p	Specific heat at constant pressure	$[\mathrm{J/kg \cdot K}]$
C_r	Contraction ratio	$[-]$
c_p	Static pressure recovery coefficient	$[-]$
c_f	Skin friction coefficient	$[-]$
D	Divergence parameter	$[-]$
D_{eq}	Equivalent diffusion factor	$[-]$
D_m	Diffusion criteria parameter	$[-]$
d	Diameter	$[\mathrm{m}]$
E	Diffuser effectiveness	$[-]$
e	Peak-to-valley surface roughness	$[\mathrm{m}]$
f_c	Correction factor	$[-]$
h	Enthalpy	$[\mathrm{J/kg}]$
h_{th}	Blade-to-blade throat width	$[\mathrm{m}]$
i	Incidence angle $(\beta - \alpha)$	$[^\circ]$
K	Vaned diffuser stall parameter	$[-]$
K_0	Unguided vaned diffuser stall parameter	$[-]$
L	Mean streamline meridional length, dimensionless diffuser blade loading parameter	$[\mathrm{m}]$
L_B	Vane mean streamline camberline length	$[\mathrm{m}]$
Ma	Mach number	$[-]$

m	Meridional length	$[\mathrm{m}]$
$\dot{m}$	Mass flow rate	$[\mathrm{kg/s}]$
N	Rotational speed	$[\mathrm{RPM}]$
PR	Pressure ratio	$[-]$
p	Absolute pressure	$[\mathrm{Pa}]$
$peri$	Perimeter	$[\mathrm{m}]$
p_v	Dynamic pressure $(p_t - p)$	$[\mathrm{Pa}]$
Re	Reynolds number	$[-]$
r	Radius	$[\mathrm{m}]$
s	Specific entropy, clearance gap	$[\mathrm{J/kg \cdot K}]$, $[\mathrm{mm}]$
T	Temperature	$[\mathrm{K}]$
t_b	Blade thickness	$[\mathrm{m}]$
U	Blade speed (ωr)	$[\mathrm{m/s}]$
V	Velocity	$[\mathrm{m/s}]$
W	Relative velocity	$[\mathrm{m/s}]$
w	Vane-to-vane passage width	$[\mathrm{m}]$
X	Choke parameter	$[-]$
y^+	Dimensionless wall distance	$[-]$
y_{wall}	Wall cell height	$[\mathrm{m}]$
z	Number of blades or vanes	$[-]$

Greek symbols

α	Flow angle with respect to tangent	$[^\circ]$
α_C	Mean streamline angle with respect to zenith axis	$[\mathrm{rad}]$
β	Blade angle with respect to tangent	$[^\circ]$
Δ	Difference	$[-]$
δ	Boundary layer thickness	$[\mathrm{m}]$
η	Isentropic efficiency	$[\%]$
θ	Camber angle	$[^\circ]$
μ	Dynamic viscosity coefficient	$[\mathrm{kg/s \cdot m}]$
ρ	Density	$[\mathrm{kg/m^3}]$
σ	Slip factor, point of maximum solidity	$[-]$

ϕ	Flow coefficient	$[-]$
ω	Rotational speed $(2N\pi/60)$	$[\mathrm{rad/s}]$
$\bar{\omega}$	Total pressure loss coefficient	$[-]$
$2\theta_C$	Diffuser divergence angle	$[^\circ]$

Superscripts

$*$	Optimum or sonic flow condition

Subscripts

B	Blade
$bell$	Bell-mouth
BL	Blade loading
CH	Choke
CR	Critical
D	Diffuser
$duct$	Circular inlet duct
FB	Full blades
H	Hydraulic
h	Hub
INA	Standard inlet conditions
i	Index for total pressure loss
$ideal$	Ideal value
inc	Incidence
$inlet$	CFD inlet boundary
I	Impeller
LE	Leading edge
m	Meridional velocity component
max	Maximum value
$outlet$	CFD outlet boundary
PS	Pressure surface
ref	Reference value
S	Stall
SB	Splitter blades

SEP	Separation
SF	Skin friction
SS	Suction surface
s	Shroud
sh	Shock
TT	Total-to-total ratio
t	Total thermodynamic condition
th	Throat
U	Tangential velocity component
VD	Vaned diffuser
0	Impeller eye condition, ambient conditions
1	Impeller inlet condition
2	Impeller tip condition
3	Diffuser inlet condition
4	Diffuser discharge condition

Auxiliary symbols

-	Average of values

Acronyms

B2B	Blade-to-blade
BVD	Berekenings Vloei Dinamika
CAD	Computer Aided Design
CENCOM	Centrifugal Compressor
CFD	Computational Fluid Dynamics
CGNS	Computer format for storage and retrieval of CFD data
CNC	Computer Numerical Control
CV	Control volume
GUI	Graphical user interface
H&I	AutoGrid5^{TM} grid topology
HOH	AutoGrid5^{TM} grid topology
H2S	Hub-to-shroud
IGES	3-D computer model format

IGV	Inlet guide vane
IDISTN	Expert parameter of the EURANUS™ solver
IWRIT	Expert parameter of the EURANUS™ solver
k-ε	Turbulence model
k-ω	Turbulence model
KKK	Kuhnle, Kopp & Kausch
LOCCOR	Expert parameter of the EURANUS™ solver
NGRAF	Expert parameter of the EURANUS™ solver
O4H	AutoGrid5™ grid topology
R-S	Rotor-stator
RMS	Root-mean-square
S-A	Spalart-Allmaras
TORRO	Expert parameter of the EURANUS™ solver
VDDESIGN	Vaned Diffuser Design
1-D	One-dimensional
3-D	Three-dimensional

1 INTRODUCTION

This document involves the study of a Baird Micro Turbine 120 Kero Start (BMT 120 KS) gas turbine, as seen in Figure 1.1, currently used in the model jet industry. A sectional view of the BMT 120 KS is shown in Figure 1.2. During 2009, Krige (2009) under supervision of Prof. T.W. von Backström, investigated the performance of the radial vaned diffuser of the BMT 120 KS turbine as part of an undergraduate project at the University of Stellenbosch.

At the start of 2010 both the Department of Mechanical and Mechatronic Engineering at the University of Stellenbosch and the Council for Scientific and Industrial Research (CSIR) of South Africa decided to launch a joint project called BALLAST, funded by the South African Air Force through ARMSCOR. One of the aims of BALLAST is to further investigate and improve various components and the overall performance of micro gas turbines.

The compressor section of the BMT 120 KS is investigated in this thesis, focusing mainly on the radial diffuser and the flow interaction between the impeller tip and radial diffuser inlet. The compressor section, shown diagrammatically in Figure 1.3, constitutes a centrifugal impeller with a radial diffuser and downstream axial blades. The compressor characteristics are discussed further in Chapter 2.

Small gas turbine engines, making use of centrifugal compressors, are widely used in industry, ranging from small power generation units to helicopter engines or Auxiliary Power Units (APU) in large aircraft.

Centrifugal compressors designed for aeronautical use are required to be as small and light as possible and therefore require radial diffusers to be very compact, but still capable of converting the high velocity exiting the impeller into static pressure. The frontal area of the turbine is proportional to its drag during flight and therefore need to be constrained. One major challenge in the design of high performance centrifugal compressors is the design of a diffuser capable of large pressure recovery over a short radial distance for a relatively wide operating range. Micro gas turbines require compressors that can operate at maximum efficiency with adequate pressure recovery for proper fuel combustion.

It is not uncommon to see centrifugal impeller designs delivering total-to-total efficiencies up to 90% (Tamaki et al., 2009). However efficiencies recorded over the entire compressor i.e. impeller and diffuser combined, are considerably lower. This is due to poor diffuser performance resulting from frictional and diffusion losses or improper matching of fluid flow through the compressor components. According to Au (1991) "*both the efficiency and surge-to-choke operating range of a centrifugal compressor depend strongly on the performance of the diffuser*". The diffuser is the main component limiting the stable operating range of the centrifugal compressor.

It is therefore the aim of this thesis to firstly evaluate the BMT 120 KS compressor performance experimentally and compare it to one- and three-

dimensional (1-D and 3-D) numerical analyses of the same compressor and secondly to improve the radial diffuser of this compressor based on a numerical approach.

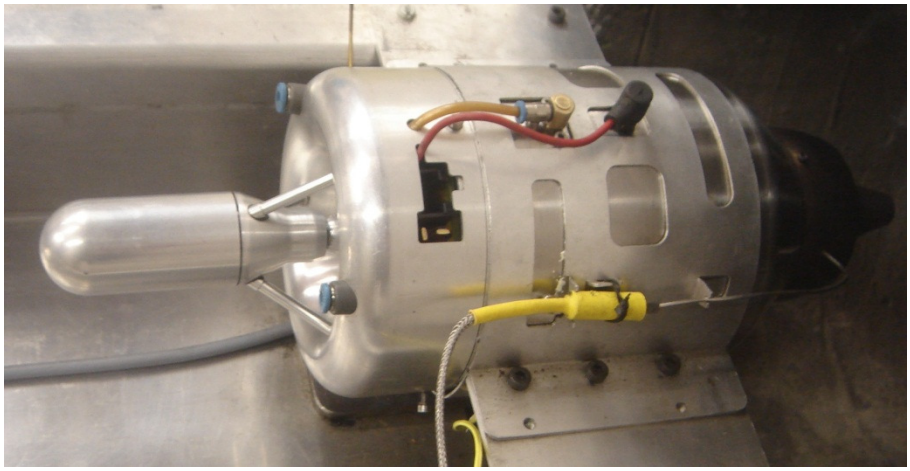

Figure 1.1: BMT 120 KS micro gas turbine

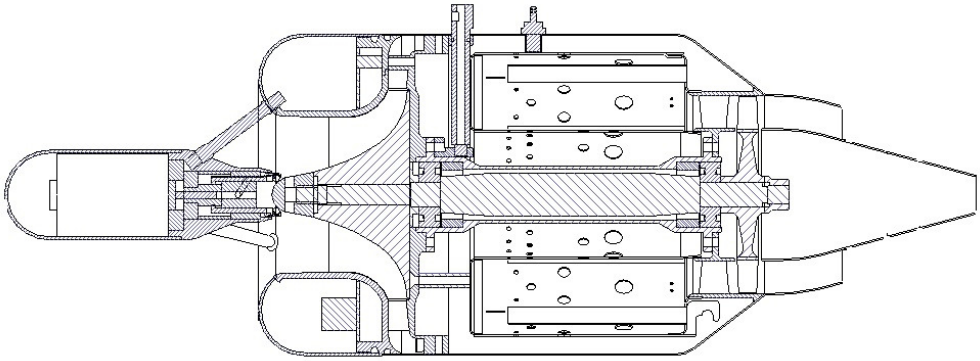

Figure 1.2: Section view of a BMT 120 KS Micro Gas Turbine

The 1-D analysis follows a mean streamline through the compressor, as seen in Figure 2.2, incorporating fundamental compressor theory and empirical loss models, as presented by Aungier (2000). The 1-D analysis for the impeller, vaneless annular passage and vaned diffuser components are performed with Aungier's (2009) 1-D CompAero software package and is discussed further in Section 3.2 and Appendix A.

The Computational Fluid Dynamics (CFD) software package, FINE™/Turbo by NUMECA™ International, is used for the 3-D CFD analysis. The CFD environment is discussed in Chapter 3 and Appendix A.

1.1 Background and Motivation

Prior to World War II, a lot of effort went into the investigation and development of gas turbines. Initially they were designed to produce shaft power, but attention quickly progressed to the development of a turbojet engine for aircraft propulsion. The use of micro gas turbines have rapidly progressed to that of the Unmanned

Aerial Vehicle (UAV) and model jet industries. A well designed gas turbine will outperform the usual ducted fan, pulse jet or two stroke reciprocating piston engines due to its ability to operate at higher temperatures resulting in higher overall efficiencies, especially at high flying speeds.

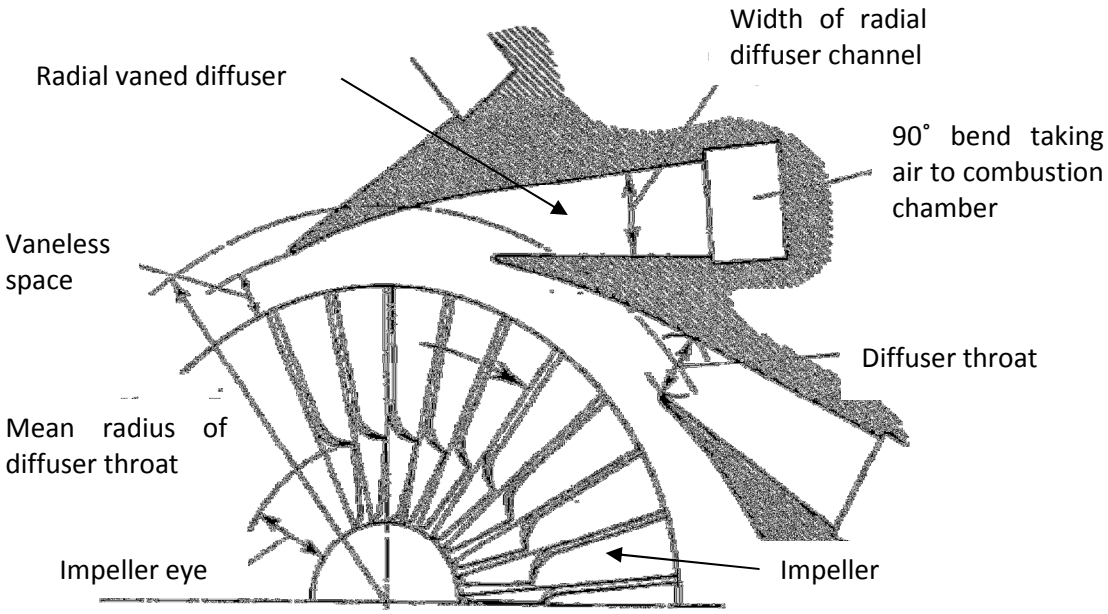

Figure 1.3: Diagrammatic sketch of a centrifugal compressor indicating the impeller and diffuser (Saravanamuttoo, 2001)

A comparison of overall thrust to weight ratio shows that the gas turbine outperforms its competitors (Smith, 1997).

Two separate micro gas turbines, similar in size to that of the BMT 120 KS, are used to illustrate the performance capabilities of micro gas turbines. The two micro gas turbines under consideration are the Hamilton Sundstrand TJ-50 (Harris et al., 2003) and the Gerald Rutten (2008) GR 180 gas turbines. Hamilton Sundstrand developed a micro gas turbine, TJ-50 shown in Figure 1.4, with a mixed flow compressor. Its performance is shown in Table 1.1. According to Harris et al. (2003) the key to the TJ – 50's success is assigned to its "*efficient mixed flow turbomachinery, a high rotating speed capability (130000 RPM) and a short residence time combustor. The turbomachinery maximizes the thrust for a given diameter and the combustor is capable of starting and stable operation at high loadings*".

The GR 180 turbine is in essence very similar to the geometry and components of the BMT 120 KS. The length of the GR 180 micro gas turbine is slightly longer than the BMT 120 KS and it makes use of a commercial off the shelf Schwitzer S200 impeller with a tip diameter of 74 mm (Figure 1.6 a) whereas the BMT 120 KS micro gas turbine uses a 70 mm diameter KKK K27.2 impeller (Figure 1.6 b). Table 1.2 displays the performance and geometry comparisons between the GR 180 and the BMT 120 KS.

Figure 1.4: TJ-50 turbine components (Hamilton Sundstrand, 2003)

Table 1.1: TJ – 50 Performance (sea level static), (Hamilton Sundstrand, 2003)

TJ – 50	Objective	Demonstrated
Thrust [N]	231	254
Air Flow [kg/s]	0.363	0.381
Pressure Ratio	4.4	5.2
Turbine Inlet Temperature [˚C]	1132	1093
Engine diameter [mm]	-	111.7
Engine length [mm]	-	304.8

Table 1.2: Comparisons between the GR 180 and BMT 120 KS

	GR 180	BMT 120 KS
Rotational speed [krpm]	120	120
Thrust [N]	186.0	107.3
Pressure Ratio	3.40	2.62
Exhaust Gas Temperature [˚C]	810	703
Engine diameter [mm]	107.5	107.8
Engine length [mm]	210	194
Impeller diameter [mm]	74	70
Turbine wheel [mm]	70	70

Figure 1.5 a) and b) both compare the total-to-static pressure ratio and engine thrust between the BMT 120 KS and the GR 180 turbines respectively. When comparing performance results of the BMT 120 KS to the mixed flow TJ-50 and the GR 180 gas turbines, it is clear that improvements to the current BMT 120 KS turbine components are possible and necessary. It should also be mentioned that the larger Schwitzer S200 impeller used in the GR 180 turbine contributes to its superior performance.

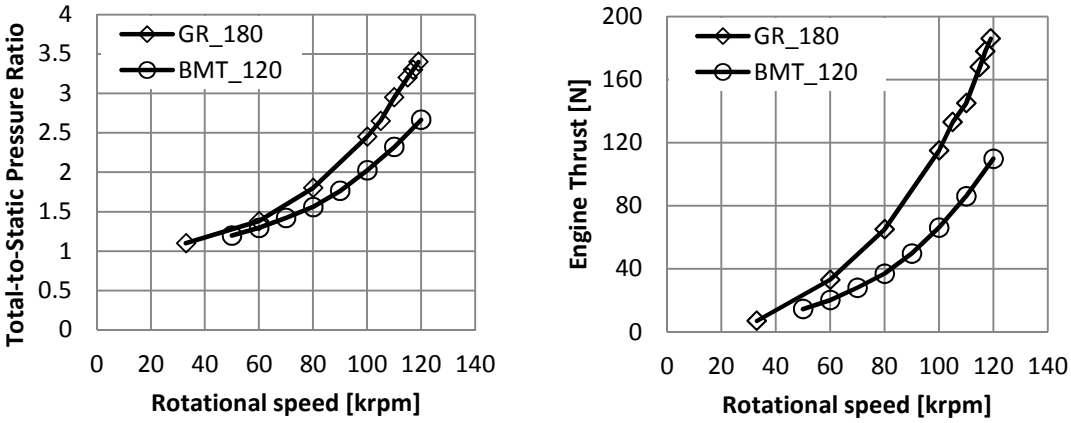

Figure 1.5: Performance comparisons between the GR 180 and the BMT 120 for a) Total-Static pressure ratio and b) Engine thrust

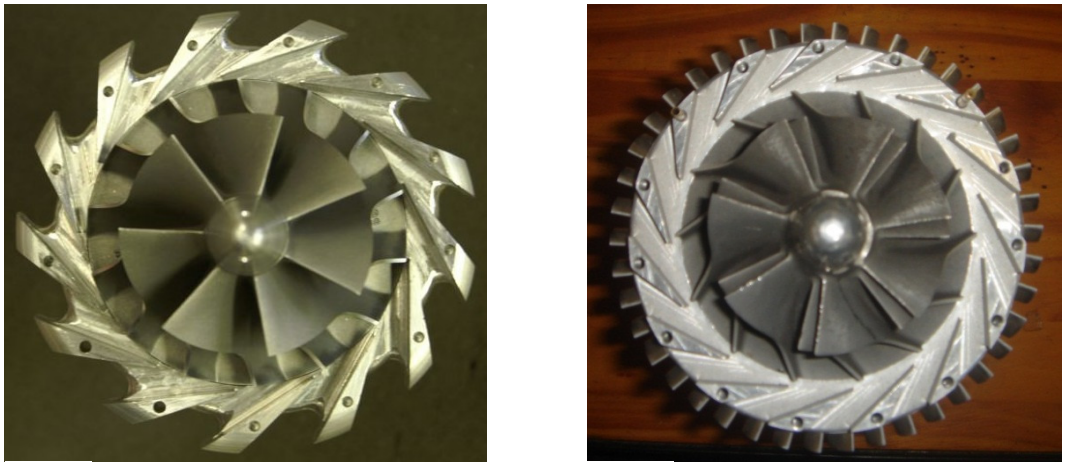

Figure 1.6: a) GR 180 compressor section, b) BMT 120 KS compressor section

1.2 Objectives and Methodology

The objective of this thesis is to investigate, evaluate and redesign the radial vaned diffuser of the BMT 120 KS micro gas turbine to obtain a more efficient diffuser capable of improved pressure recovery at a higher mass flow rate.
A brief point-wise discussion of the methodology used to achieve the thesis objectives are listed in chronological order below:

- Construction of a test bench for the BMT 120 KS micro gas turbine with appropriate equipment.
- Calibration of all test bench measureming equipment.
- Record several runs with the BMT 120 KS micro gas turbine to determine the accuracy, reliability and repeatability of the test bench between consecutive runs and compare the data to the data recorded by Krige (2009).
- Model all relevant compressor components in a Computer Aided Design (CAD) package. SolidWorks is the CAD package used for all components.
- Export all relevant compressor geometries into the 1-D software package to analyze the mean streamline data. CompAero based on centrifugal compressor theory by Aungier (2000), is the 1-D software package used.
- Export all relevant compressor geometries into the 3-D Computational Fluid Dynamic (CFD) software package to model and analyze the full compressor. FINE^{TM}Turbo by NUMECA^{TM} International is the CFD software package used.
- Verification and validation of numerical results.
- Perform preliminary radial diffuser designs using both 1-D and 3-D software systems.
- Finalization of radial diffuser designs.
- Computer Numerical Control (CNC) machining of the new radial diffuser designs.
- Experimental testing of the BMT 120 KS micro gas turbine with the new radial diffusers.
- Evaluate and compare the experimental results.
- Draw conclusions from the investigations and provide recommendations for future work.

2 LITERATURE STUDY

The literature study entails a detailed discussion of the relevant geometry and safe operating conditions of a centrifugal compressor in a micro gas turbine. The 1-D analysis procedures of Aungier (2000) and the 3-D CFD modelling procedures using FINE^{TM}/Turbo, are discussed in Chapter 3 and Appendix A.

2.1 Basic Operating Principles of a Centrifugal Compressor

A single shaft gas turbine with a centrifugal compressor relevant to this thesis, as shown in Figure 2.1, is considered in the following discussion. The compressor section investigated in this thesis is divided into different components as shown in Figure 2.2.

Figure 2.1: Single shaft BMT 120 KS compressor section

A centrifugal compressor typically consists of two major components, namely a rotating impeller and a stationary diffuser. Air enters the impeller inlet in a relatively uniform axial direction and is turned at high rotational speeds into the radial direction by main- and splitter- blades on the impeller disc. No Inlet Guide Vanes (IGV) are used in this gas turbine configuration. The impeller imparts energy to the operating gas by means of blade forces and pressure distributions that exist in the blade passages as air is forced from the axial- into the radial-direction, causing an increase in angular momentum and a rise in total enthalpy. A vaneless annular passage exists between the impeller tip and radial diffuser inlet. The vaneless annular passage increases the flow area and radius at which the flow rotates, resulting in a decrease in Mach number, if the Mach number is less than 1, and a rise in static pressure. The optimal radial distance of the vaneless annular passage may vary, depending on the magnitude of the Mach number exiting the impeller. Further diffusion is enabled by radial diffuser vanes, whereby the flow area is gradually increased to facilitate additional static

pressure recovery. Using a vaned diffuser in the compressor assembly slightly reduces the compressor operating range (Aungier, 2000), but has the added benefit of further static pressure recovery over a smaller required diffuser length, (Dixon, 2005). According to Dixon (2005), not only does the required diffuser length decrease when implementing diffuser vanes, but diffusion also occurs at a much higher rate with improved efficiency.

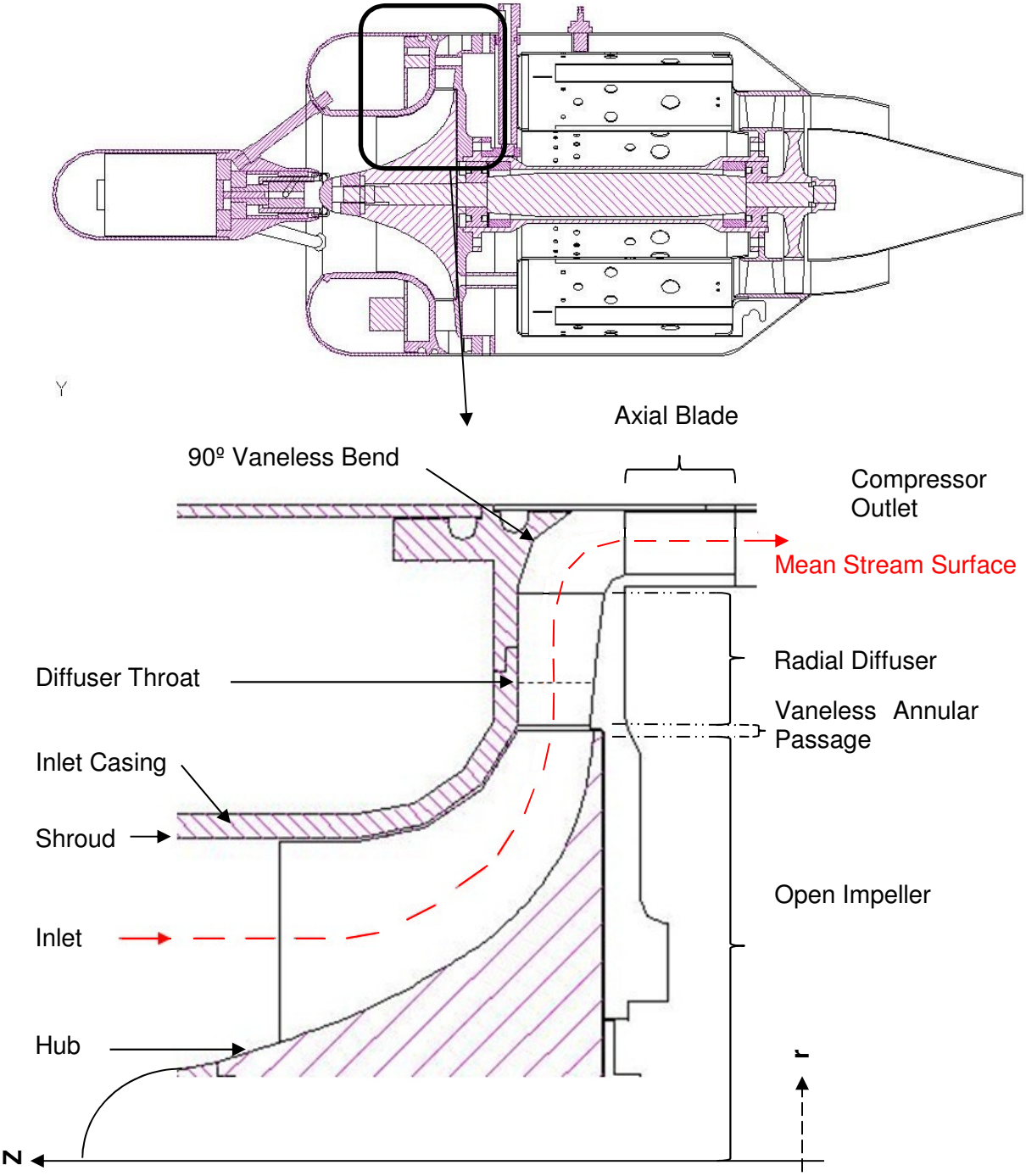

Figure 2.2: Centrifugal compressor overview in the r-Z plane

As the fluid leaves the radial diffuser vanes it is presented to another vaneless space with a 90˚ bend that redirects the radial flow into the axial direction. The reason for using a vaneless space behind the radial diffuser is attributed to the limited radial space in a micro gas turbine and helps to further reduce high Mach numbers, due to the increased flow area. During experiments by Krige (2009) it was noted that the 90˚ vaneless bend creates an unfavorable swirl component in the flow that may result in poor combustion in the downstream combustion chamber. This phenomenon is countered by adding a row of axial blades in the flow passage to redirect the flow into the axial direction.

The flame stability and propagation in the combustion chamber, downstream of the axial blades, is largely affected by the velocity of the air presented to the fuel injector nozzles. Therefore air at a lower velocity, presented in a more stable fashion, improves combustion and ultimately engine performance.

2.1.1 Centrifugal Compressor Theory

The flow through the centrifugal compressor is highly three-dimensional and complicated, making a full 3-D analysis essential. However, the flow model can be simplified to obtain approximate solutions by following a *one-dimensional* approach, by assuming that fluid conditions are uniform over the compressor components. The operating fluid in a micro gas turbine is air and is modelled using compressible flow theory. Since the air density is subject to temperature and pressure changes, it is convenient to examine the centrifugal compressor performance by means of a Mollier chart making use of thermodynamic properties. The Mollier chart in Figure 2.3 shows the compressor performance from impeller inlet (*1*) to diffuser exit (*4*). The diffuser performance and theoretical analysis will be further discussed in Sections 2.3 and 2.4, for the vaneless annular section and the radial diffuser sections respectively.

Compressor calculations and equations are shown where necessary and are discussed further in Appendix C.

2.1.2 Compressor Instabilities

Engine failure or poor operation may result from a number of compressor instabilities. The three main limitations associated with centrifugal compressor operation will briefly be discussed in the following section.

The first condition is known as compressor or rotating stall. Compressor stall occurs when the airflow through the compressor becomes unstable. This is due to an imbalance between vector quantities, namely: compressor rotational speed and inlet velocity, and a pressure ratio that is incompatible with the engine speed. This occurs when the effective angle of attack of one or more compressor blades exceeds the critical angle of attack. Compressor stall causes the air flow to decrease and stagnate in the compressor. It can even reverse the direction of air flow, leading to engine failure. Compressor or rotating stall may lead to compressor surge, but can exist on its own during stable operation (Sayers, 1990).

The second condition is known as compressor choke. Compressor choke occurs when no additional flow can pass through the compressor, i.e. when the pressure ratio of a constant speed line drops rapidly with a very small change in mass flow, indicated by the vertical constant speed lines in Figure 2.4. This occurs when the flow reaches sonic speeds, Mach ≥1, in either the impeller or diffuser throat, Dixon (1979).

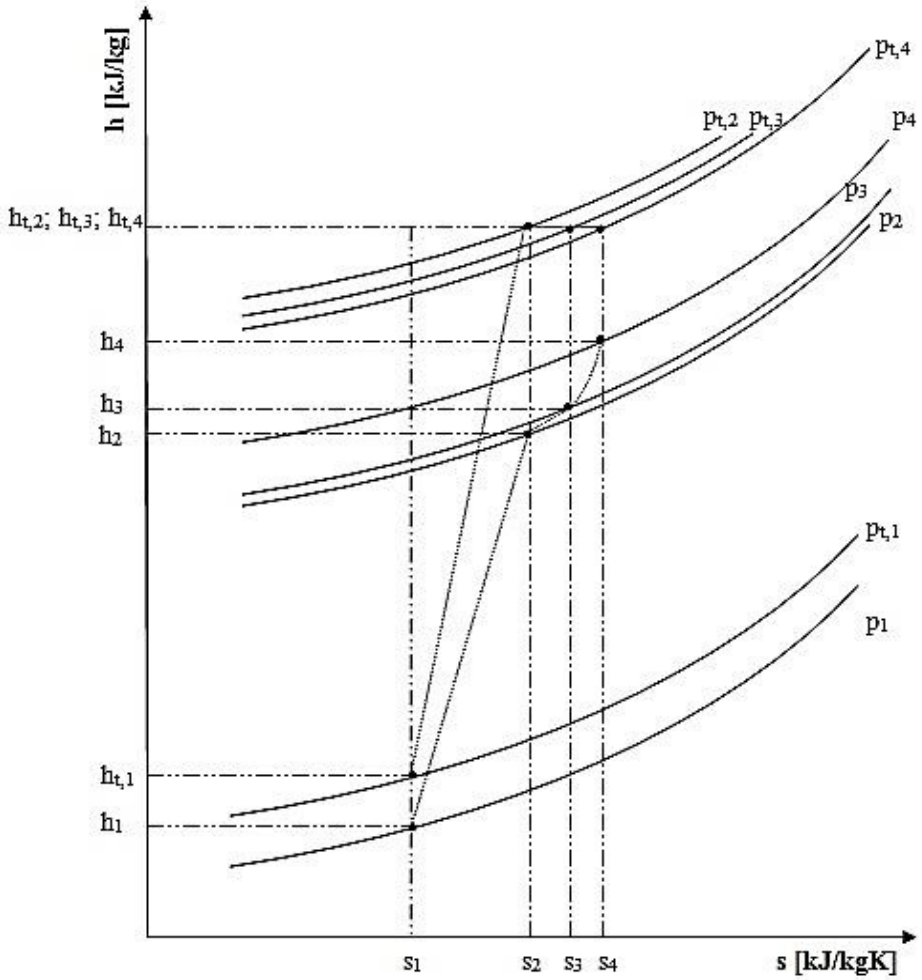

Figure 2.3: Mollier diagram for the complete centrifugal compressor stage

When flow through a compressor can no longer be maintained, surge occurs. Surge is in effect similar to compressor stall, a phenomenon that occurs at low mass flow conditions, as seen in Figure 2.4. It is caused by an increase in pressure, causing the compressor to fall below the minimum flow limit required at a specificied speed for stable operation and can cause gas flow to briefly reverse direction. According to van Helvoirt (2007), "*surge is an unstable operating mode of a compression system that occurs at mass flows below the so-called surge line*".

Baghdadi et al. (1975) performed visual studies and performance measurements on three sets of vanes representing common vaned diffuser designs. From their

studies it was observed that flow separation in the vaneless or semi-vaneless space between the impeller exit and diffuser throat caused instability, resulting in compressor surge. They claimed that the only factor having an effect on the surge-to-choke operating range is the number of diffuser vanes.

According to Moroz (2010) the surge margin is greatly reduced when using a vaned diffuser, as a result of changes in suction pressures**.** This is due to the large incidence angle that exists at the impeller exit with respect to the diffuser blade angle.

The above mentioned compressor instabilities may occur when the engine operates at conditions other than its design point. These conditions should be avoided during operation, since it affects the performance of the compressor, resulting in a significant loss in performance and efficiency and will have detrimental effects on the compressor components that may lead to engine failure. The range of mass flow between surge and choke diminishes for compressors that are designed for a higher pressure ratio. An example of a centrifugal compressor's characteristic curves is indicated in Figure 2.4.

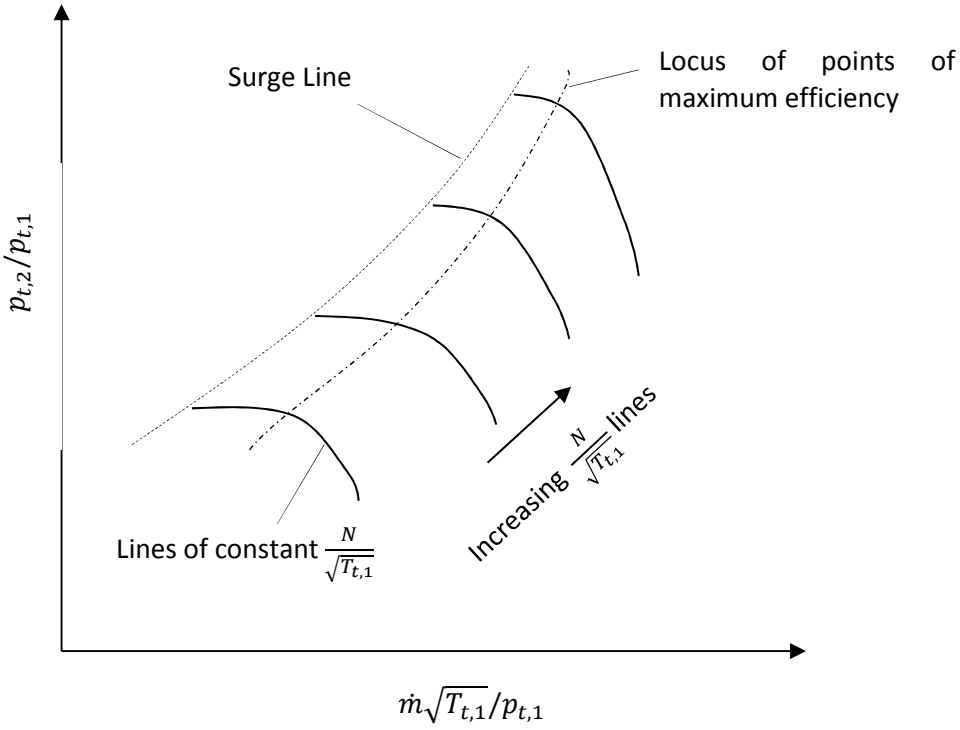

Figure 2.4: Overall characteristic of a centrifugal compressor

2.2 Impeller Performance

A vast amount of research have been performed and theory developed for centrifugal impellers resulting in various impeller designs capable of achieving

efficiencies up to 90% (Tamaki et al., 2009). In this thesis the impeller will however not be redesigned. The subject is restricted to the characteristics of the air and flow angles at the impeller inlet and impeller tip. The impeller used in the BMT 120 KS turbine is a KKK K27.2 turbocharger compressor wheel, and is discussed further in Section 3.3.3. All theoretical 1-D and 3-D analyses done on the compressor are based on this specific impeller.

2.3 Vaneless Annular Passage Performance

The centrifugal compressor under investigation makes use of two separate vaneless annular passages (vaneless spaces). The first passage exists between the impeller tip and radial diffuser inlet and the second, a 90˚ vaneless bend, exists between the radial diffuser exit and the axial blade inlet. The first passage is shown schematically in Figure 2.5.

Flow entering the vaneless diffuser annular passage may be supersonic at high rotational speeds, resulting in absolute Mach numbers well in excess of 1. This may cause shockwaves to occur at the diffuser inlet or throat. In an attempt to reduce the high fluid velocity exiting from the impeller blades, and achieve effective pressure recovery in the diffuser, a relatively large vaneless space between the impeller tip and diffuser inlet is required.

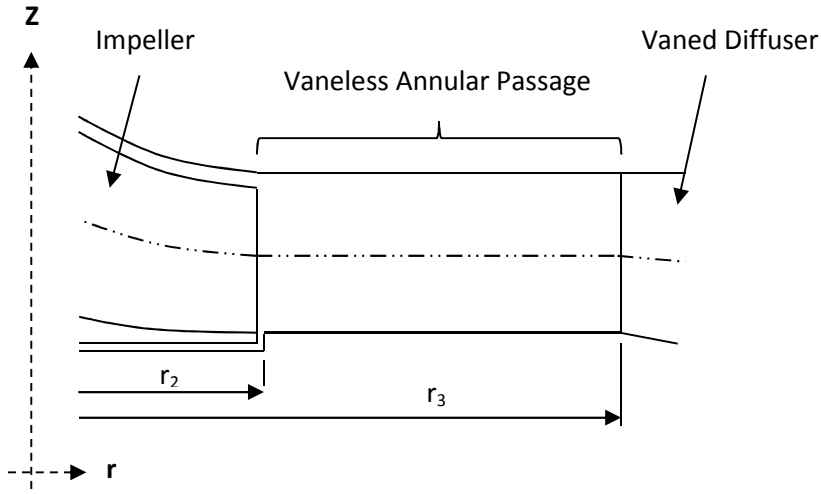

Figure 2.5: Vaneless annular passage (vaneless space)

Sayers (1990) states that if the radial flow velocity component is subsonic, then no loss in efficiency is caused by the formation of shock waves, and this is ultimately the purpose of the vaneless annular passage.

The three main functions of the vaneless space between the impeller exit and diffuser inlet can be summarized as follows (Dixon, 1979):

- To reduce the circumferential pressure gradient at the impeller tip.

- To smooth out velocity variations between the impeller tip and diffuser vanes.
- To reduce the high Mach numbers exiting the impeller.

The flow in the region between the impeller tip and diffuser inlet is considered to be turbulent, three dimensional and rather complex. Dixon (1979) regards the flow exiting the impeller tip to follow a logarithmic spiral path up to the diffuser vanes.

Diffusion in the vaneless annular passage is governed by 1.) the conservation of angular momentum, i.e. the swirl velocity is reduced due to an increase in radius, and 2.) the increase in flow area due to an increase in radial length, i.e. controlling the radial velocity component by adjusting the radial flow area (Sayers, 1990).

Adiabatic flow through the vaneless passage is summarized by means of a Mollier chart, Figure 2.6, with impeller tip (*2*) and vaned diffuser inlet (*3*) as reference. The total pressure drops as a result of frictional forces in the passage, causing an increase in entropy.

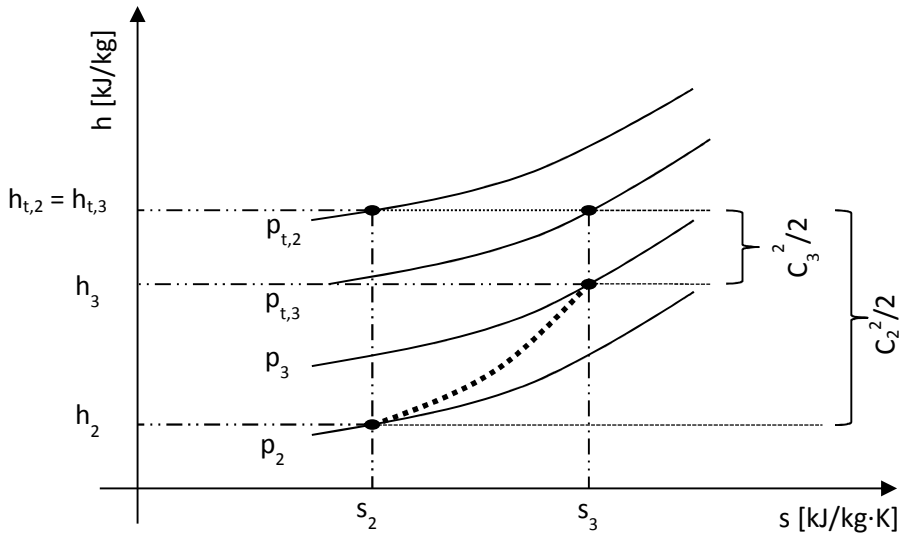

Figure 2.6: Vaneless annular passage Mollier chart

The length of the vaneless annular passage influences the pressure ratio, mass flow rate, efficiency, noise and mechanical loading of the compressor (Ziegler et al., 2003). At higher mass flows a longer vaneless space is required to reduce the high fluid velocity exiting the impeller and losses in the vaneless diffuser before entering the vaned diffuser (Benini et al., 2006).

Rayan et al. (1980) investigated the effect of high swirl on vaned diffusers. Their investigation showed that the length of the vaneless space between the impeller exit and diffuser leading edge is a major factor in diffuser efficiency. Concluding from their experiments, they achieved a minimum loss coefficient when the vane leading edge radius is approximately 1.2 times the vaneless diffuser inlet radius, i.e. $r_3 = 1.2r_2$. On the other hand, Aungier (2000) recommends a vaneless radius

ratio, r_3/r_2, of between 1.06 and 1.12, i.e.1.06 ≤ r_3/r_2 ≤ 1.12. The lower limit of 1.06 is used to provide space for the distorted impeller flow to smooth out and the blade wakes to decay before the flow enters the diffuser vanes. The upper limit of 1.12 is used due to the low-flow angles involved that occurs as a result of the high impeller tip Mach numbers, resulting in high vaneless space loss levels (Aungier, 2000). Also, too much diffusion in the vaneless or semi vaneless space will result in excessive boundary layer growth that leads to large throat blockage in the vaned diffuser (Bennet et al, 2000).

From investigations composed by Ziegler et al (2003), the radial extent of the vaneless annular passage between the impeller exit and diffuser inlet was varied between 4 to 18% of the impeller tip radius, i.e. 1.04 ≤ r_3/r_2 ≤ 1.18. They found an increase in total pressure with a decrease in the vaneless annular passage length. They also found that the air flow exiting the diffuser vanes is more homogeneous at smaller vaneless spaces, indicating better diffusion.

Shum (2000) conducted a study on the effect of impeller-diffuser interaction on the performance of a centrifugal compressor. His principal finding was that the most influential factor of unsteady flow and compressor performance is the impeller tip leakage flow. He examined various impeller-diffuser spacings and found that there exists an optimum radial gap size for maximum impeller pressure rise. He did tests on radius ratios, r_3/r_2, of 1.092 and 1.054. His results indicated better performance for the 1.092 ratio. He concluded by saying that the "*beneficial effects of impeller-diffuser interaction on overall stage performance come mainly from the reduced blockage and reduced slip associated with the unsteady tip leakage flow in the impeller*".

Saravanamuttoo et al. (2001) stated that the dangers of encountering shock losses and excessive circumferential variation in static pressure are considerably increased if the diffuser leading edges are too close to the impeller tip. A number of investigations and studies have been performed on gas turbine centrifugal compressors, focusing mainly on the flow interaction between the impeller exit and vaned diffuser inlet. At present three-dimensional flow in this region is not yet fully understood.

The size of the vaneless annular passage is determined by Equations C.1.1 to C.1.4 with reference to Figure 2.5. To obtain a large reduction in kinetic energy the absolute velocity component needs to be as small as possible, requiring the radial length to be large, and therefore results in a vaneless space with a large radius (r_3), (Sayers, 1990).

2.4 Diffuser Performance

The main function of a diffuser is to recover and convert the maximum possible amount of kinetic energy, generated by the impeller, to static pressure. Due to the geometry constraints on gas turbines used in the aeronautical industry, centrifugal compressors require very compact diffusers. For example the radial length as well as the diagonal or axial length of the diffuser is limited to that of the engine housing or combustion chamber, resulting in reduced diffusion and

pressure recovery in the diffuser section. This increases the importance of proper diffuser design and appropriate blade angle selection to match the fluid flow angles from hub to shroud and from leading to trailing edge of the radial vanes.

Two major features that concern the design of an effective vaned diffuser is firstly and most importantly the radial vanes of the diffuser and secondly the 90˚ annular bend as gas flows from the radial into the axial direction in a diameter constrained design. The radial vanes are considered the most critical feature of the diffuser, more specifically the leading edge, due to its interaction with the exit flow of the impeller and the strong diffusion that needs to occur in these relatively short passages. Figures 2.7 and 2.8 are used as reference to describe the operation of a radial vaned diffuser further.

2.4.1 Vaned Diffuser Theory

The flow process in a vaned diffuser is similar in concept to that of the vaneless annular passage. No energy addition occurs in the diffuser passages and the process is again assumed to be adiabatic, resulting in the total enthalpy remaining constant throughout the vaned diffuser. The Mollier chart in Figure 2.9 summarizes the process through the radial vaned diffuser with diffuser inlet (*3*), diffuser throat (*th*) and diffuser outlet (*4*) as reference stations. The process whereby the fluid is moved from a region of high concentration or total pressure and low static pressure to a region of a lower concentration with an increased static pressure is known as diffusion. Diffusion for subsonic flows is achieved by a flow area increase from the diffuser inlet to the diffuser outlet. The stagnation pressure at the diffuser outlet ($P_{t,4}$) needs to have as small a kinetic term as possible, as this simplifies the combustion chamber design (Sayers, 1990).

The increase in area reduces the high velocity of the flow and thus converts the kinetic energy to static pressure. This can be shown from the principle of mass flow conservation as follows:

$$\dot{m}_{in} = \dot{m}_{out} = \rho_1 A_1 C_1 = \rho_2 A_2 C_2$$

where ρ is the fluid density, A is the flow area and C the absolute velocity.

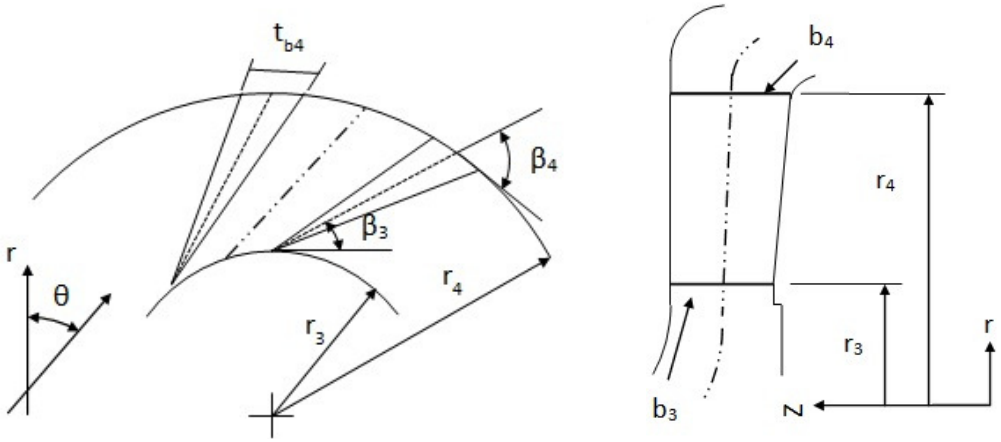

Figure 2.7: Vaned diffuser geometry in the *r-θ* and *r-Z* planes

Therefore as the flow area gradually increases, the absolute velocity decreases, assuming the density doesn't vary too much, resulting in a decrease in kinetic energy.

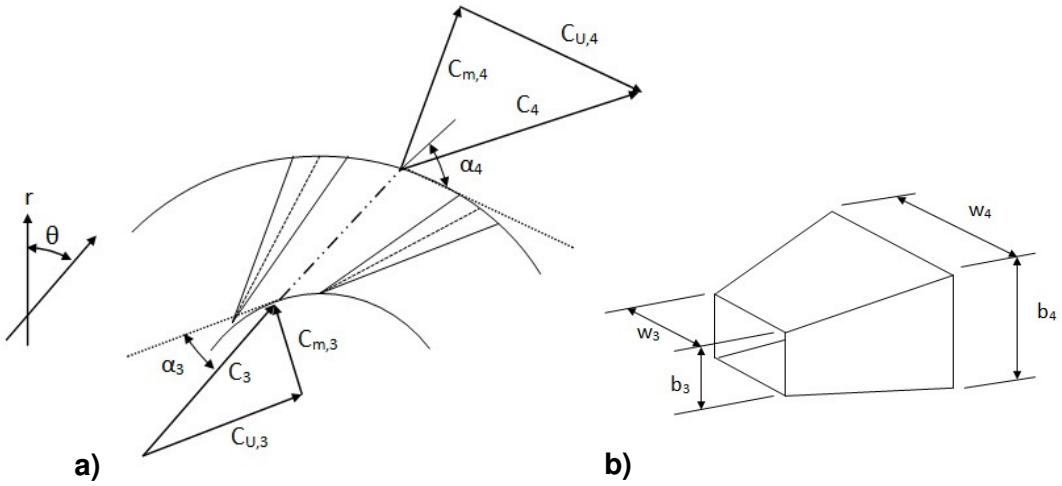

Figure 2.8: a) Vaned diffuser velocity triangles and b) sketch of a channel diffuser

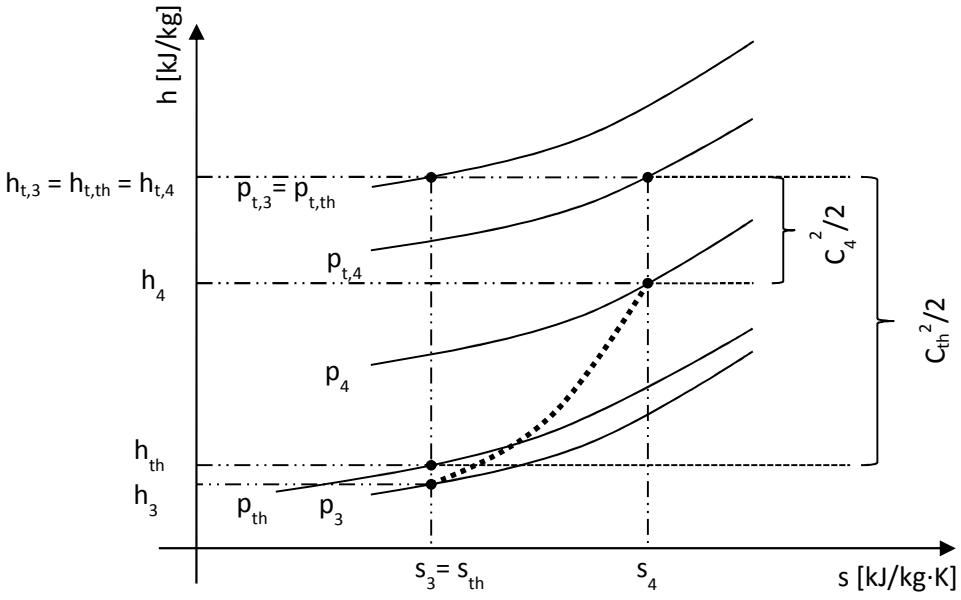

Figure 2.9: Vaned diffuser Mollier chart

The total-to-total compressor efficiency and pressure ratio are defined by equations B.7 and B.8.

To design a highly effective diffuser many geometric and aerodynamic parameters need to be investigated. These parameters will be discussed in the following consecutive sections.

2.4.2 Diffuser Geometric Parameters

This section involves the geometric parameters that need to be considered when designing a vaned diffuser. Modifications made by various authors to the conventional vane-island diffusers, in an attempt to improve the overall compressor performance, are also included where necessary.

a) Vaned versus Vaneless Diffusers

In a vaned diffuser the radial vanes are used to remove swirl at a much higher rate than a vaneless diffuser with a large radius. A vaned diffuser minimizes both flow instability and the possibility of reverse flow. The vanes also reduce the length of the flow path required, making it advantageous for use in radially constrained applications. However a diffuser with a high solidity, i.e. too many vanes, may be prone to premature choking. Kenney (1970) investigated the difference in performance between vaned and vaneless diffusers at high Mach numbers and found that the kinetic energy generated at the impeller tip is too large for efficient pressure recovery in vaneless diffusers. Au (1991) recommends vaned diffusers for medium to high pressure ratio applications. He states that sufficient pressure recovery is obtained by making use of vaned diffusers that gradually increase the flow area.

Inoue and Cumpsty (1984) investigated centrifugal impeller discharge flow in vaned and vaneless diffusers. They observed that "*circumferential distortion from the impeller attenuated very rapidly and had only minor effects on the flow inside the vaned diffuser passage*". In addition they found that when the diffuser vanes were too close to the impeller, flow reversal back into the impeller occurred at low mass flows. Shum (2000) confirmed this when he placed the diffuser closer to the impeller than the optimum and noted that increased losses overcame the benefits of reduced slip (σ) and blockage (B).

Xi et al. (2007) observed an increase in pressure and efficiency by making use of vaned diffusers. Vaned diffusers directly affect the optimum working conditions and operating range of the compressor. Work done by Osborne (1979) indicates the performance characteristic differences between vaned and vaneless diffusers in centrifugal compressors. He states that the main difference between vaned and vaneless diffusers is the larger operating flow range produced by vaneless diffusers at the expense of rapid pressure recovery. From his results it can be seen that the vaned diffuser produced a much higher peak stage efficiency.

It is therefore clear that a compact diffuser design definitely requires vanes for rapid pressure recovery.

b) Passage Divergence and Radial Length

Gas turbines used for aeronautical applications have size and weight restrictions, resulting in a restricted engine diameter, as is the case for this thesis. This confines the radial length of the diffuser, making adequate diffusion challenging. Accordingly the compact diffuser's radial length and geometry plays a critical part in the compressor efficiency.

In the case of simple channel diffusers, the specification of area ratio (A_R) and streamwise length (L_B) automatically determine the divergence angle (θ). Ashjaee and Johnston (1979) showed by means of a pressure recovery versus non-dimensional diffuser length plot ($c_p\ vs\ L/w$) the importance of these parameters (A_R, L_B, θ). From their data a divergence angle of approximately 9˚, i.e. $2\theta = 9^{\circ}$, produced a peak pressure recovery. At values other than this, inefficient or insufficient diffusion occurs. According to Sayers (1990) the divergence angle of the diffuser passage is the controlling variable for the rate of diffusion. He agrees that an appropriate divergence angle of between 8˚ to 10˚ should ensure no boundary layer separation along the passage walls. The rate of divergence of the first portion of a diffuser is extremely important and determines approximately two-thirds of the pressure recovery in the first 30% of the diffuser length from the leading edge (Japikse and Baines, 1998).

Runstadler and Dolan (1973) suggest a non-dimensional length (*L/w)* of 17 for optimum pressure recovery. This will however be impossible to achieve in constrained compressor geometries.

c) Throat Aspect Ratio

The throat aspect ratio is the ratio of the diffuser throat depth to width ratio (b_{th}/w_{th}). For an aspect ratio of 1 or greater very little variation in performance is observed. However for low aspect ratios, i.e. aspect ratios below 0.5, a significant loss in diffuser pressure recovery is observed (Japikse and Baines, 1998). There is agreement from various investigations by different authors that small aspect ratios penalize the pressure recovery substantially. Nonetheless the variations in pressure recovery for large aspect ratios should be carefully considered. Japikse and Baines states that the "*aspect ratio is strongly coupled with aerodynamic blockage, Mach number and Reynolds number effects*".

d) Passage Shape and Geometry

Diffusers that have been used in high pressure ratio applications range from vane-island diffuser passages, diffuser wedge type airfoils to piped diffusers. In more general terms these can be referred to as channel diffusers, annular diffusers and conical diffusers.

Various radial flow diffuser geometries exist for the diffuser leading- to trailing-edge and have been investigated by many turbomachine researchers. Discussed below are only a few diffuser designs that pose useful information and findings with regards to the diffusers considered in this thesis.

Au (1991) investigated four different diffuser designs namely:

1. Straight vane leading edge with parallel end walls (i.e. with axisymmetric end walls).
2. Straight vane leading edge with non-axisymmetric end walls.
3. Parabolic vane leading edge with parallel end walls (i.e. with axisymmetric end walls).
4. Parabolic vane leading edge with non-axisymmetric end walls.

From these investigations Au (1991) stated that there is not much difference between the parallel end wall and non-axisymmetric end wall diffusers. However the stagnation pressure loss is less for diffusers with a parabolic leading edge than the straight leading edge. He found that by increasing the passage depth to chord ratio (*b/c*), the end wall configuration of the passages become more prominent. According to Au (1991) the two parameters in diffuser design that are of particular importance are the pitch-to-chord ratio (h_{th}/c) and the passage depth-to-chord ratio (*b/c*). He found that if these two ratios are small, the flow will not respond to changes in end wall contouring and the flow can be treated as being one-dimensional. However when the ratios are sufficiently large an increase of 5% in the pressure recovery coefficient (c_{PD}) is experienced in diffusers that lack axial symmetry.

Bennet et al. (2000) replaced the straight-walled channel diffusers with pipe or conical type diffuser passages. The reasons for using these diffuser passages are given by him as follows:

- Theoretical considerations show that they have a better flow-to-wetted area relationship than vane island diffusers, resulting in reduced frictional losses.
- In a pipe diffuser it is often possible to obtain an improved diffusion area ratio within the same geometrical constraints.
- The leading-edge geometry, resulting from the intersection of two D-shaped or conical shaped pipes or passages, is also claimed to be capable of handling highly distorted flows leaving the impeller, without large losses.
- The performance of the pipe diffuser is claimed to be particularly superior and plays an important role at high inlet Mach numbers and is thus likely to be of increasing importance in higher-pressure-ratio stages.

Pipe diffusers, as used by both General Electric and Pratt and Whitney in North America, have been claimed to be an improvement over conventional vane island diffusers (Bennett et al, 2000). Based on this claim, up to 2 - 3 percent improvement in compressor efficiency is thought possible with the use of pipe diffusers, in particular at higher pressure ratios.

Roberts et al. (2003) found that one of the main causes that negatively affect the compressor efficiency and increases pressure losses in the compressor is any mismatch between the impeller exit flow angle and the diffuser inlet vane angle. Since the air exiting the impeller is not uniform from hub to shroud, it follows that the diffuser leading edge profile needs to be aligned such that it matches the 3-Dimensional air flow and help reduce boundary layer growth. The diffuser inlet shape is a geometrical parameter that some authors recommend replacing by a sharp leading edge, whereas others prefer a rounded or curved leading edge. Runstadler and Dolan (1973) found little difference in the measured performance between sharp and rounded leading edges for Mach numbers below 1.2. Kenny (1970) observed a higher performance for conical diffusers over channel diffusers and attributed the difference to the inlet region which took the shape of a "*swallow tail*" or scallop as consecutive passages intersected each other. Kenny argued that the conical diffuser inlet profile is more likely to shed vortices into the

diffuser that will result in higher performance due to a more stable flow field. The results do in fact indicate a performance improvement for scalloped diffuser inlet shapes.

Robert et al. (2003) investigated a diffuser comprising of circumferentially spaced discrete channels that partially define flow paths through the diffuser. The channels are angled such that they intersect adjacent channels, creating an annular semi-vaneless leading edge profile as seen in Figure 2.10. The leading edges are defined by the intersection of adjacent blade channels, creating an improved hub-to-shroud incidence match between impeller tip and diffuser inlet. Krige (2009) also investigated the effect of using an elliptical type leading edge profile over the conventional vaned diffuser type for the diffuser inlet. The vaneless space created by the intersection of adjacent D-shaped passages was chosen due to the advantageous match between the flow angles exiting the impeller tip and diffuser blade angles as pointed out by Robert et al. (2003). From Krige's experiments it was found that the curved leading edge matches the flow better than the straight leading edge at a lower speed. The engine was also able to spool up from zero to max thrust over a reduced time. However at maximum speed it was found that the leading edge angles needed to be increased slightly to better match the flow angles, since the design point was not taken at maximum speed, i.e. 120 krpm.

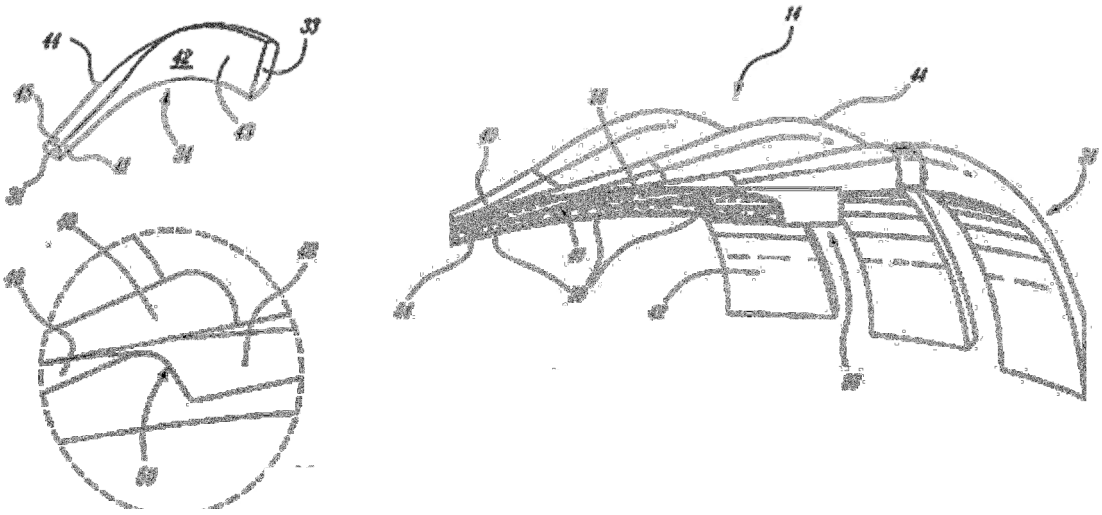

Figure 2.10: Circumferentially spaced discrete channels that partially define diffuser flow paths (Robert et al., 2003)

Many authors, such as Kenny (1972), Rodgers (1982) and Osborne and Japikse (1982), using straight walled diffusers report satisfactory results for a wide range of Mach numbers, including transonic levels. Other authors, such as Dean et al. (1970), Verdonk (1978) and Runstadler and Dolan (1973), investigated the effect of contouring the vane to control the flow in this region more accurately and believed that it would be more advantageous for transonic flow regimes. It is however not possible to argue that either of the vane shapes is superior to the other in a specific Mach number regime since no definitive information regarding this has been found. Campbell (1978) proposed a design of a centrifugal compressor diffuser in which he made use of radial vanes with non-axisymmetric

end walls. The idea of using non axisymmetric end walls was to reduce the vane-to-vane pressure gradient by allowing the flow to naturally flow along the suction surface of the vane. However Campbell's concept was proposed for subsonic diffusers and did not prove to be successful. Au (1991) further investigated the Campbell diffuser concept and stated that "*the flow is more sensitive to geometrical change than in incompressible flow*" and he further suggests that "*Campbell's approach may in fact have something to offer for supersonic diffusers which typically suffer from a strong inlet shock wave and the accompanying separation and high losses*". This may result in lower losses at the diffuser entrance for a Campbell diffuser design. Sullerey et al. (1983) also investigated the difference between straight and curved diffuser vanes. They concluded that higher values of pressure coefficient are achievable with straight diffusers, given the same area ratio and divergence angle. More losses occur on the curved diffuser vanes due to increased boundary layer growth.

Fox and Kline (1960) investigated the performance of a circular arc diffuser centerline. It is clear from their results that the straight centerline diffuser is superior to the curved centerline diffuser. Moore (1976) confirmed this observation. Similarly Sagi et al. (1967) studied a wide range of curved vane island diffusers and also found that the straight diffusers performed better than the curved diffusers.

Abdelwahab et al. (2007) provided a compressor system that operates more efficiently over a wider operating range by making use of a low solidity vaned airfoil diffuser for a centrifugal compressor, as seen in Figure 2.11. He suggested that each blade have a lean angle greater than zero. One fundamental characteristic of this type of diffuser according to him is "*the lack of a geometrical throat that permits it to increase the operating range without the risk of flow choking*". This type of diffuser geometry incorporates the larger operating range of vaneless diffusers with the reasonably good pressure recovery levels obtained by vaned diffusers, but without attaining the maximum pressure rise achievable.

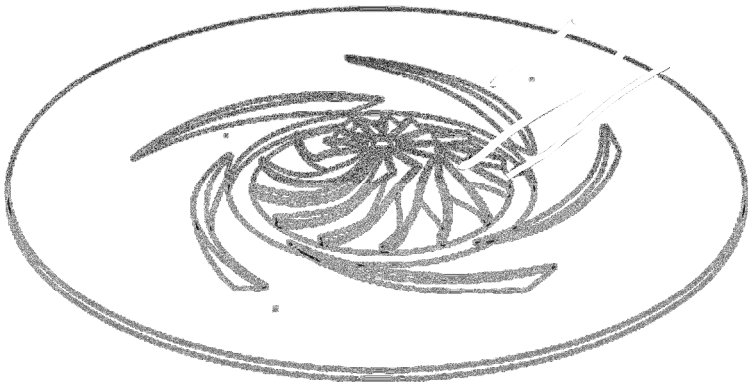

Figure 2.11: Low solidity, curved-vane diffuser (Abdelwahab et al., 2007)

Loringer et al. (2006) investigated the effect of boundary layer growth on the pressure and suction walls of the diffuser and suggested flow slots in the diffuser vanes. They claimed the flow slots in the diffuser vanes will minimize the growth

of a flow separation zone along the suction side. This is made possible by slots in the vanes allowing the flow to move from the pressure to the suction side. Their design is displayed in Figure 2.12.

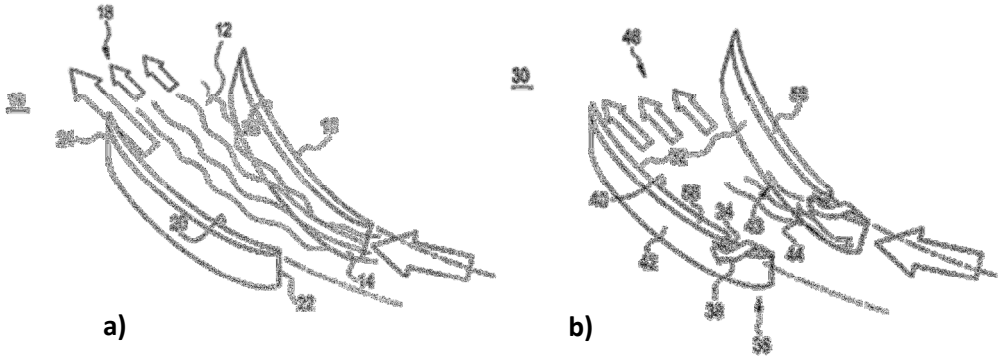

Figure 2.12: The effect of slots in the diffuser on flow separation (Loringer et al., 2006)

Loringer et al. explains that the amount of fluid passing over the slots in the vanes create a vortex that interferes with the boundary layer growth, thereby minimizing the growth of a flow separation zone along the suction side.

Figure 2.12 a) illustrates the large flow separation zone occurring on the suction side of the initial diffuser vanes. The flow separation zone results from a separation of the boundary layer on the suction side, leading to a lower velocity component than the working fluid through the diffuser channel and in effect reduces the overall fluid flow rate. Whitfield and Baines (1990) stated that in inviscid flow the velocity on the suction side is the highest. With respect to Figure 2.12 a) Loringer et al. (2006) explains that "*the flow separation zone creates a distorted exit flow from the compressor, reducing the efficiency of the compressor and potentially leading to surge and stall, with resultant damage to the compressor and/or a downstream turbocharged engine*".

Flow separation occurring on the suction side of the diffuser vanes can cause compressor stall, resulting in poor diffuser performance and poor compressor efficiency. However through experiments Loringer et al. (2006) found that "*by allowing a portion of the working fluid to flow through or over the vane from the pressure side to the suction side of the vane, the flow separation zone can be reduced or eliminated, efficiency increased and the likelihood of stall or surge reduced*". According to Loringer et al. "*the position and angle of the vane is chosen as a compromise between avoiding stalling of the flow and maintaining efficient pressure recovery for the angles of attack of the various incoming air flow streams that were anticipated to impinge upon the vane.*"

Airflow from the impeller is presented to the diffuser at high velocity with a certain incidence angle, creating a suction and pressure side on the vaned diffuser blades. The incidence angle is defined as the difference between the blade angle (β_3) and the flow angle (α_3) i.e. incidence angle $i = \beta_3 - \alpha_3$. Boundary layer growth according to Hagishimori (2005) increases near the hub and shroud ends of the diffuser vanes. It results from the negative incidence angle experienced near the

hub, *H*, and shroud, *S*, ends of the vanes, refer to Figure 2.13. He investigated means of reducing the pressure loss in the diffuser, by suppressing the generation of the boundary layer at the suction surface near the hub and shroud ends of the diffuser blades. He suggested "*that the suction surface be formed into a concave surface at least in the throat portion to suppress the generation of a boundary layer near the shroud surface and the hub surface*" as shown in Figure 2.13, accommodating the flow angles from hub to shroud.

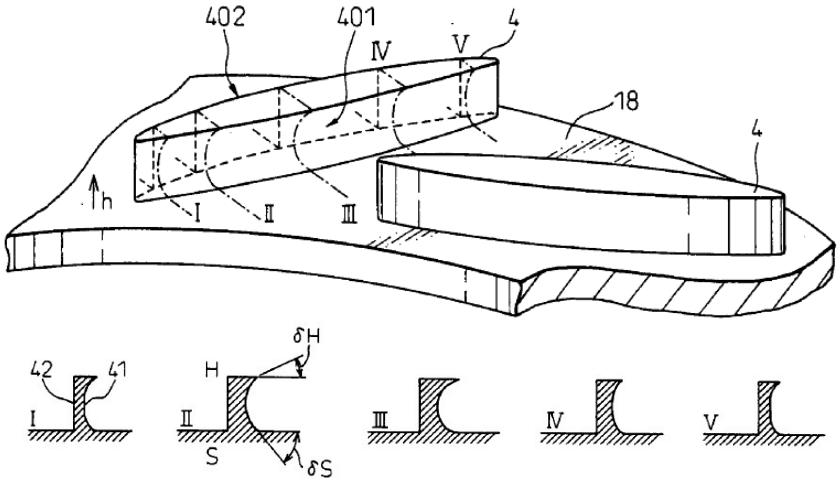

Figure 2.13: Concave diffuser suction surface (Hagishimori, 2005)

Au (1991) further agrees that the boundary layer on conventional diffuser side walls, caused by the adverse pressure gradient that exists at the diffuser inlet, grows rapidly due to the vane inlet geometry. Due to the range of operating conditions that needs to be accommodated when operating a gas turbine and the possibility of flow separation and boundary layer growth occurring at the leading edge, the specification of the correct blade angles is critical.

Teipel et al. (1987) investigated the effect of different diffuser stagger angles and their effect on the pressure distribution on different blade geometries in a transonic flow field. They observed that the flow was sensitive to increasing the blade stagger angle, with altered pressure conditions at the diffuser exit.

Moroz (2010) investigated the effect of changing the stagger angle of various vaned diffuser designs. He performed tests on three diffusers by changing the stagger angle of each. When increasing the stagger angle by 3 degrees, a slight increase in pressure recovery is observed, at the expense of flow rate, whereas by decreasing the stagger angle by 3 degrees, the flow rate is increased with a slight decrease in pressure. However Xi et al. (2007) found that by reducing the diffuser stagger angle, i.e. smaller than the design value, the maximum pressure ratio increases at the expense of compressor efficiency and flow rate. The diffuser vane stagger angle in a centrifugal compressor has a great influence on the flow and ultimately performance of the compressor. At large incidence angles, large vortices exist on the diffuser vane. An optimal diffuser stagger angle exists at a specific flow rate for flow through the compressor (Xi et al., 2007).

From various experimental investigations it is found that the inlet conditions of a vaned diffuser unquestionably influences the performance of the compressor and that the diffuser inlet stagger angle determines the safe operating flow range of the compressor. Cumpsty (1983) agrees that details of impeller-diffuser vane geometry are not as important as the poor performance delivered by high pressure ratio machines caused by mismatching of flow and vane angles. This can be singled out as one of the most influential factors in the diffuser's performance.

The number of vanes selected may vary and there is no clear preference as yet. However a low solidity at the diffuser inlet stabilizes the shock in the diffuser throat, caused by the high Mach numbers, at the expense of diffuser performance (Au, 1991). A low solidity radial diffuser decreases the total pressure loss of the compressor, whereas maximum pressure rise involves high aerodynamic loading on vane profiles, resulting in an increase in pressure losses.

According to Sayers (1990) the number of vanes in a diffuser is subject to the following considerations:

- The greater the vane number, the better is the diffusion but the greater is the friction loss.
- The cross section of the diffuser channel should be square to give a maximum hydraulic radius (cross-sectional area/channel perimeter).
- The number of diffuser vanes should have no common factor with the number of impeller vanes. This is to avoid resonant or sympathetic vibration.

e) Inlet Distortions

Velocity and total pressure distributions may cause distortions at the diffuser inlet that have a significant effect on the diffuser performance. An investigation on the effect of inlet distortion on diffuser performance was done by Al-Mudhafar et al. (1982). These authors concluded that the best pressure recovery occurs when there is no distortion present at the diffuser inlet. In addition their results also suggest that the inlet distortion is almost independent of Mach number. It is also observed that the diffuser exit blockage increases where inlet distortions exist (Wolf and Johnston, 1969). Misalignment of the flow entering the diffuser vanes will also result in distortions causing boundary layer growth and hence blockage in the region between the diffuser inlet and throat.

The flow leaving the impeller varies from hub to shroud, resulting in a small flow angle near the shroud and a larger angle near the hub. This is due to the varied tangential and radial momentum caused by the impeller. Bammert et al. (1983) investigated the effect of twisting the diffuser vane to better align it with the flow. Their results showed a better range and higher efficiency for a twisted vane configuration.

2.4.3 Diffuser Aerodynamic Parameters

General definitions of the different aerodynamic parameters are given in the following section. The most important aerodynamic parameters in the diffuser are assigned to the diffuser inlet.

a) Aerodynamic blockage

According to Japikse and Baines (1998) a diffuser with an effectiveness of 90% implies a diffuser inlet aerodynamic blockage of less than 3% and a value of less than 12% is required for an effectiveness of 67% to be realized.

Stratford and Tubbs (1965) identified the importance of boundary layer displacement thickness to the diffuser recovery process. From their observations it is clear that thin inlet boundary layers are beneficial for a high pressure recovery and that longer diffusers are also required as the inlet boundary thickness increases. Boundary layer displacement thickness is also known as aerodynamic blockage or simply blockage (B). The aerodynamic blockage refers to the fraction of the inlet passage area that is occluded or blocked by the displacement thickness on all walls (Japikse and Baines, 1998).

Many investigators regard aerodynamic blockage (B) as being one of the most important flow parameters that influence diffuser performance. Both the peak pressure recovery and the divergence angle decrease rather quickly as the aerodynamic blockage increases (Japikse and Baines, 1998).

b) Reynolds number dependence

Japikse and Baines (1998) reported that very little information is available for the performance of diffusers in laminar or transitional regimes and since the flow is highly turbulent at the diffuser vane inlet and Reynolds number is a relatively weak parameter to use as essential design criteria.

The significance of the Reynolds number is often regarded as a weak parameter for diffuser studies and therefore omitted. However for diffusers operating at a low aspect ratio, high inlet aerodynamic blockage or past the point of peak recovery, it is regarded as an important and necessary parameter (Japikse and Baines, 1998).

c) Inlet Mach number

Work done by Runstadler (1969) illustrated that there is no significant dependence on the Mach number for flows below a Mach number of 1. It follows that for diffusers operating above Mach 1 the Mach number plays a very important role in the design of the diffuser inlet and throat geometry. Accordingly, if the diffuser inlet geometry is not designed correctly it will create shock waves in the diffuser throat causing premature choking. However, for unstalled flows the Mach number is a relatively mild parameter to use (Japikse and Baines, 1998). For a Mach number between 0.2 and 1.0 there seem to be a linear change in performance (Japikse and Baines, 1998).

d) Inlet velocity profiles

Various research programs have revealed the significance and importance of the inlet velocity profile to the diffuser and it is regarded as an important aerodynamic parameter in any diffuser design. However, no convention has been developed to specify the diffuser inlet velocity profiles (Japikse and Baines, 1998). An integral scale as defined in Equation 2.1 is often used to define the velocity profile shape or distribution.

$$\alpha = \frac{1}{\overline{U}^3 A}\int_A U^3 dA \qquad 2.1$$

where U is the local velocity and $\overline{U}$ is the mean velocity required to satisfy continuity through area *A*.

e) Inlet Swirl

The flow exiting the impeller tip has a swirl component. This implies that the flow entering the diffuser has a relatively large tangential velocity component.

2.4.4 Overall Diffuser Performance Parameters

a) Static pressure recovery coefficient

The static pressure recovery coefficient indicates the percentage of inlet kinetic energy converted to static pressure rise through the diffuser. The static pressure recovery coefficient, C_p, of a diffuser is defined as the static pressure rise through the diffuser divided by the inlet dynamic head (Equation 2.2). This illustrates the fundamental purpose of a diffuser.

$$C_p = \frac{p_4 - p_3}{p_{t,3} - p_3} \qquad 2.2$$

$$C_{pi} = 1 - \frac{C_2^2}{C_1^2} \qquad 2.3$$

The ideal pressure recovery (Equation 2.3) is both a useful reference and can be used to deduce very important functional relationships (Japikse and Baines, 1998). For example, the pressure recovery in swirling flow for annular diffusers is influenced by a number of different variables. Using Equation 2.3 a general expression for the ideal pressure recovery in an annular diffuser can be defined with inlet swirl α_3 as (Japikse and Baines, 1998):

$$C_{pi} = 1 - \left(\frac{\overline{r_3}}{\overline{r_4}}\right)^2 \frac{tan^2\alpha_3 + (b_3^2/b_4^2)}{tan^2\alpha_3 + 1} \qquad 2.4$$

This equation indicates the importance of both the radius ratio and inlet-to-exit passage depth for effective pressure recovery. The swirl term α_3 can be suppressed by designing a diffuser with a large radius ratio and by using the law of conservation of angular momentum, $rC_\theta = constant$. This expression indicates that a maximum pressure recovery with respect to swirl will be achieved when

$b_3/b_4 = 1$ (Japikse and Baines, 1998). For this particular case Equation 2.4 can be reduced to Equation 2.3.

Pressure recovery in diffusers with unlimited radial space is frequently in the order of 0.5 to 0.7 at the best efficiency point, whereas in turbomachinery with a restricted radial length pressure recovery in the order of 0.2 to 0.5 is accepted (Japikse and Baines, 1998).

b) Diffuser effectiveness and efficiency

The diffuser effectiveness is defined as the relationship between the actual pressure recovery and the ideal pressure recovery:

$$E = \frac{C_p}{C_{pi}} \tag{2.5}$$

The effectiveness concept is very useful and handy when judging the level of performance of a new diffuser design when limited operating conditions are known. For compressible flow the diffuser efficiency is defined by

$$\eta_D = T_3 \left[\left(\frac{p_4}{p_3} \right)^{\frac{\gamma-1}{\gamma}} - 1 \right] \Big/ T_4 - T_3 \tag{2.6}$$

c) Total pressure loss coefficient

In addition to the static pressure recovery another important concern is the loss in total pressure over the diffuser. According to Japikse and Baines (1998) for all practical purposes the loss coefficient must refer to the entire flow field since the diffuser is a basic fluid dynamic element in a larger system. The most common loss coefficient definition is as follows:

$$K = \frac{\bar{p}_{t,3} - \bar{p}_{t,4}}{\bar{p}_{t,3} - \bar{p}_3} \tag{2.7}$$

where integrated mass averages are used across the diffuser inlet and outlet.
To conclude, three-dimensional flow calculations are becoming more feasible, accompanied by CFD packages, suggesting that the only realistic way to determine flow results is to use a three-dimensional technique.

Proper fluid flow matching between the impeller tip and the diffuser inlet minimizes flow losses or boundary layer growth in the compressor and improves the overall performance of the compressor.

It can be said that the four dominant factors that affect the performance of a vaned diffuser is:

- Inlet Mach number
- Aerodynamic blockage
- Incidence angle
- Solidity

3 NUMERICAL ANALYSIS

3.1 Introduction

To support and enhance the design process of the centrifugal compressor, both a 1-D mean stream surface model and a 3-D Computational Fluid Dynamic (CFD) software package is used. The initialization of the respective compressor geometries, as well as the 1-D and CFD modelling and techniques are discussed in the following chapter.

3.2 Review of the 1-D and 3-D CFD Software Packages

An in depth discussion of the 1-D and 3-D CFD software environments and the procedures followed for this thesis are included in Appendix A.

Aungier's (2000) one-dimensional centrifugal compressor software program, CompAero, is used to perform the 1-D analyses. CompAero is an aerodynamic design and analysis software system for centrifugal and axial flow compressors (Aungier, 2009) based on the theory of Aungier (2000). It uses basic thermodynamic and fluid dynamic principles, empirical models and key numerical methods to execute computations along a mean stream surface through each of the compressor stage components. CompAero has a variety of programs to use for compressor design, however only the CENCOM (**CEN**trifugal **COM**pressor) and VDDESIGN (**V**aned **D**iffuser **DESIGN**) programs were of interest for this thesis. The CompAero environment is discussed in Appendix A.1.

All compressor geometries, i.e. impeller, vaneless space and radial vaned diffuser, are specified in CENCOM as well as the initial flow conditions. CENCOM computes and saves performance prediction results and uses them to display various performance maps for the compressor as well as the performance of each stage.

VDDESIGN forms part of the design procedure. The flow chart of the design procedure followed in VDDESIGN is shown in Figure A.1. It has the option to perform design point or off-design performance analyses as well as blade-to-blade flow analyses for direct evaluation of the blade loading. Various important design parameters are specified in VDDESIGN that determine the final diffuser design and its design point performance.

FINE™/Turbo v8.9-1 by NUMECA™ International (Intl.) is the CFD software used in this thesis. Three separate software systems are used in FINE™/Turbo for the CFD analysis as follows:

1. The *pre-processor* is a combination or integration of two separate programs, namely **I**nteractive **G**eometry modeller and **G**rid generator (IGG™) and **Auto**mated **Grid** generator (AutoGrid5™).
2. The *solver* system in FINE™/Turbo uses EURANUS™ (**EUR**opean **A**erodynamic **N**umerical **S**imulator) to solve computations.
3. The *post-processor* is a Computational Field Visualisation software program known as CFView™.

All three systems have been integrated into one package by NUMECA Intl. called **F**low **IN**tegrated **E**nvironment (FINE™/Turbo). The three systems mentioned above are discussed in further detail in Appendix A.2. The entire centrifugal compressor mesh quality and convergence criteria followed during the modelling procedures, as stipulated by NUMECA™ (Intl.), are included in Appendix A.2.

3.3 Compressor Modelling Procedure for CFD analysis

In order to understand the modelling techniques used in this thesis, the following section will use the original BMT 120 KS centrifugal compressor as a guideline. All other compressor models are similar in concept and are included in Appendix D.

To investigate and analyze the diffuser performance in a centrifugal compressor the inlet flow behavior for the diffuser is required. The diffuser is therefore dependent on the upstream component geometries and their flow behavior. The impeller geometry as well as the hub and shroud contours are required to perform a diffuser performance analysis. The hub-and-shroud contours and impeller geometry are discussed in Sections 3.3.2 and 3.3.3 respectively.

To perform a full CFD analysis on the current BMT 120 KS compressor, a Computer Aided Design (CAD) model with accurate geometry is required.

The KKK K27.2 impeller was scanned by an optical scanner and converted to a parasolid file to be imported and rebuilt in Solidworks (see Figure 3.1). The radial and axial diffuser geometries are obtained from the BMT 120 KS owner and designer, A. Baird (2011), and remodelled in SolidWorks. The complete BMT 120 KS gas turbine CAD file was drawn up and assembled in Solidworks. All compressor components required for CFD modelling were exported as IGES files from Solidworks to Rhinoceros3D (Rhino3D). Rhino3D is a surface modelling program used to divide the selected curves into several points that represent the curves. These curves are then exported to AutoGrid5™ in a **.geomTurbo* file format. The **.geomTurbo* file contains the respective compressor geometry points to create the model in AutoGrid5™. The points are referenced to either a Cartesian or cylindrical coordinate system. The centrifugal compressor geometry as seen in Solidworks and Rhino 3D are shown in Figures 3.2 and 3.3 respectively.

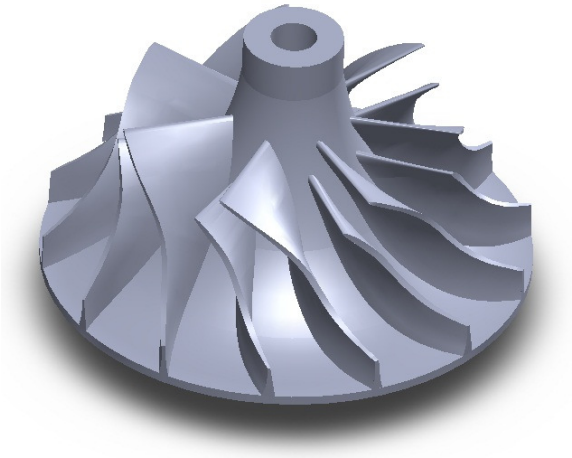

Figure 3.1: KKK K27.2 – 2970 M_AA_ Impeller

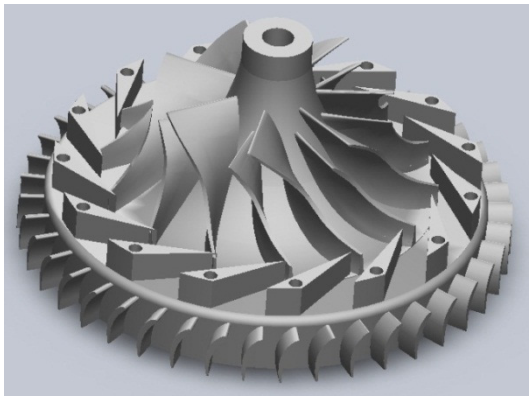

Figure 3.2: SolidWorks compressor model

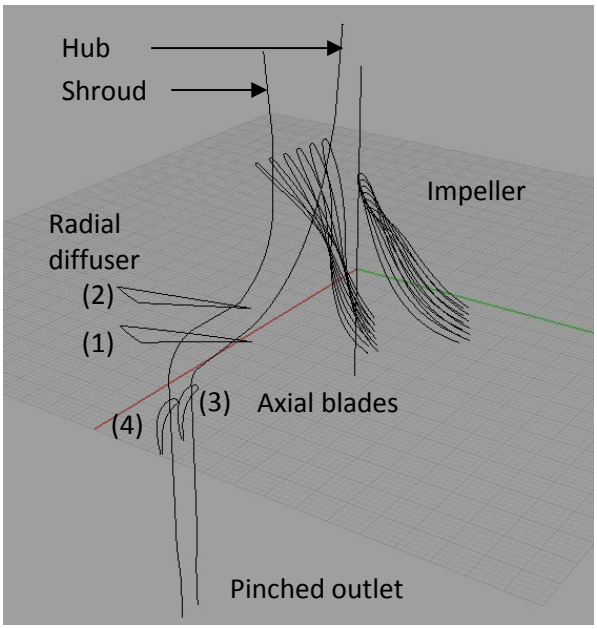

Figure 3.3: Compressor curves in Rhinoceros3D

3.3.1 Computational Domain

The computational domain for CFD analysis of the centrifugal compressor stretched from the impeller inlet to the axial blade outlet. The inlet is located 20 mm upstream of the impeller main blade leading edge and is modelled as a surface parallel to the x-y plane in AutoGrid5™. The outlet is placed downstream of the axial blades. The initial location of the outlet resulted in flow recirculation and unstable simulations. This is further discussed in Section 3.3.2. It should also be mentioned that only the flow performance over the compressor section is required and therefore the combustion chamber is not included in this analysis.
AutoGrid5™ requires the **.geomTurbo* files of the compressor hub, shroud and blades that make up a stage in the flow passage. All compressor stages or rows are created in AutoGrid5™ with its respective rotor-stator interface between the impeller and radial diffuser. The complete model is reopened in IGG™ to specify

the stator-stator interface between the radial diffuser and axial blades by means of a full non-matching mixing plane, as well as its periodicity.

A screenshot of AutoGrid5™'s user interface displaying the BMT 120 KS centrifugal compressor with the three main components, i.e. impeller with splitter blades (1), radial diffuser (2) and axial blades (3) shown in Figure D.1. The development of each component is discussed separately below.

3.3.2 Hub and Shroud Contours

The compressor hub and shroud contours are each represented by a single continuous curve from the impeller inlet to the axial blade outlet. AutoGrid5™ revolves these curves about the z-axis (axis of rotation) to create surfaces for meshing.

During initial FINE™/Turbo compressor simulations flow separation was observed behind both the radial and axial diffuser vanes. This caused recirculation in the flow at the compressor outlet resulting in unstable simulations, i.e. negative pressures and densities were calculated by the solver and caused the solver to stop prematurely. This phenomenon was overcome by firstly increasing the axial length of the hub and shroud curves, creating a lengthened vaneless space between the axial diffuser vanes and the model's outlet, and secondly by pinching the outlet slightly to constrict the flow, as depicted in Figure 3.3. The additional vaneless space causes the flow to recuperate before reaching the outlet boundary. The moderately pinched outlet increases the velocity gradient, reducing the possibility of flow to re-enter the compressor outlet boundary and prevents the solver from stopping prematurely.

3.3.3 Impeller Modelling

The KKK K27.2 (K27.2 – 2970 M_AA_) impeller consists of 7 main and 7 splitter blades as seen in Figure 3.1. This specific impeller is designed for application in an automotive turbocharger. The original impeller diameter was 74 mm, but it has been modified to a diameter of 70 mm for use in the micro gas turbine by cutting away a portion of the trailing edge. The main impeller dimensions are indicated in Table 3.1.

Pairs of impeller blades, i.e. 1 main- and 1 splitter- blade, are divided into 6 equally spaced curves per pair from hub to shroud, representing the blade geometries in AutoGrid5™, as shown in Figure 3.4. To reduce the mesh size and computational time only one pair of blades are developed and meshed in AutoGrid5™, by making use of axial symmetry. The impeller structured mesh is created with 73 flow paths from hub to shroud on the surface of revolution. The impeller blade-to-blade (B2B) grid layouts for the main and splitter blades are shown in Figures 3.5 and 3.6 respectively.

The cell distributions near the hub, shroud and blade boundaries are densely clustered to achieve low y^+ values in order to accurately capture the large velocity gradients. In the boundary layers the y^+ values for the impeller mesh are well within the acceptable viscous sublayer range i.e. between 0 and 10. There are however a few cells that overshoot to a maximum y^+ value of 12 as seen in

Figure 3.9. This occurs at the impeller tip and according to NUMECA Intl. (2011b) "*blade tip clearances are meshed with uniform spanwise node distributions, resulting in y+ values that will tend to be higher within the gap than elsewhere in the computational domain nearwall regions*". NUMECA Intl. (2011b) also states that "*this should not raise concern as the tip clearance flow consists of thoroughly sheared vertical fluid that undergoes significant acceleration and is therefore quite different than a standard boundary layer*".

Table 3.1: KKK K27.2 Impeller dimensions

Parameter	Value
$r_{1hub}\ (mm)$	9.1
$r_{1shroud}\ (mm)$	26.1
$r_2\ (mm)$	35.0
$b_2\ (mm)$	6.0
β_1	40.0˚
β_2	59.6˚

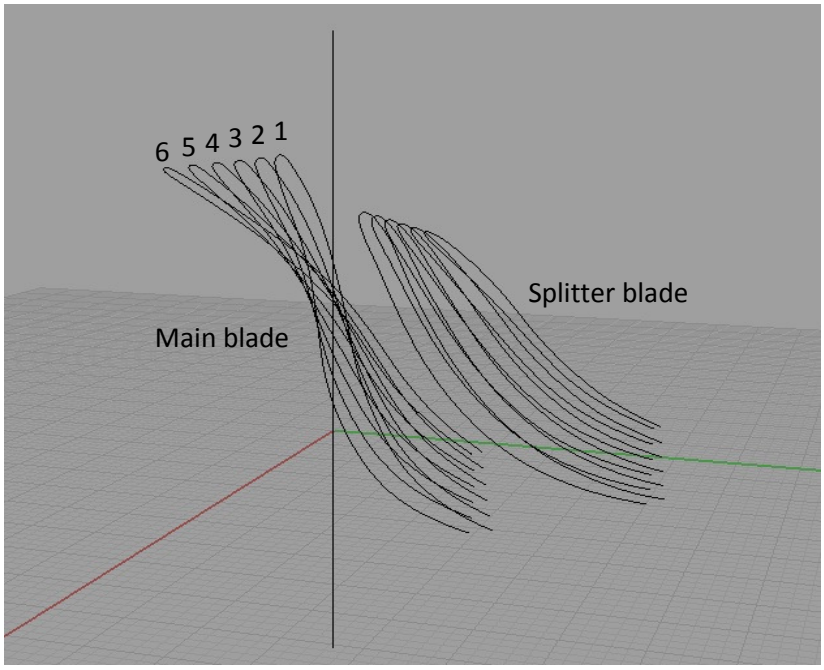

Figure 3.4: Screenshot of the impeller curves as seen in Rhinoceros3D

H&I mesh topology (as described in Appendix A) is used with a *low inlet type* angle and *normal outlet type* angle for the impeller blades. A tip gap of 0.2 mm is implemented between the rotating blade edges and shroud at the leading and trailing edges; and a periodicity of 7 is specified for the number of mesh volumes. The coarse impeller mesh is indicated in Figure D.2.

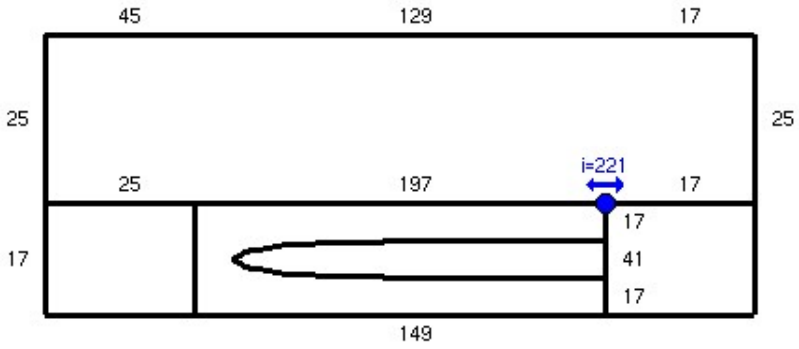

Figure 3.5: Main blade B2B grid layout

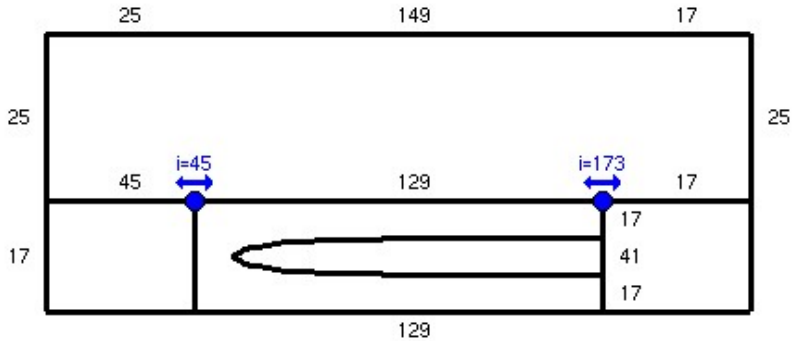

Figure 3.6: Splitter blade B2B grid layout

The impeller mesh consists of 2 333 952 grid points with the following mesh quality criteria (see Appendix A for an explanation of the mesh quality criteria):

Table 3.2: Impeller mesh quality criteria

Quantity	Required value	Impeller Mesh
Orthogonality	> 24˚	28.31˚
Aspect Ratio	< 2000	218.63
Expansion Ratio	< 2.5	2.66
Angular Deviation	< 40˚	15.46˚

The number of cells that exceed the required expansion ratio value of 2.5 is found to be 494 cells out of a total of 54 364 800 cells. This represents only $9.1 \cdot 10^{-4}$ % of the total number of cells and is therefore considered acceptable.
A subsonic inlet boundary is assigned to the impeller inlet, whereas the impeller outlet is assigned to a *Non Reflecting 1D* rotor-stator interface between itself and the radial diffuser. The remaining boundaries that form part of the axisymmetric model are set to a periodicity of 7.

3.3.4 Radial Diffuser Modelling

The BMT 120 KS turbine makes use of 15 thick vaned radial diffuser vanes. Due to its simple geometry only the radial diffuser hub (1) and shroud (2) curves are required by AutoGrid5™, as depicted in Figure 3.3, to generate the vanes for meshing. The radial diffuser structured mesh is created with 57 flow paths from hub to shroud on the surface of revolution, with streamlines more densely spaced near the solid wall boundaries for low y^+ values. The y^+ values for the radial diffuser mesh are well within the acceptable viscous sublayer range. The radial diffuser B2B grid layout is shown in Figure 3.7.

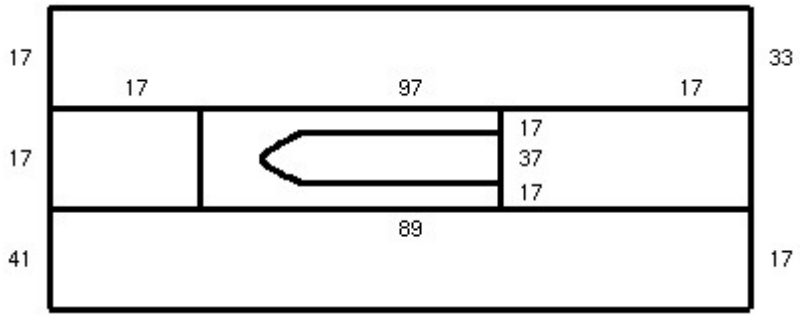

Figure 3.7: Radial diffuser B2B grid layout

The *default* B2B mesh topology is used in AutoGrid5™ with a *high inlet type* angle and *low outlet type* angle. The radial diffuser mesh consists of 3 646 575 grid points with the following mesh quality criteria:

Table 3.3: Radial diffuser mesh quality criteria

	Mesh quality criteria	Radial Diffuser Mesh
Orthogonality	> 24˚	29.56˚
Aspect Ratio	< 2000	80.72
Expansion Ratio	< 2.5	1.82
Angular Deviation	< 40˚	7.83˚

The radial diffuser inlet boundary is assigned to a *Non Reflecting 1D* rotor-stator interface between itself and the impeller as previously mentioned; and the radial diffuser outlet is assigned to a *FNMB* stator-stator interface between itself and the axial diffuser. The remaining boundaries that form part of the axisymmetric model are set to a periodicity of 3 due to the full non matching boundary (FNMB) mixing plane requirements as described below.

It is required to create a FNMB mixing plane between the 15 radial and 42 axial diffuser vanes to connect the two non-matching mesh boundaries. IGG™ is used to execute the FNMB connections by redefining its boundary conditions.

According to NUMECA (2011a) "*all patches defining the connection must have the same periodicity information for periodic FNMB connections*". This is achieved by determining the largest common denominator between the number of vanes of each diffuser and meshing the minimum amount required. Therefore 5 radial diffuser vanes and 14 axial blades are meshed for the BMT 120 KS 3-stage centrifugal compressor with a FNMB mixing plane connecting the two stages. Full non matching boundary (FNMB) connections are fully supported by the NUMECA flow solver, EURANUS. The 5 meshed radial diffuser vanes are shown in Figure D.3.

3.3.5 Axial Blade Modelling

The axial diffuser meshing approach is in essence very similar to that of the radial diffuser. Again, only the axial diffuser hub (3) and shroud (4) curves are required by AutoGrid5^{TM}, as seen in Figure 3.3, to create the blades for meshing. The axial diffuser has a structured mesh with 57 flow paths from hub to shroud on the surface of revolution, with streamlines more densely spaced near the solid wall boundaries for low y^+ values. The axial blade's B2B grid layout is shown in Figure 3.8.

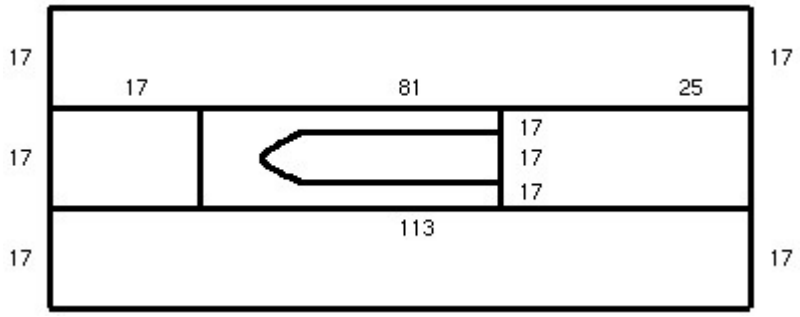

Figure 3.8: Axial blade B2B grid layout

The *default* B2B mesh topology is used in AutoGrid5^{TM} with a *high inlet type* angle and *normal outlet type* angle. The axial diffuser mesh consists of 13 443 906 grid points with the following mesh quality criteria:

Table 3.4: Axial blades mesh quality criteria

	Mesh quality criteria	Axial blade mesh
Orthogonality	> 24˚	37.59˚
Aspect Ratio	< 2000	218.45
Expansion Ratio	< 2.5	2.39
Angular Deviation	< 40˚	4.24˚

The axial diffuser inlet is assigned to a FNMB stator-stator interface between itself and the radial diffuser, as described in Section 3.3.4. The axial diffuser

outlet is also the three-stage centrifugal compressor model's outlet. The remaining boundaries that form part of the axisymmetric model are set to a periodicity of 3 due to the FNMB mixing plane requirements. It is required to mesh 14 axial vanes as seen in Figure D.4. The required mesh passages for the BMT 120 KS 3 stage centrifugal compressor that represent the full model is shown in Figure D.5.

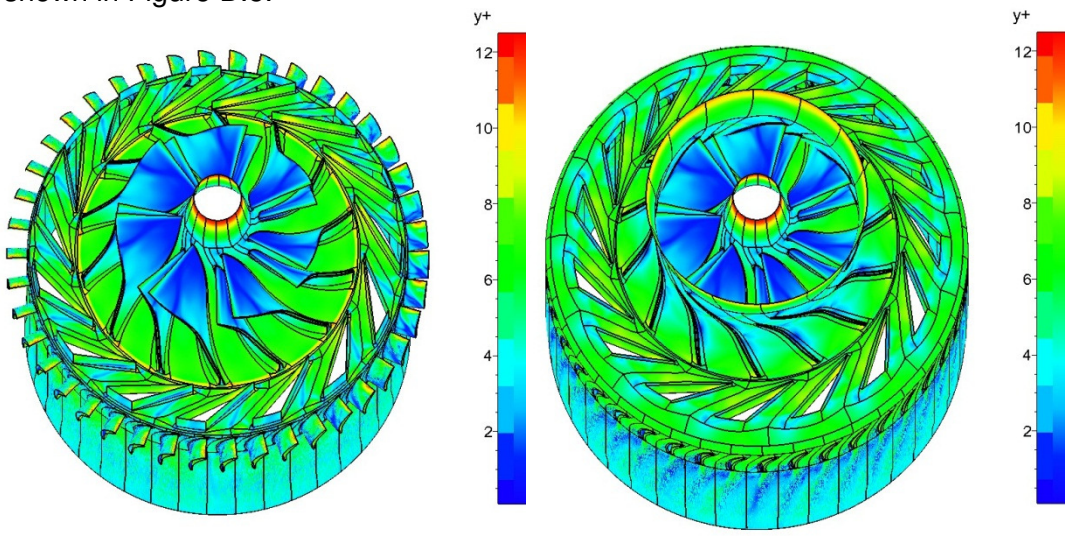

a) Unshrouded b) Shrouded

Figure 3.9: y^+ values of the original BMT 120 KS compressor at 0.323 kg/s

3.4 CFD Computational Parameters

The parameters required to set up and solve steady state flow simulations are briefly discussed in this section.

3.4.1 Fluid Model

FINE^{TM}/Turbo has a number of predefined fluid or gas types. For this study air is used as the operating gas. The air property selected in FINE^{TM}/Turbo has perfect gas properties with constant specific heats. Le Roux (2010) advised to use the calorically perfect gas, *AIR (Perfect)*, instead of the incompressible gas, *AIR (Incompressible)* or real gas, *AIR,* for low speed computations, due to the decreased computational time required to give rather similar results. Both the real gas and calorically perfect gas was simulated at the same conditions and proved to give similar results with the calorically perfect gas performing the best.

3.4.2 Flow Model

Steady flow is assumed for the centrifugal compressor investigation. FINE^{TM}/Turbo's Turbulent Navier-Stokes equations are used with the one-equation Spalart-Allmaras turbulence model to solve the flow equations. The Spalart-Allmaras turbulence model is considered to be more robust, performing

better than algebraic turbulence models and requires less computational memory than the k - ε two-equation turbulence models (de Wet, 2011).

The reference temperature and pressure values used in FINE^{TM}/Turbo were measured in the test facility to be 283 K and 100 kPa.

3.4.3 Rotating Machinery

The impeller is set to a specific rotational speed to compute the operating flow range for a specific constant speed line. The compressor is simulated at the following rotational speeds: 70, 80, 90, 100, 110 and 120 krpm. The radial diffuser and axial blades are kept stationary at 0 rpm. For the rotor-stator interface between the impeller and radial diffuser a Non-Reflecting 1D approach is used. This approach is based on a characteristic analysis of the linearized Euler equations. The Non-Reflecting 1D approach is recommended when wave reflection is observed at the interface, which can occur when the interface is close to the blade (NUMECA International, 2011d).

3.4.4 Boundary Condtitions

The boundary conditions are composed of four main boundary groups:

1. Inlet

A subsonic inlet boundary is assigned to the compressor inlet. The flow is assumed to enter the compressor in an axial fashion and is therefore constrained to the z-axial direction (negative z-direction) in a cylindrical coordinate system. In order to constrain the velocity components (V_r, V_t, V_z), a V extrapolated velocity boundary condition is assigned. The absolute total pressure and temperature quantities are defined at the inlet as indicated in Table 3.5.

Table 3.5: Inlet boundary imposed quantities

Property	Value
$V_r/\|V\|$	0
$V_t/\|V\|$	0
$V_z/\|V\|$	-1
Absolute Total Pressure	100 kPa
Absolute Total Temperature	283 K
Turbulent Viscosity	0.0001 m^2/s

2. Outlet

The outlet boundary is assigned to an averaged static pressure imposed boundary condition. This boundary condition is used since the approximation of uniform static pressure at the outlet is not an accurate approximation for the physical pressure distribution. The pressure profile for the average static pressure condition is extrapolated from the interior field (NUMECA International, 2011d). The mass flow decreases as the static pressure is increased for

consecutive simulations to obtain the compressor operating surge-to-choke range. It is also noted that the operating range decreases as the discharge pressure is increased.

3. Periodic

All periodic boundaries are defined in AutoGrid5™ and IGG™ and automatically assigned in FINE™/Turbo when the mesh file is imported.

4. Solid

The solid boundaries include the impeller blades, diffuser vanes, axial blades and hub and shroud contours. The impeller hub and blades are modelled as rotating solids. The rotational speed of these solids is set to the same speed as the required impeller speed.

3.4.5 Multigrid Parameters

FINE™/Turbo's flow solver, EURANUS, makes use of a multigrid strategy to efficiently solve flow equations on different grid levels. This strategy is useful for obtaining initial conditions to computations and to accelerate convergence by using the coarser grid level solutions as an initial solution to finer grid levels. For the 3-stage centrifugal compressor model three grid levels are used, namely 000, 111 and 222, to solve the flow solution. Grid level 000 is regarded as the finest grid level.

The EURANUS flow solver is set to specific convergence criteria per grid level and will only start interpolating the next finer grid level once these criteria have been met. This process allows for a more robust simulation on the finest grid level. The convergence criteria for the first two coarser grids are set to 1000 cycles per grid level. The next finer grid level will be initiated either when the solver reached 1000 iterations or when the global residual reaches a value of *-5*. The central spatial discretization scheme is applied to all grid level simulations. The convergence criteria for the finest grid level (000) is set to a maximum of 6000 iterations or stops computing when the global residuals reach a value of *-9*. The solver is set to single precision as discussed in Section 4.3.

The midspan B2B mesh of the 3 stage centrifugal compressor on three different grid levels is shown in Appendix D.

3.4.6 Expert Parameters

The following expert parameters were used in FINE™/Turbo:

1. IDISTN (1); this parameter is used in the calculation of the wall distance in the turbulence models.
2. IWRIT (1); this parameter influences the type of output written in the **.mf* extension file, i.e. mass flow through rotor/stator interfaces.
3. LOCCOR (1); this is a parameter used in the mixing plane approach and is used to activate the local enthalpy correction.
4. TORRO (1); this parameter is used to compute the force and torque on the part which is defined through an area defined rotation.

3.4.7 Output Variables

The following output variables are computed for each simulation:

Thermodynamic

- Static and total absolute temperature and pressure, density and entropy

Velocities

- Absolute velocity vectors, absolute velocity magnitude, absolute Mach number
- Relative velocity vectors, relative velocity magnitude, relative Mach number

Solid data

- y^+ value in the first inner cell

Planes are created in the flow passages of the computational domain to compute and obtain the magnitudes of various weighted integrals.

During a simulation various residuals can be viewed to monitor the convergence, namely:

1. Global residual
2. Pressure ratio
3. Efficiency
4. Inlet/outlet mass flow

3.5 Numerical Analysis Conclusion

One and Three- dimensional software systems developed for turbomachinery applications reduce both cost and design time and should unquestionably be used in the design process. However, care should be taken when using these systems since user errors can easily creep in and influence computational results. It is therefore necessary and important to verify and validate data with experimental results.

4 EXPERIMENTAL APPARATUS

4.1 Introduction

The work detailed in this chapter involves the experimental performance evaluation of the centrifugal compressor in the Baird Micro Turbine (BMT 120 KS). The aim of the experimental setup is to record the engine performance at various positions over the compressor and use it as reference experimental work for numerical validation and design work. In addition, the results obtained for the original BMT 120 KS diffuser (Diffuser 1) act as reference work for the new diffuser configurations. The engine test facility, instrumentation and processing procedures are discussed in this chapter.

4.2 Engine Test Setup

The experimental tests involve the entire BMT 120 KS gas turbine. The experiments are performed in a test laboratory at ambient temperature and pressure conditions that vary slightly year round. Diffuser 1 was tested at ambient temperature and pressure conditions of 283 K and 100 kPa respectively and Diffuser 2 and 3 were tested at 294 K and 100 kPa respectively. The 1-D and CFD validation procedures are performed at 283 K and 100 kPa. The engine is positioned on a test bench such that the exhaust gasses are fired through an extraction hole in the laboratory to prevent the engine from reusing exhaust gasses that can affect the engine performance.

4.2.1 Test Bench

A rigid test bench is required for measurement accuracy and test repeatability. The test bench is designed with two 4.5 mm thick U-shaped aluminium frames placed on top of each other as seen in Figure 4.1. These aluminium frames will be referred to as “beds” in this section. The base bed is slightly larger than the runner bed and is fixed to a rigid table in the laboratory. Ball bearing runners are placed between the vertical walls of the beds, allowing the runner bed to slide in a horizontal (x) direction for thrust measurement. The engine is placed near the back of the runner bed to allow a bell-mouth and a circular inlet duct to be attached to the engine inlet and runner bed. This allows the engine and bell-mouth to slide as a fixed unit when the engine is running. The function of the bell-mouth and circular duct combination is twofold. Firstly, it is used to measure the engine mass flow rate (see Section 4.2.2) and secondly, it provides a more stable and laminar airflow distribution at the engine inlet, due to the length of the circular duct ($L = 4D$). This reduces successive testing errors and also eliminates the effect of any external flow factors that may occur upstream of the engine inlet that are not accounted for in the 1-D or 3-D analyses. The runner bed houses the engine by means of engine brackets fixed to the sides of the bed. The circular duct is sealed over the engine housing with an O-ring type rubber seal to prevent

air leakage and is smoothly joined to the bell-mouth to prevent any disturbance of the airflow.

1. Test setup inlet
2. Bell-mouth
3. Circular duct
4. Base bed
5. Runner bed
6. Engine
7. Load Cell, thrust measurement
8. Engine Outlet

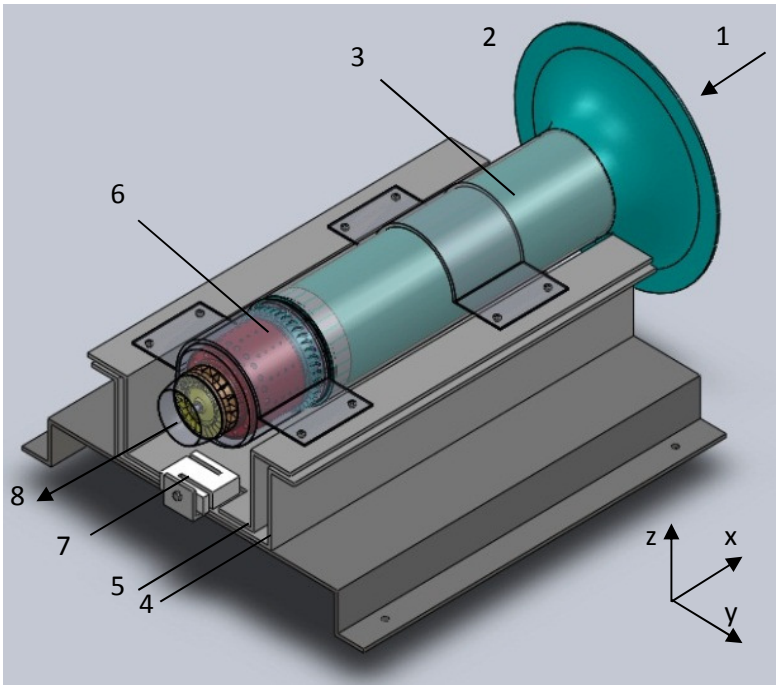

Figure 4.1: Test bench setup

The bell-mouth has dimensions of $d_1 = 280\,mm$, $d_2 = 102\,mm$ and $L = 440\,mm$, with reference to Figure 4.2.

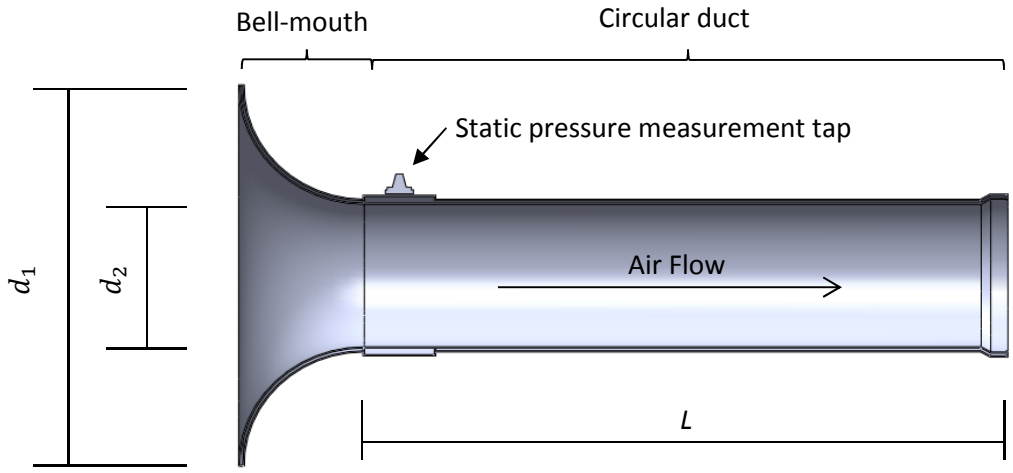

Figure 4.2: Section view of bell-mouth and circular duct geometry

4.2.2 Instrumentation of the Test Facility

The engine thrust, mass flow rate, rotational speed, fuel consumption, exhaust gas temperature and various static pressure measurements over the compressor are measured during a single experimental run. Figure 4.3 shows a schematic

illustration of the instrumentation used in this test facility. The calibration procedures of the measurement equipment are included in Appendix E.

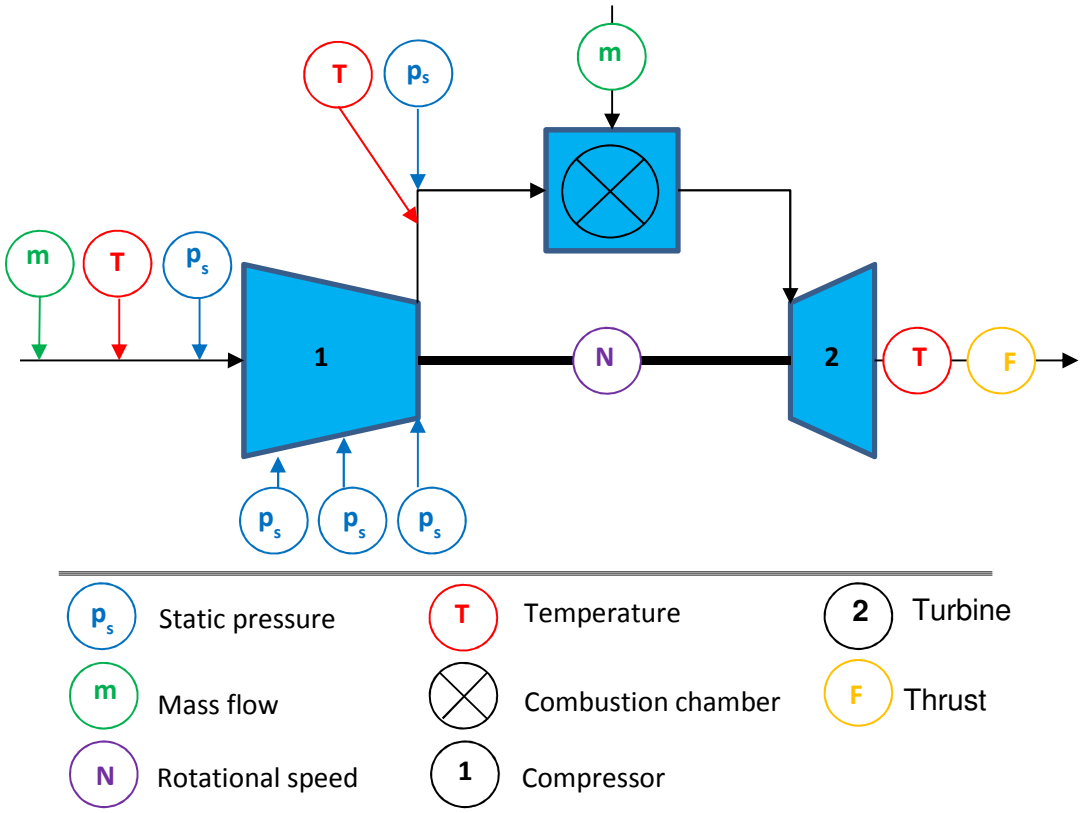

Figure 4.3: Instrumentation locations over the BMT 120 KS gas turbine

A Hottinger Baldwin Messtechnik (HBM) spider 8, 4.8 kHz/DC data logger, as depicted in Figure 4.4, with 8 Input/Output channels is used to measure the engine thrust, various static pressures and fuel consumption. The data is sampled at a rate of 50Hz. The data logger is connected to a personal computer (PC) that displays the measured data digitally and saves it in **.xls* (Microsoft Excel) format for further processing.

Figure 4.4: HBM Spider 8 data logger

a) Engine Mass Flow Rate

The air mass flow rate through the engine is deduced from the difference between the ambient pressure and the static pressure measured in the bell-mouth, as shown in Equations 4.1 and 4.2. The location of the three static pressure measurement taps in the bell-mouth is shown in Figure 4.5. The three measurements are combined and an average static pressure value is measured by the pressure transducer.

When a fluid approaches its speed of sound or operates in this region, density changes become significant and the flow is termed compressible (White, 2006). The Mach number is regarded as being the dominant parameter in compressible flow analysis (White, 2006), and is therefore firstly evaluated for the airflow through the inlet duct to determine the method for mass flow calculation, i.e. whether the flow should be treated as compressible or incompressible.

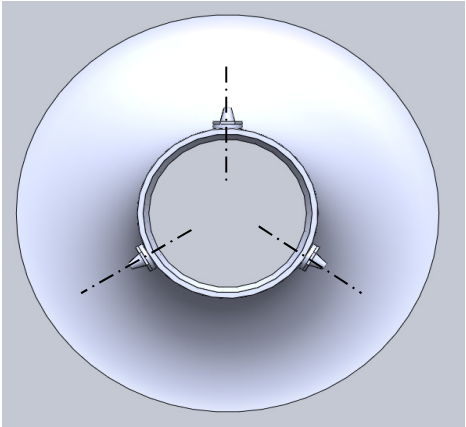

Figure 4.5: Static pressure taps in the circular duct

The velocity component through the inlet duct (C_{duct}) is initially determined by measuring the static pressure difference (Δp) between the bell-mouth and the ambient pressure, and solving for the velocity component in Equation 4.1:

$$\Delta p = \frac{1}{2}\rho {C_{duct}}^2 \qquad 4.1$$

Flow with a Mach number less than 0.3 can be treated as incompressible flow where density effects are negligible (White, 2006). The Mach number is calculated to be 0.08 in the bell-mouth and the flow is therefore treated as incompressible. The mass flow rate is determined from:

$$\dot{m} = \rho_{duct} C_d A_{duct} \left[\frac{2\Delta p/\rho_{duct}}{1-\beta^4}\right] \qquad 4.2$$

The BMT 120 KS delivered a mass flow rate of 0.288 kg/s at 120 krpm.

b) Pressure Measurements

Static pressure is measured at various positions over the compressor. The positions are as follows, as shown in Figures 4.3 and 4.6:

1. *Engine inlet*; the static pressure is measured on the circumference of the circular duct behind the bell-mouth, upstream of the engine inlet, (see Figures 4.2 and 4.5).
2. *Behind the impeller tip*; a hole with a diameter of *0.5 mm* is drilled in the shroud wall of the diffuser near the impeller tip at a radius of *36.5 mm.*

3. *Diffuser throat*; similar to 2 above, a hole with a diameter of *0.5 mm* is drilled in the shroud wall near the throat of the radial diffuser, at a radius of *40 mm.*
4. *Radial diffuser vane exit*; similar to 2 and 3 above, a *0.5 mm* hole is drilled in the shroud wall near the radial vane exit, at a radius of *45 mm.*
5. *At the compressor outlet*; a brass tube with inner diameter *0.6 mm*, is placed flush with the axial blade outlet.

The static pressure at *position 1* is measured by means of an HBM PD1/0.1 bar differential pressure transducer. The differential pressure measurement is taken at three equi-spaced locations on the circumference of the circular duct. These three locations are joined by pneumatic Festo tubes to produce an averaged static pressure measurement and this value is then used to calculate the mass flow rate as discussed earlier. The PD1/0.1 bar differential pressure transducer is connected on one side to the pneumatic tube and the other pressure input is left open to the atmosphere. The pressure transducer has a range of 10kPa (0.1 bar) and an accuracy of ± 0.25%.

Positions 2, 3, 4 and 5 make use of HBM P8AP 10 bar pressure transducers to measure the static pressure. Due to the small size of the engine and the electronics mounted in the engine cowl, it was difficult to access more than one diffuser passage for static pressure measurements. The location of positions 1, 2, 4 and 5 are the same for all the diffusers, i.e. at similar radii. However, position 3 varies as the location of the throat varies for each diffuser design. The HBM P8AP pressure transducers have an accuracy of 0.3% with a repeatability of 0.1%.

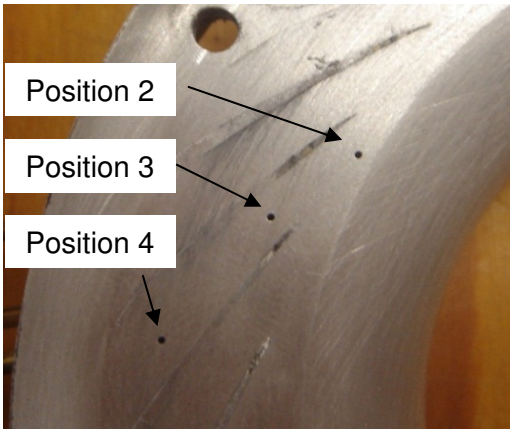

Figure 4.6 Static pressure measurement holes in the diffuser shroud wall

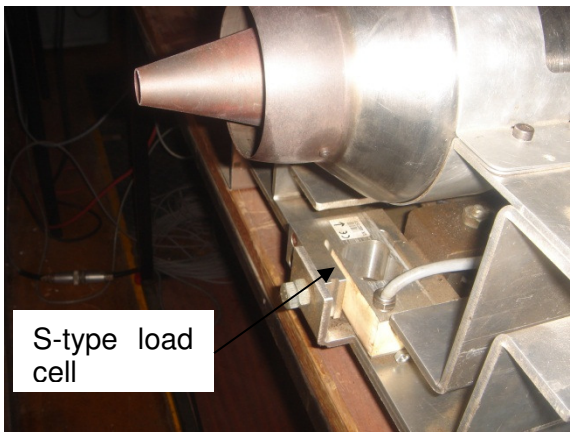

Figure 4.7: *HBM RSCC S-type 50kg* load cell between the stationary base- and sliding runner- beds

The 0.5 mm drilled holes at positions 2, 3 and 4 are each sealed with a bronze tube and connected to a silicon pipe that fits over a nipple on the pressure transducer.

c) Thrust Measurement

Thrust is measured by placing a *HBM RSCC S-type 50kg* load cell between the stationary base- and sliding runner- beds as indicated in Figures 4.1 and 4.7. As the engine spools up and develops thrust it drives the runner-bed forward, pulling the load cell, resulting in a thrust reading in Newton on the PC. The *HBM RSCC S-type* load cell has a sensitivity tolerance of ± 0.25% and is calibrated with a spring loaded weight scale. The thrust measurement system is repeatable and returns to zero after every experimental run.

d) Temperature Measurement

The ambient temperature is measured before every experimental run with a thermocouple placed near the engine inlet. The air temperature through the engine is measured at 3 possible locations during operation. The inlet air temperature is measured at the impeller inlet by means of a K-type thermocouple that is connected to a data acquisition (DAQ) logger and display the temperature output digitally on the PC. A similar K-type thermocouple is mounted behind the axial diffuser blades, measuring the compressor exit temperature. The third temperature probe is placed behind the axial turbine wheel, measuring the Exhaust Gas Temperature (EGT) of the engine. The GSU has the ability to abort any operation when the EGT exceeds a certain set material temperature limit, i.e. *1000 ˚C.* All temperature probes display values digitally, either on the GSU or on the PC. K-type thermocouples are used due to their high accuracy and reliability. The K-type thermocouples are accurate to within ± 2.2˚C with a sensitivity of 41 μV/˚C. The temperature between the impeller tip and radial diffuser exit cannot be measured due to limited accessibility and is therefore calculated numerically from the measured data.

e) Impeller Rotational Speed Measurement

The engine rotational speed is determined by means of two small magnets placed opposite each other in the base of the impeller hub and measured with magnetic speed sensors placed in the engine cowl. The GSU is programmed to adjust the fuel pump voltage that controls the fuel flow as the engine speed is required to increase or decrease. The rotational speed is displayed digitally on the GSU. The method of measuring the engine rotational speed has proven to be accurate and reliable over the past 10 years (Baird, 2011).

f) Fuel Consumption Measurement

The engine fuel consumption was measured by hanging a *5* liter fuel container vertically from an *HBM U2A 50 kg* load cell. The load cell is connected to the *HBM Spider8* data logger that displays the fuel consumption in *kg over time* (*kg/s*) on the PC. The HBM U2A load cell has a sensitivity of ± 0.2% for tensile loads.

4.2.3 Experimental Procedure

Experiments were performed to measure the gas turbine mass flow, thrust, exhaust gas temperature, static pressure distribution inside the compressor and fuel consumption. The different diffuser configurations were assembled in the gas turbine and evaluated.

The gas turbine is controlled by a BMT Ground Support Unit, (GSU). The GSU controls the engine speed by adjusting a certain percentage of the fuel pump voltage. The GSU digitally display the impeller rotational speed, exhaust gas temperature, (EGT), and the fuel pump voltage.

The experimental procedure for each test case is identical and is briefly discussed in Appendix E.

4.2.4 Data Processing and Test Uncertainty

All engine characteristics are tabulated and plotted using Excel. To compare the performance of each diffuser, the engine thrust and compressor static pressures and temperatures are plotted against the mass flow rate and engine rotational speed.

The accuracy of the results are determined by making use of an uncertainty analysis. Test uncertainty is calculated to determine the accuracy or quality of the test and the bounds of the measured values. The static pressure measurements are measured with a direct feedback into the HBM Spider 8 data logger and are independent of other variables and therefore the results will have an uncertainty of ± 0.3%, as stated by HBM, for their P8AP pressure transducers. Since no major pulsations occurred during testing, a time average of the measured data could be used. Similarly, the engine thrust, fuel consumption and temperature measurements are also measured with a direct feedback and will have an uncertainty of ± 0.25%, ± 0.2%, ± 2.2˚C respectively. However, the mass flow rate depends on the relative effect of systematic errors in the measured quantities. Similarly the efficiency calculations are also dependent on both temperature and pressure measurements. The mass flow and efficiency results will therefore have an uncertainty of 1.2% and 0.6% respectively.

4.2.5 Results

The engine test facility is not designed to adjust the engine mass flow rate at a specific constant speed to obtain the operating range of the compressor at that speed. Only a single working point is obtained at a specific speed that represent the compressor performance curve, i.e. the actual working line of the compressor is obtained as the engine spools up from idle to maximum speed.

a) Repeatability

Good repeatability of the experimental results is essential for the test facility. Repeatability is crucial for creating confidence in the test facility results and plays an important role in the validation of the 1-D and 3-D computer simulations. The test facility delivered repeatable experimental results as seen in Figure 4.8. Figure 4.8 shows a comparison of the total-to-static pressure ratio results at the diffuser outlet between two consecutive runs on the test bench.

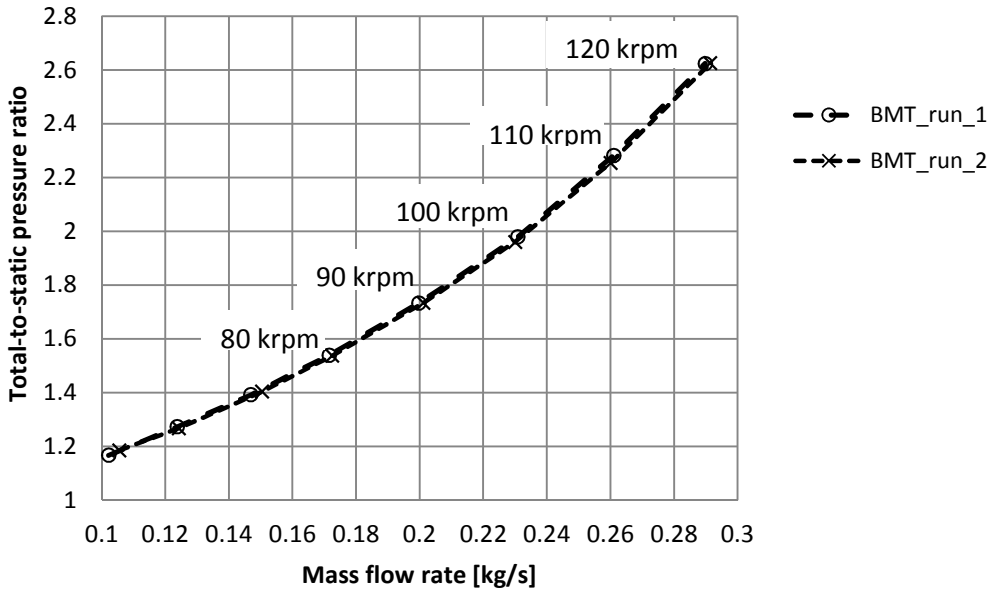

Figure 4.8: Repeatable results between consecutive runs

5 VERIFICATION AND VALIDATION OF COMPAERO AND FINE™/TURBO

5.1 Introduction

This chapter involves the verification and validation of the 1-D (CompAero) and 3-D (Fine™/Turbo) analyses using the experimentally obtained BMT 120 KS results. The validation is presented and summarized by means of various comparison graphs, tables and maps. Note that for the experimental test data only a compressor performance curve, i.e. the compressor's actual working line, was obtained as the engine spools up from idle to maximum speed. The experimental test facility is not designed to throttle the mass flow at a specific constant speed. In other words the compressor operating map showing various constant speed lines is not obtained from the experimental tests, only a single working point is obtained at a specific rotational speed.

Since the 1-D modelling on the mean stream surface through the compressor does not provide solutions for distributions from hub to shroud, the main focus throughout the validation process was based on performance predictions, i.e. pressure ratios, efficiencies etc. using time and area averaged values.

The compressor performance curve obtained from the experimental test facility is used to verify and validate the 1-D and 3-D numerical solutions, i.e. the radial diffuser discharge values are used. Appendix E provides tables for the experimental data obtained from the experiments.

5.2 Validation of CompAero

CompAero evaluates the operating range from choke to stall of a specific constant speed line in CENCOM. The compressor is therefore simulated in CENCOM for a number of constant speeds and plotted on a compressor map (see Figure 5.1). The simulated speeds are as follows: 80, 90, 100, 110 and 120 krpm. The experimental compressor working line is plotted on the same compressor map and the experimental data point at each specific speed is compared to the numerically obtained speed line. CompAero computes the operating range at 8 points between choke and stall for a specific constant speed line. One of these points is assigned to the same mass flow rate as the experimentally measured value. The performance predictions by CompAero are evaluated and compared to the experimentally obtained results at this specific point to determine the accuracy of the 1-D mean stream surface analysis by Aungier (2000) (see Figure 5.2).

The vaned diffuser performance analysis by CompAero is an iterative process that continues until the discharge meridional velocity component ($C_{m,4}$) has converged in VDDESIGN. The performance prediction for Diffuser 1 (the original diffuser is referred to as Diffuser 1) converged after 8 iterations.

Table 5.1 indicates the percentage difference between the experimental and 1-D data for each specific rotational speed and mass flow rate at the radial diffuser discharge. The largest deviation between results was obtained for the total-to-total efficiency (η_{TT}) at 80 krpm and 0.171 kg/s with a deviation of 4.9%. When considering the percentage deviation between the simulations and experimental results for the total and static pressure measurements at 80 krpm it is seen to be well below 5% for both cases and therefore considered acceptable. A deviation of 1.5% for the static pressure at 80 krpm proves the validity of the 1-D results, since the static pressure is the actual measured value at the diffuser discharge. The total pressure and total-to-total efficiency are calculated from the measured data by using isentropic relationships as shown in Equation B.6. Despite the deviation of 4.92% it was decided that CompAero satisfactorily predicts the flow in the compressor and was therefore used in the new diffuser design procedure as described in Chapter 6. Also note that the new diffuser designs will be designed at a rotational speed of 120 krpm and a mass flow rate of 0.3 kg/s. When considering the differences obtained at 120 krpm the results prove to be more than satisfactory.

Table 5.1: Radial diffuser discharge conditions for experimental and 1-D data

$\dot{m}$ [kg/s]	N [krpm]	$p_{t,4}$ [kPa]		Dev [%]	p_4 [kPa]		Dev [%]	η_{TT} [%]		Dev [%]
		Exp	1-D		Exp	1-D		Exp	1-D	
0.171	80	180.8	176.4	2.4	153.9	156.2	1.5	82.1	86.3	4.9
0.199	90	203.6	202.0	0.8	173.3	176.4	1.8	82.5	86.1	4.1
0.230	100	232.5	231.9	0.3	197.9	200.1	1.1	83.9	85.3	1.6
0.260	110	268.1	267.6	0.2	228.2	230.3	0.9	83.1	84.2	1.4
0.288	120	308.3	312.0	1.2	262.4	269.9	2.8	84.5	83.4	1.3

5.3 Verification of FINE™/Turbo

The CFD verification process involves the quantification of errors. Apart from computer coding and user errors in FINE™/Turbo additional errors need to be investigated for CFD verification. These include roundoff errors, iterative convergence errors and discretization errors (Versteeg et al, 2007).

The *roundoff* error is assessed by comparing computed results for the same mesh by using different levels of machine accuracy. This was achieved by comparing single and double precision results in FINE™/Turbo. It was determined that the solutions are more than acceptable by setting the solver to single precision. A difference of $33.6 \cdot 10^{-6}$ was calculated between the mass flow solutions of the single and double precision results. The double precision results required much more memory and computational time. It was therefore decided to use single precision for the simulations.

The *iterative convergence* error is quantified by investigating the effects of systematic variations of the truncation criteria for all residuals on selected quantities of interest, e.g. mass flow rate. The inlet and outlet mass flow rates are compared for each simulation to determine the confidence of a fully converged solution. Errors between the inlet and outlet mass flow rates were less than 0.4% for each simulation at convergence.

The *discretization error* is quantified by refining the mesh systematically. The method used is described below:

The discretization error, E_U, of a steady flow problem can be written in terms of the difference between a selected target quantity, U, i.e. mass flow, as a function of a reference size h of the control volumes inside the mesh (Versteeg et al, 2007). For two meshes with a refinement ratio $r = h_2/h_1$ and solutions U_1 and U_2, the discretization error can be written in terms of the difference between the two solutions:

$$E_{U,1} = \frac{U_2 - U_1}{1 - r^p} \tag{5.1}$$

$$E_{U,2} = r^p \frac{U_2 - U_1}{1 - r^p} \tag{5.2}$$

Where $E_{U,1}$ is the course grid solution error, $E_{U,2}$ the finer grid solution error and p is the order of the numerical scheme, i.e. $p = 1,2,3$ etc.

Roache (1997) proposed a so-called grid convergence indicator (GCI) to quantify the numerical error in a CFD solution (Versteeg et al, 2007):

$$GCI_U = F_s E_U \tag{5.3}$$

where F_s is the safety factor.

Versteeg et al. (2007) recommends that the discretization error formula (Equations 5.1 and 5.2) should be evaluated using Roache's (1997) proposed equation (Equation 5.4) for the order of the truncation rate decay ($\tilde{p}$) for three successively refined meshes, in conjunction with a reduced safety factor, $F_s = 1.25$, for high-quality studies using two or more levels of refinement.

$$\tilde{p} = ln\left(\frac{U_3 - U_2}{U_2 - U_1}\right) / \ln(r) \tag{5.4}$$

$U_2 - U_1$ is the difference between the coarse and medium grid solutions and $U_3 - U_2$ is the difference between the fine and medium grid solutions.

The discretization errors for the BMT 120 KS centrifugal compressor meshes are indicated in Table 5.2.

It was concluded from the results obtained for the roundoff error, iterative convergence error and discretization errors in Table 5.2 that FINE™/Turbo adhere well to the CFD quantification criteria.

Table 5.2: Discretization errors in CFD

Parameter	Value
$\tilde{p}$	1.263
$E_{U,1}$	$3.68 \cdot 10^{-3}$
$E_{U,2}$	$6.39 \cdot 10^{-4}$
$GCI_{U,1}$	$4.6 \cdot 10^{-3}$
$GCI_{U,2}$	$7.99 \cdot 10^{-4}$

5.4 Validation of FINE™/Turbo

Similar to the validation process of CompAero, the CFD results obtained in FINE™/Turbo are also validated against the experimental BMT 120 compressor test data. The operating range from choke to stall is firstly determined for each specific speed, i.e. 80, 90, 100, 110, 120 krpm, whereafter the corresponding experimentally measured mass flow rate is determined in FINE™/Turbo for comparison. Since the outlet boundary in FINE™/Turbo is static pressure imposed, a number of trial-and-error simulations are run until the corresponding experimental mass flow rate is achieved.

CFView™ is used to display the solved flow domain results. Cutting planes are inserted in the compressor model in CFView™ to compute the values at the same location as that used in the experimental setup. A weighted integral averaged value is determined for each parameter over the cutting plane for the corresponding location to be used for validation. The cutting plane allows the user to determine results at any point over the flow domain and therefore made it possible to determine the flow criteria in the diffuser throat. The results and percentage deviations between the experimental and CFD solutions at the radial diffuser discharge are indicated in Table 5.2. The compressor working line is also indicated in Figure 5.2.

The largest deviation is obtained for the total-to-total efficiency (η_{TT}) at a rotational speed of 80 krpm and mass flow rate of 0.171 kg/s, as seen in Table 5.3. However, the deviation for both the total and static pressure measurements at 80 krpm are well below 5%, and thus considered acceptable.

5.5 Modelling Results and Discussion

The total-to-total and total-to-static pressure ratio performance curves or working lines for the 1-D and CFD computations fit the experimental working line well, as seen in Figures 5.2 and 5.3. The 1-D total-to-static pressure ratio seem to deviate slightly from the experimental data as the rotational speed is increased, yet a deviation of 2.78% at 120 krpm is still tolerable. The total-to-total efficiency for the 1-D and CFD computations follow a similar trend as seen in Figure 5.3, whereas

the experimental data seem to predict otherwise. This is due to the fact that the total temperature and pressure used to determine the experimental total-to-total efficiency was computed from isentropic relationships and was not directly measured during testing.

Table 5.3: Radial diffuser discharge conditions for experimental and CFD data

$\dot{m}$ [kg/s]	N [krpm]	$p_{t,4}$		Dev [%]	p_4 [kPa]		Dev [%]	η_{TT} [%]		Dev [%]
		Exp	CFD		Exp	CFD		Exp	CFD	
0.171	80	180.8	182.5	0.9	153.9	158.9	3.2	82.1	86.6	5.2
0.199	90	203.6	209.0	2.6	173.3	177.6	2.4	82.5	85.6	3.6
0.230	100	232.5	239.6	3.0	197.9	200.1	1.1	83.9	84.5	0.7
0.260	110	268.1	278.9	3.9	228.2	225.4	1.2	83.1	82.8	0.3
0.288	120	308.3	314.8	2.1	262.4	260.0	0.9	84.5	80.9	4.5

The operating range for each constant speed line in the 1-D and CFD solutions seem to predict similar results near the actual operating point. However, as the rotational speed increases the operating point predictions deviate slightly as seen in Figure 5.1 and 5.2. In addition, the stall and choke margins seem to differ for the 1-D and CFD operating ranges. This is assigned to the fact that Aungier's (2000) stall and choke criteria for 1-D flow reduces the operating range to ensure stable operation.

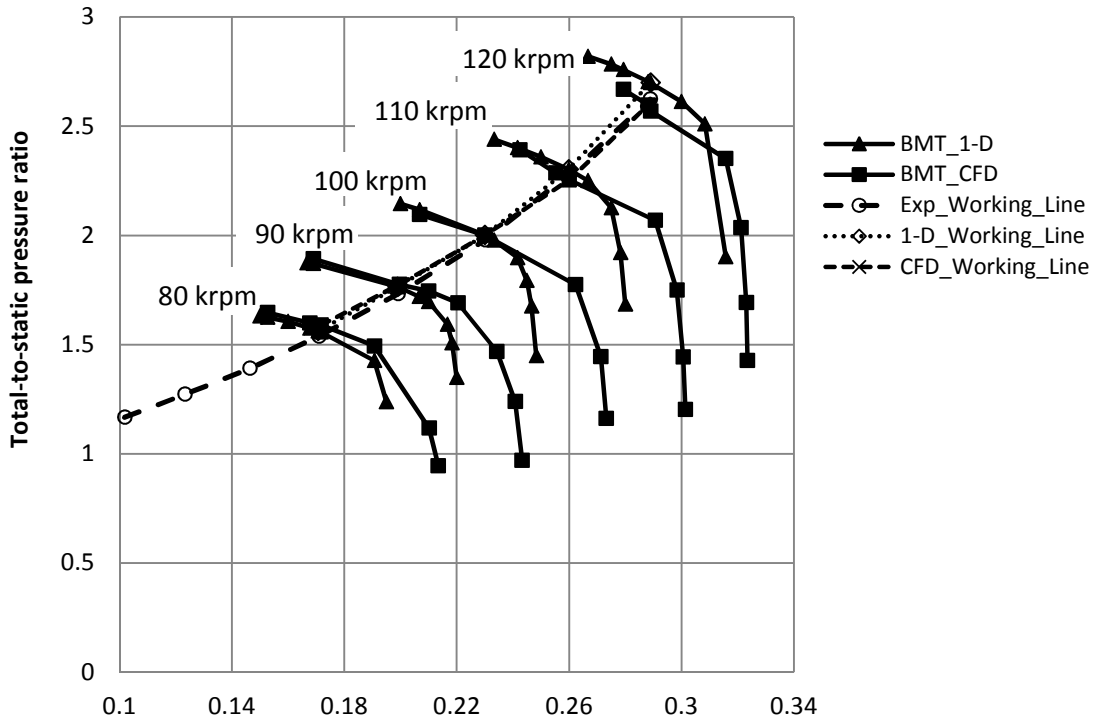

Figure 5.1: BMT 120 KS total-to-static performance map

Evaluating Aungier's impeller blade stall criteria (Equation 5.6), it indicates stable operation for the 1-D working line, with a maximum diffusion factor (D_{eq}) of 2.05 at 0.267 kg/s and 120 krpm, indicating stall. Aungier (2000) states that impeller stall can be expected when $D_{eq} > 2$, Equation 5.5, where W_{max} is the maximum relative velocity and W_2 is the relatve velocity at the impeller tip.

$$D_{eq} = \frac{W_{max}}{W_2} \tag{5.5}$$

$$D_{eq,stall} > 2 \tag{5.6}$$

The diffusion factor at the operating point of 0.288 kg/s and 120 krpm is 1.9. Following Aungier's (2000) diffuser stall criterion (Equations 6.17 to 6.19) it was observed that diffuser stall occurred at a mass flow rate of 0.244 kg/s. Aungier (2000) states that diffuser choke is observed when the aerodynamic throat area is smaller than the required area for a sonic velocity at a specific mass flow rate, i.e. $C_r A_{th} \leq A^*$. A^* is determined using Equations B.13 to B.16. The diffuser is found to choke at a mass flow of 0.316 kg/s at 120 krpm.

An indication to the onset of stall in the CFD simulations is when the inlet and outlet mass flow solutions oscillate with large amplitudes and eventually diverge. Choke is determined when the mass flow rate remains constant for a reduced static pressure imposed computation, indicated when the constant speed lines become vertical in Figure 5.1.

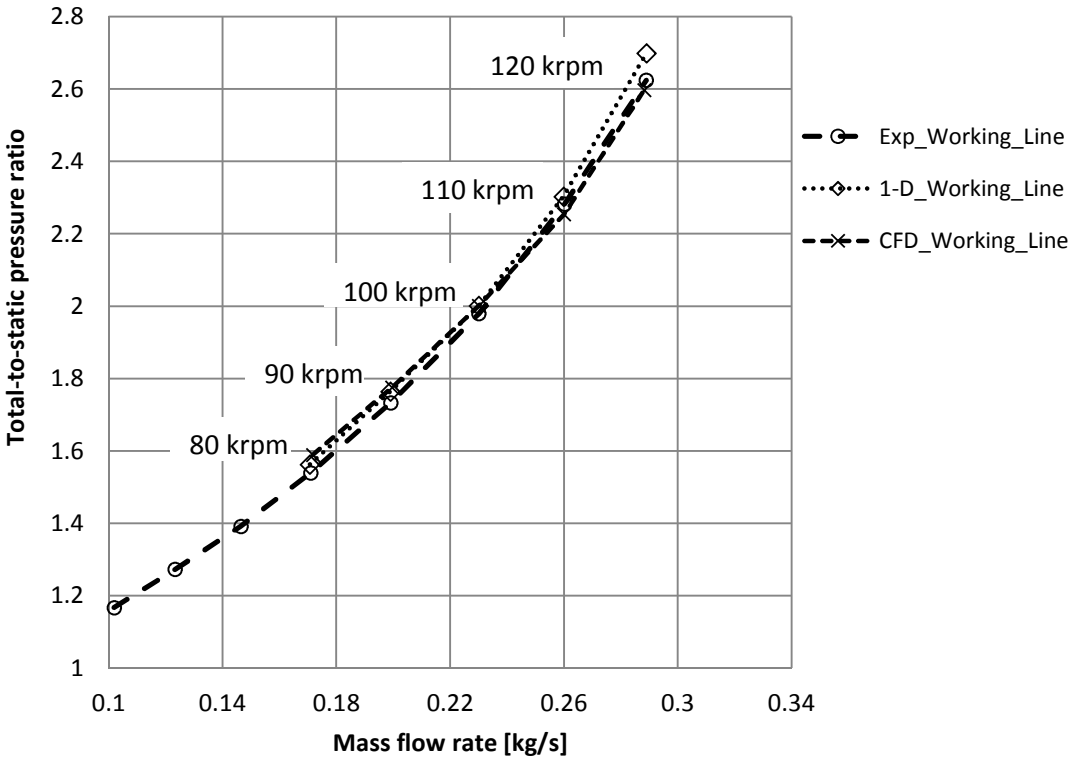

Figure 5.2: BMT 120 KS total-to-static working line

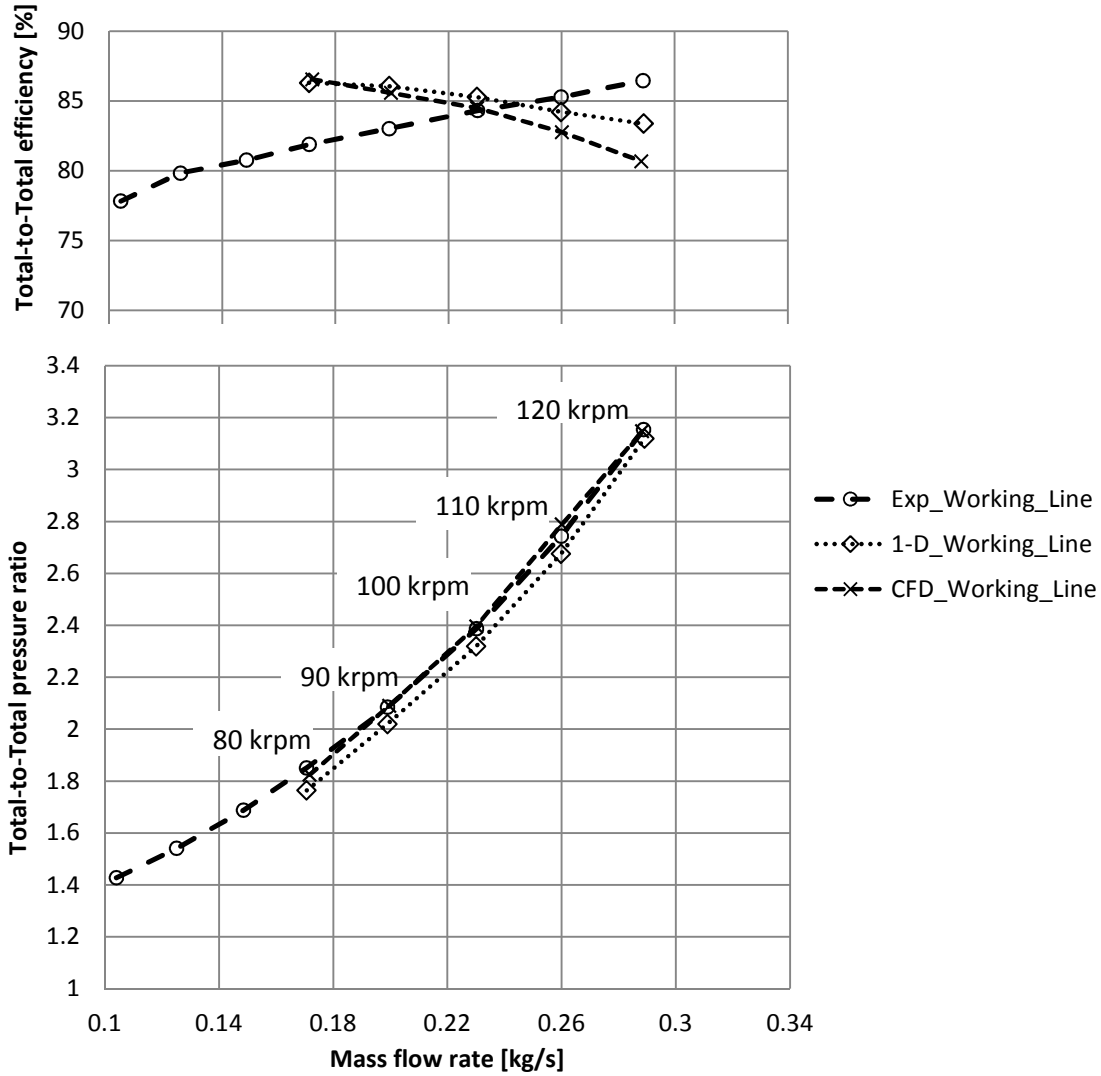

Figure 5.3: BMT 120 KS Total-to-Total performance curve

6 VANED DIFFUSER DESIGN

6.1 Introduction

After the in-depth literature study in Chapter 2, it was realized that a number of tradeoffs need to be addressed when designing a diffuser for a centrifugal compressor, for example mass flow rate vs pressure ratio, surge vs choke, operating range vs optimum design point etc. It was therefore decided to design three radial diffusers, each with different vane geometries and tradeoffs. The aim for this thesis is to design a diffuser that achieves a higher pressure recovery, with a minimum loss in efficiency, by only redesigning the diffuser vane geometry, constraining the flow passages to the original BMT 120 KS compressor hub and shroud contours.

The four diffuser configurations discussed in this chapter are referred to as Diffuser 1, 2, 3 and 4. Diffuser 1 is the original BMT 120 KS diffuser. The designs and reasoning of Diffuser's 2 to 4 will be discussed in the following chapter by clearly indicating which diffuser is being discussed.

6.2 Diffuser Design Procedure

The experimental test data recorded for the original BMT 120 KS is used as reference work for the 1-D and CFD validation and performance comparison. After extensive validation of CompAero and FINE™/Turbo, it was decided to base the preliminary diffuser design on the 1-D approach by Aungier (2000) using CompAero's CENCOM and VDDESIGN programs, due to its rapid computational time for compressor performance predictions. Aungier's (2000) preliminary design strategy in CompAero is based on reference design conditions that are consistent with good design practice and achievable performance objectives (Aungier, 2000). Once a satisfactory diffuser design is obtained with VDDESIGN, the vane geometry is exported to SolidWorks to create a 3-D CAD model. The 3-D model is then exported to Autogrid5™ by means of a **.geomTurbo* file as explained in Section 3.3 to perform the CFD computations. If the CFD results prove to be adequate the full diffuser assembly is created in SolidWorks and the parts are machined for experimental testing.

6.3 Diffuser Constraints

The overall dimensions of the gas turbine need to be kept to an absolute minimum due to its application in the aeronautical field. The diffuser geometry needs to adhere to the constrained radial space between the impeller tip and the engine housing. The radial distance between the impeller tip (r_2 = 35 mm) and engine housing (r_5 = 53.3 mm) is 18.3 mm, (see Figure 6.1). It was decided to

leave the hub and shroud contours that define the flow passage as is and only redesign the diffuser vane geometry.

The hub and shroud contours are parallel over the vaneless space, i.e. between the impeller tip and diffuser inlet, with a passage depth (b) of 6 mm. The shroud contour over the radial diffuser extends radially outwards with a constant axial (z) coordinate, whereas the hub contour varies linearly with the radial length such that it gradually increases the flow passage at a diverging angle of θ = 6.3˚, see Figure 6.1.

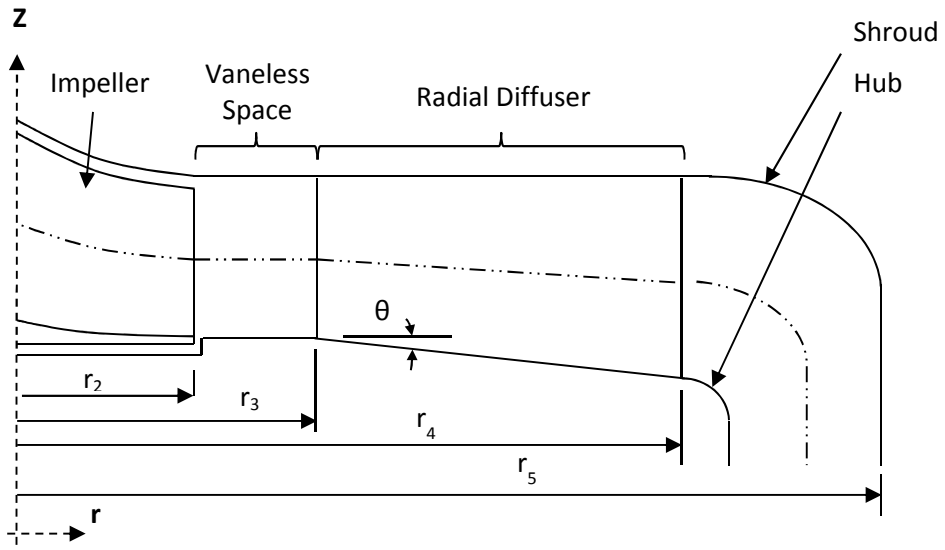

Figure 6.1: Compressor geometry in the r-Z plane

The original BMT 120 KS engine (with Diffuser 1) delivered a thrust of 107.3 N at a rotational speed of 120 krpm. The compressor developed a total-to-static pressure ratio of 2.62 at a mass flow rate of 0.288 kg/s. The design point for the compressor is taken as 0.3 kg/s at a rotational speed of 120 krpm to maximize the pressure recovery.

6.4 Diffuser Configurations

The new diffuser designs are predominantly based on theory by Aungier (2000), since his 1-D mean stream surface program (CompAero) is used. However other criteria not used by Aungier are also considered in the design process and mentioned where necessary. The four diffuser configurations are briefly discussed in this section to supply the reader with an overall idea of each diffuser before the in-depth design discussion follows. Note that any further geometrical information regarding the radial diffusers that are not included in this chapter is provided in Table E.2.

6.4.1 Diffuser 1

The original BMT 120 KS compressor makes use of a straight thick-vaned radial diffuser as seen in Figure 6.2. The diffuser throat is also indicated in the figure. It has 15 radial vanes and 42 axial blades. The walls of the pressure and suction surfaces of the radial vanes are symmetric; and are joined with a straight and sharp leading edge at the diffuser inlet, at a radius (r_3) of 37 mm. The diffuser trailing edge forms a circular arc that has the same radius as the diffuser discharge (r_4 = 46.5 mm). The diffuser flow passages have a rectangular cross sectional area and the width (w) of the passages diverge linearly outwards at a combined angle of 9˚, i.e. $2\theta = 9°$.

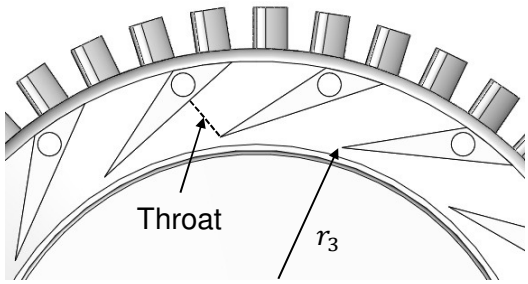

Figure 6.2: Diffuser 1 vane geometry, (original BMT 120 KS diffuser)

6.4.2 Diffuser 2

Diffuser 2 is similar in concept to that of an airfoil type diffuser as seen in Figure 6.3. It was decided to design a marginally-curved airfoil vane to determine whether it performs better than the conventional thick vaned diffusers, as claimed by Aungier (2000). Considering the diffuser constraints described in Section 6.3 and the actual machining constraints, the airfoil-type vane was designed using CompAero to deliver a maximum pressure recovery and resulted in a radial diffuser with 30 vanes. The flow passages between the blades also have rectangular cross sections. It was decided to decrease the number of axial blades from 42 to 30, such that each radial vane has a matching axial blade. By reducing the number of axial blades the blade solidity decreases and the axial flow passage increases, resulting in additional diffusion to take place, possibly at the expense of a reduced swirl component. Again a straight and sharp leading edge is used at the diffuser inlet radius (r_3) of 38 mm. The trailing edge is also sharp at a radius (r_4) of 48 mm. Note that the radial vane trailing edge of Diffuser 1 has a radius of 46.5 mm. The slightly increased radial length of the flow passages should also contribute to the diffusion process and decrease the swirl component (Runstadler et al., 1973). The 'bulb', indicated by (1) in Figure 6.3, exists at the trailing edge of 6 of the 30 airfoil vanes. This is used to fix and assemble the compressor components in the BMT 120 KS engine.

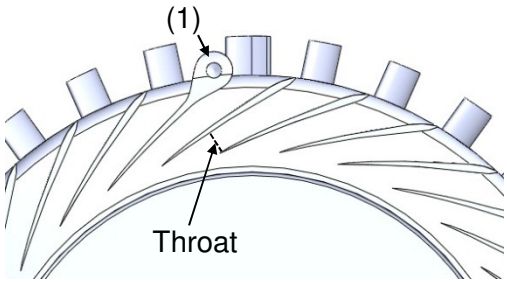

Figure 6.3: Diffuser 2 vane geometry, (airfoil type design)

6.4.3 Diffuser 3

The main aim of Diffuser 3 was to use CompAero to design a diffuser capable of maximum pressure recovery at the design point, despite a poor blade loading parameter or effective divergence angle. This led to the vane geometry as indicated in Figure 6.4. This design also has 30 radial vanes and 30 axial blades. Again a rectangular cross section defines the flow passage between consecutive vanes. The vane leading edge is straight and rounded at the diffuser inlet, ($r_3 = 38\,mm$). Similar to Diffuser 2, the trailing edge is extended to a radius of 48 mm. The major difference in this diffuser concept is its increased outlet blade angle (β_4). The vanes now redirect the flow into the radial direction that contributes to the diffusion process by reducing the large swirl component and the absolute velocity through the diffuser.

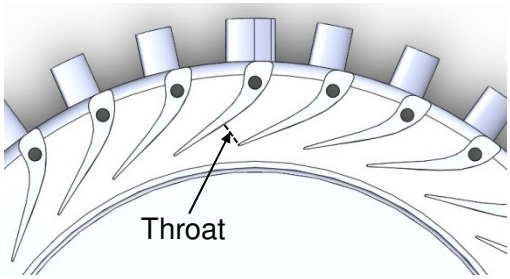

Figure 6.4: Diffuser 3 vane geometry

6.4.4 Diffuser 4

The design process of Diffuser 4 was executed manually by modifying certain vane parameters as suggested by various authors (see Chapter 2) in conjunction with CFD flow predictions from hub to shroud. The main aim of Diffuser 4 is to design a diffuser vane that matches the distribution of flow angles from hub to shroud exiting the impeller better by varying the vane leading edge angles. The CFD analysis involved various visual and numerical investigations that were executed on the original BMT 120 KS compressor as well as on the BMT 120 KS impeller with no diffuser (vaneless). The vaneless model was executed to determine the streamline and flow predictions over the radial passage, in order to design a diffuser that properly

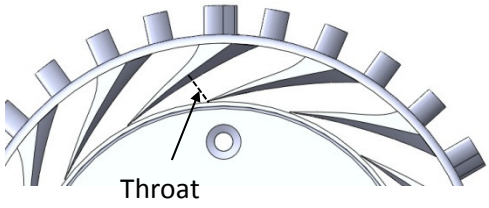

Figure 6.5: Diffuser 4 vane geomtry

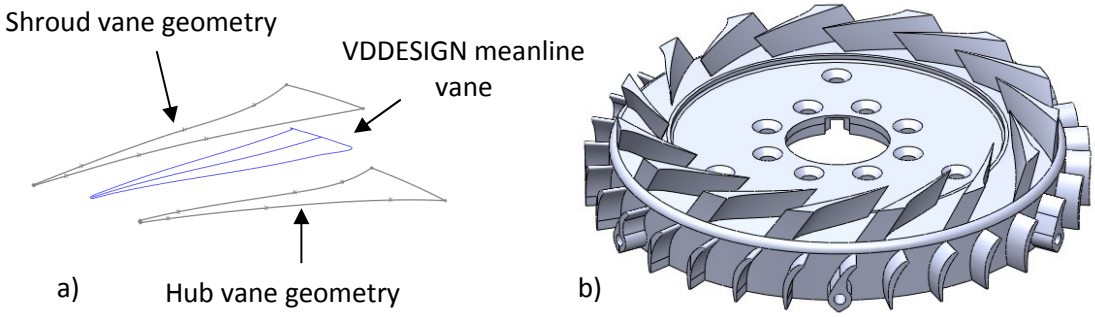

Figure 6.6: Diffuser 4 a) vane geometry, b) meridional view

matches the streamlines from hub to shroud. The vane leading edge is sharp and leans forward from hub to shroud as seen in Figure 6.6. In addition the 15 radial vanes are curved towards the trailing edge to accommodate better diffusion with minimum boundary layer growth. Diffuser 4 also has 30 axial blades.

6.5 Diffuser Enhancements, Analysis and Criteria

The function of a diffuser is to recover and convert the maximum possible kinetic energy, generated by the impeller, to static pressure. Throughout the literature study it was noted that a certain standard trend is followed when designing centrifugal compressors, but few components in the design involve as much difference in opinion from designers as do the vaned diffuser. Lately the use of Computational Fluid Dynamics (CFD) has brought about reasonable clarity with regards to the flow patterns in the compressor. This section discusses the design procedure and reasoning of each diffuser.

6.5.1 Diffuser Vaneless Space

The main function of the vaneless space between the impeller tip and diffuser inlet is to reduce the high Mach numbers that exit the impeller tip when the engine is running at maximum speed. The Mach number at the impeller tip and diffuser inlet is calculated to be 0.83 and 0.77 respectively at a rotational speed of 120 krpm for the original BMT 120 KS turbine (with Diffuser 1).

Since the hub and shroud contours remain fixed only the radial length of the vaneless space is adjusted for the new designs. Care is taken not to design the vaneless space too large, since this may result in excessive boundary layer growth that negatively contribute to the diffuser throat blockage downstream and reduce the surge margin (Bennet et al., 2000). As a general guideline to determine the vaned diffuser inlet (r_3) the following radius ratio criteria is recommended by Aungier (2000)

$$1.06 \leq \frac{r_3}{r_2} \leq 1.12 \qquad 6.1$$

Diffuser 1 has a vaneless space radial length of 2 mm, i.e. $r_3/r_2 = 1.057$. Based on Equation 6.1, the radial length of the vaneless space should vary between 2.1 mm and 4.2 mm for the respective KKK K27.2 impeller ($r_2 = 35\,mm$). According to Aungier (2000), the radius ratio should be as close to the lower limit as possible if the Mach numbers allow it. Similar radius ratio criterion is also recommended by Ziegeler (2003) and Shum (2000). It was therefore decided to design Diffusers 2 and 3 with a radius ratio of 1.086, i.e. $r_3 = 38\,mm$. This reduces the Mach number at the diffuser inlet to 0.75.

The vaneless space in Diffuser 4 varies from hub to shroud creating a vaneless space with an additional 'semi-vaneless space'. The vane leading edge at the shroud is designed with a radius (r_3) of 36 mm, whereas the vane leading edge at the hub is placed at a radius (r_3) of 38 mm, resulting in a mean vane leading edge radius (r_3) of 37 mm. The mean stream surface calculations in VDDESIGN

are executed with a vane leading edge radius of 37 mm resulting in a radius ratio of 1.057. The additional 'semi-vaneless space' adds to the reduction of large Mach numbers that exit the impeller tip.

The vaneless space performance predictions by CompAero at the operating point ($\dot{m} = 0.288\ kg/s$) and the design point ($\dot{m} = 0.3\ kg/s$), are indicated in Table 6.1. From Table 6.1 it is seen that no major gains are predicted over the vaneless passage for the increased radius ratio. However, the static pressure increases for Diffusers 2 and 3 with a favorable decrease in Mach number. Diffuser 4 proves to be slightly more efficient than Diffusers 2 and 3, yet no major improvements are seen over the vaneless space when compared to Diffuser 1.

Table 6.1: Vaneless passage performance predictions by CENCOM

Diffuser		**1**	**2**		**3**		**4**	
r_3/r_2	[-]	1.057	1.086		1.086		1.057	
$\dot{m}$	[kg/s]	0.288	0.288	0.300	0.288	0.300	0.288	0.300
$p_{t,3}$	[kPa]	328.55	325.13	320.62	325.13	320.62	328.55	323.72
p_3	[kPa]	220.54	223.67	221.06	223.67	221.06	220.54	217.81
Ma_3	[-]	0.77	0.76	0.75	0.76	0.75	0.78	0.77
$Total\ LC$	[-]	0.041	0.069	0.064	0.069	0.064	0.041	0.038
$Static\ C_p$	[-]	0.075	0.101	0.105	0.101	0.105	0.075	0.078
$\eta_{adiabatic}$	[%]	84.9	84.0	84.0	84.0	84.0	84.9	84.8
$\eta_{polytropic}$	[%]	87.2	86.4	86.3	86.4	86.3	87.2	87.1

6.5.2 Vaned Diffuser

Vaned diffusers are the most effective way to decelerate trans- or supersonic flow exiting impellers and achieve high pressure recovery over a relatively short distance, as opposed to a vaneless diffuser. There is therefore no question that a vaned diffuser needs to be used for the BMT 120 KS turbine. The various geometric and aerodynamic design parameters are discussed in this section.

a) Leading edge geometry and throat area

The diffuser leading edge geometry up to the diffuser throat is accepted as being the most critical feature in any aerodynamic diffuser design and crucial to the performance of a centrifugal compressor. The air leaving the impeller is presented in a warped or distorted fashion to the vaneless space and moves in a logarithmic spiral path before entering the diffuser. The first step in the diffuser design process is to establish the location of the vane leading edge (r_3) and inlet blade angle (β_3). The primary constraint at the vane inlet is to match the vane leading edge geometry to the impeller tip flow.

Good performance and a wide stable operating range of the vaned diffuser require low flow angles (α_2 and α_3). Diffusion and passage curvature losses are dominant factors at high flow coefficients (φ) which in turn require higher flow angles (α), but according to Aungier (2000) vaned diffusers cease to be effective at the higher flow coefficients. This adds to the importance of the vaned diffuser design, since relatively high flow coefficients exist at the impeller tip for a rotational speed of 120 krpm. The flow coefficient at the impeller tip (Equation 6.2) and vane inlet flow angle of each diffuser is included in Table 6.2.

$$\phi_2 = \frac{\dot{m}}{\rho_{t,0}\pi r_2^2 U_2} \qquad 5.2$$

Table 6.2: Flow data predicted by VDDESIGN

Diffuser	$\dot{m}$ $[kg/s]$	ϕ_2 [-]	α_3 [˚]	β_3 [˚]	i_3 [˚]
1	0.288	0.302	19.9˚	18.5˚	-1.4
2	0.300	0.318	21.8˚	21.5˚	-0.3˚
3	0.300	0.318	21.7˚	23.6˚	1.9˚
4	0.300	0.318	21.2˚	22.0˚	0.8˚

The leading edge geometry is designed to match the flow angles that exit the impeller tip at the design point. Diffuser 1 has a straight and sharp leading edge with an inlet vane angle (β_3) of 18.5˚ at a radius of 37 mm. After analyzing the flow on the mean stream surface with CompAero and FINE™/Turbo it was found that the flow angle does not perfectly match the blade inlet angle of Diffuser 1 resulting in boundary layer growth and a decreased flow area, as seen in Figure 6.7 and 6.8. According to Aungier (2000) the vaned diffuser incidence angle (i_3) should usually be around -1, i.e. $i_3 = \beta_3 - \alpha_3$. Flow separation occurs at the leading edge of Diffuser 1, resulting in an increased boundary layer thickness across the diffuser flow passages that reduce the effective throat area. Diffuser 1 has an incidence angle of -0.95˚ with an incidence loss coefficient of 0.0409. Vaned diffusers will tend to show a wider stable operating range if they are designed with low inlet blade angles and a low number of vanes (Aungier, 2000). However if the vane inlet angle is too low the losses in the vaneless space increase and there is also a possibility that rotating diffuser stall may occur (Aungier, 2000). The blade inlet angle for Diffuser 1 proved to be too small after investigating the B2B velocity vectors from hub to shroud, resulting in excessive boundary layer growth on the vane surfaces as seen in Figure 6.7 and an increase in incidence losses (also see Figures D.15 to D.19). Figure 6.8 indicates the absolute velocity streamlines and shows the reduced flow area due to mismatched flow and vane angles.

The absolute flow angles as predicted by FINE™/Turbo are also plotted at different radii from hub to shroud between the impeller tip and diffuser vane inlet

in CFView™. One such example is shown in Figure 6.9, representing the absolute flow angles from hub to shroud at a radius of 37 mm. Figure 6.10 indicates the absolute flow angle distribution from hub to shroud for radii between 35 mm and 38 mm.

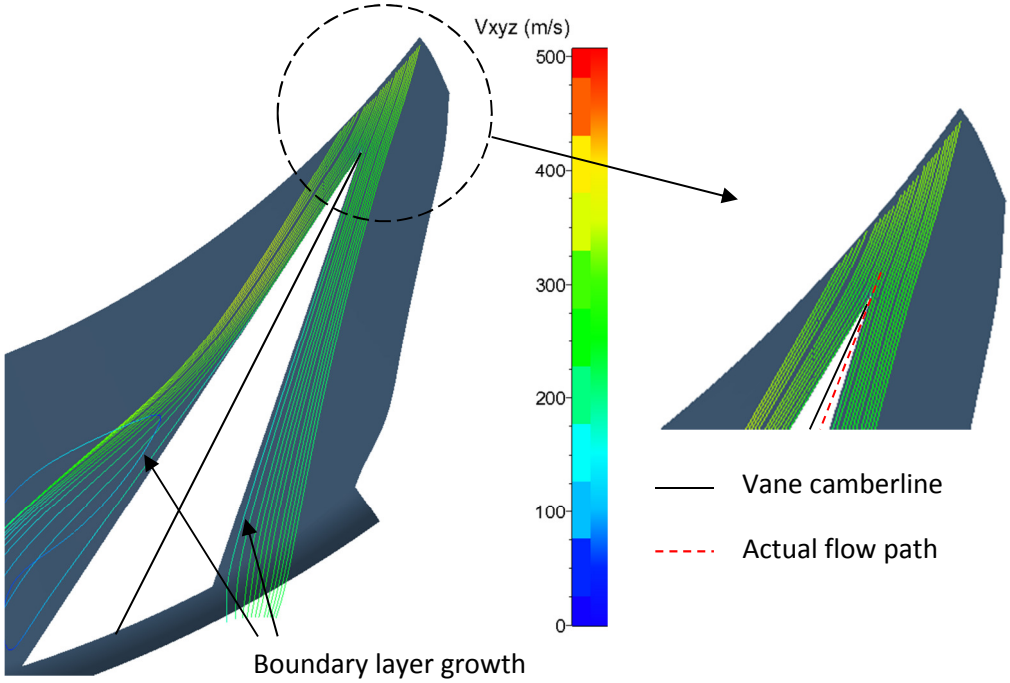

Figure 6.7: Absolute velocity flow vectors of Diffuser 1 at 50% span and the operating point

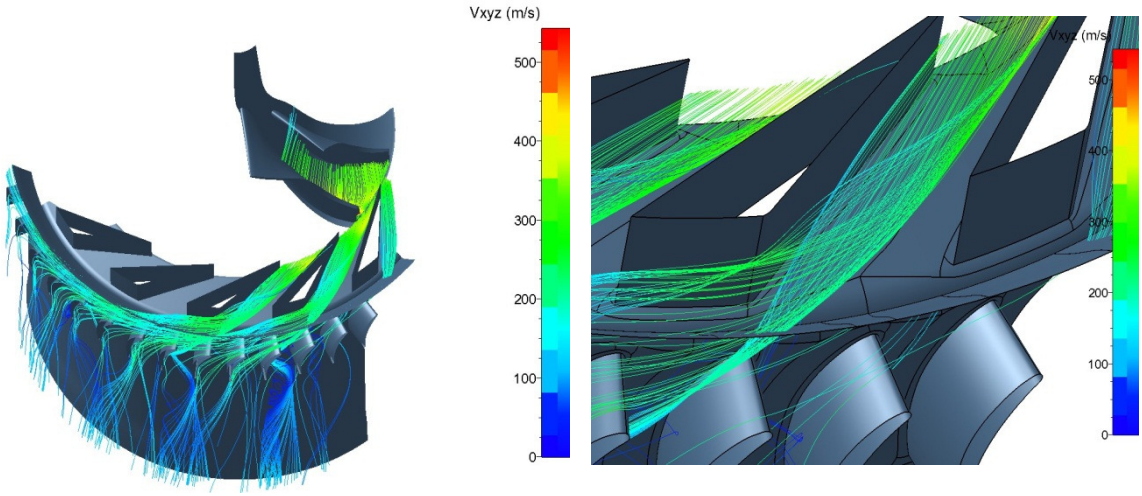

Figure 6.8: Absolute velocity flow vectors of Diffuser 1 indicating mismatched flow angles at the operating point

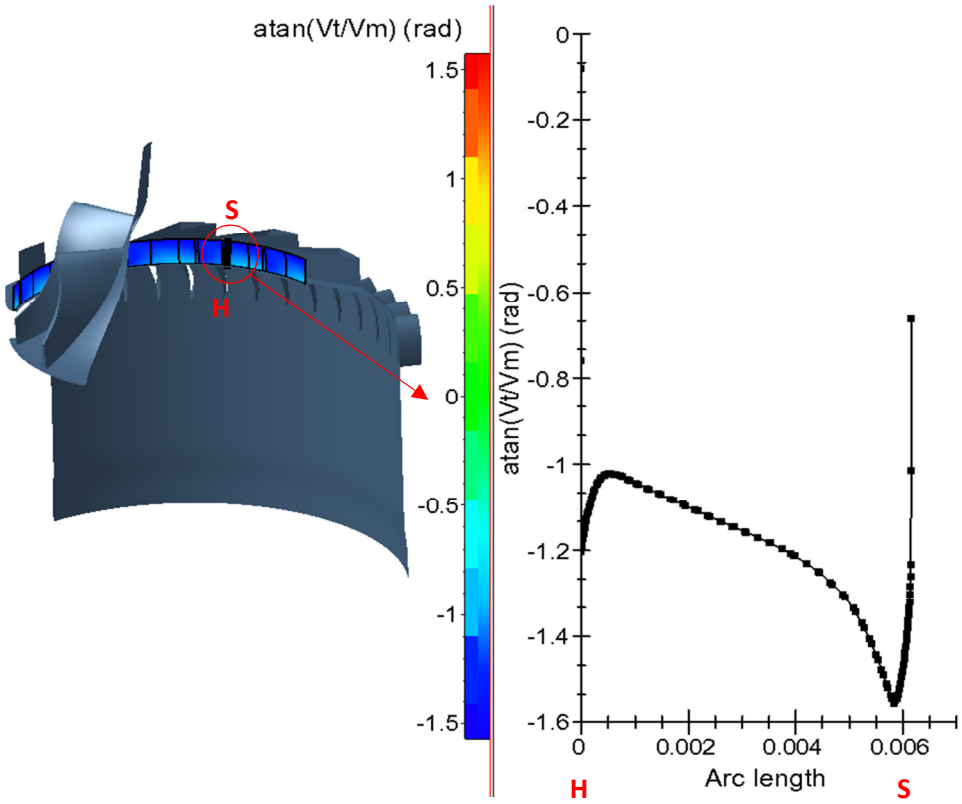

Figure 6.9: Absolute flow angles from hub to shroud at a radius of 37 mm

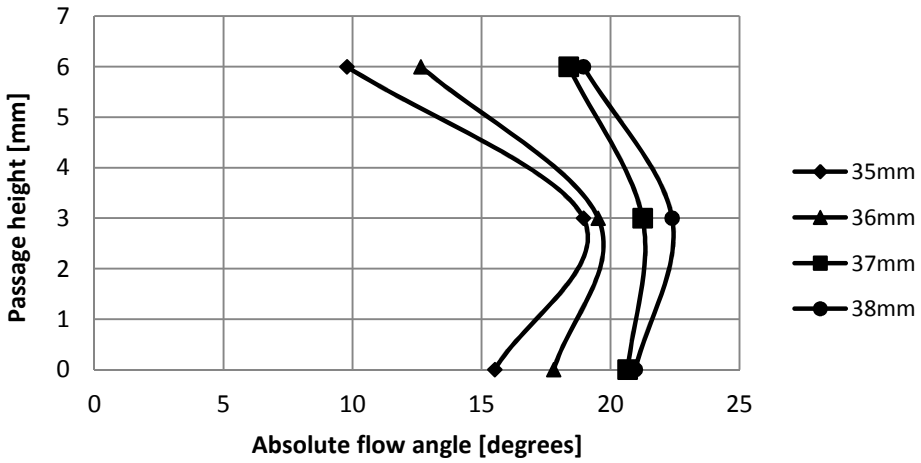

Figure 6.10: Absolute flow angle distribution for various radii over the passage height

The results in Figure 6.10 confirm the concave hub to shroud vane surface distribution as suggested by Hagishimori (2005) (see Figure 2.13).

Diffuser 2 is designed with an inlet vane angle (β_3) of 21.5˚ at a radius of 38 mm. The leading edge is straight and the point where the pressure and suction surfaces meet is sharp. The incidence angle at the inlet of Diffuser 2 is -0.27˚ with an incidence loss coefficient of 0.0205. The camberline is slightly curved as the passage extends from the vane inlet to discharge. The reason for curving the vane camberline is to better match the logarithmic spiral path that exists in the flow passage.

Diffuser 3 is designed with a further increased vane inlet angle (β_3) of 23.6˚, since this angle resulted in an increased pressure recovery coefficient predicted by VDDESIGN. However, this caused Diffuser 3 to operate in the stall region predicted by Aungier (2000) as seen in Figure F.3. The pressure and suction surfaces are joined with a small rounded leading edge at the vane inlet. Diffuser 3 has an incidence angle of 1.95˚ with an incidence loss coefficient of 0.0259. It was also noted that for a mass flow of 0.31 kg/s the incidence loss coefficient dropped to 0.0118 and the pressure recovery coefficient further increased from 0.725 to 0.734, favoring a higher mass flow rate and pressure recovery.

Diffuser 4 is designed with varying vane inlet angles to better match the flow distribution exiting the impeller tip from hub to shroud as indicated in Figures 6.7 and 6.8. From Figure 6.9 it is clear that the flow angles near the shroud are smaller than the flow angles near the hub, with an increase in flow angle in the mean streamline due to the absence of wall friction. The vane inlet angles for Diffuser 4 vary between 16.2˚ at the shroud to 23˚ at the hub. The shroud leading edge is placed at a radius of 36 mm and the hub at a radius of 38 mm due to the flow vectors predicted by FINE™/Turbo. Ideally the diffuser vanes need to be concave in shape from hub to shroud to better accommodate the flow angles exiting the impeller tip, as suggested by Hagishimori (2005). VDDESIGN predicted an incidence angle of 0.76˚ on the meanline of Diffuser 4 resulting in an incidence loss coefficient of 0.0332. It should be noted that VDDESIGN only predicts diffuser performance on the mean stream surface and therefore does not account for the curved or twisted vane geometry. The results or performance predictions by VDDESIGN for Diffuser 4 can therefore only be used as an approximation.

Another parameter critical to maximum diffusion is the throat area. The diffuser throat area is the region where Mach numbers can reach sonic flow conditions and cause the diffuser to choke. The throat size needs to be specified correctly to prevent premature choking in the compressor. The viscous area blockage in the vane throat is estimated by Aungier (2000) as a throat contraction ratio (Equation 6.3).

$$C_r = \sqrt{A_3 sin\beta_3 / A_{th}} \tag{6.3}$$

CompAero predicts diffuser choke when the effective throat area ($C_r A_{th}$) is equal to the sonic flow area (Equation 6.4).

$$A^* = \frac{\dot{m}}{\rho^* C^*} \tag{6.4}$$

Work done by Bennett et al. (2000) investigated four diffusers each having a different throat cross sectional area. The four cross sectional areas varied from 90% of the design throat area, 95% of the design throat area, the design throat area and 105% of the design throat area. From their investigations it was found that increasing the throat area by 5% appears to introduce excessive diffusion that causes the system to surge prematurely due to blockage introduced in the flow passages. There was however little variation in performance between the design throat area and the 5% reduced throat area. The poorest performance was that of the 10% reduced throat area. For their given design point the 5% undersized throat area proved to be 1% more efficient than the design throat area. Bennet et al. (2000) concluded that the diffuser should be sized very close to choke at the desired operating point, since this improves both the stage efficiency and pressure rise. The cross sectional throat area and sonic flow predictions of each diffuser are indicated in Table 6.3, as well as the incidence, choke and blockage loss coefficients (LC).

Table 6.3: Vaned diffuser design point performance predictions by VDDESIGN

Diffuser	$\dot{m}$	A_{th}	A_{th}/A^*	Incidence LC	Choke LC	Blockage LC
	$[kg/s]$	$[mm^2]$	[-]	[-]	[-]	[-]
1	0.289	581.9	1.143	0.041	0	0.024
2	0.300	586.5	1.122	0.021	0	0.034
3	0.300	576.9	1.184	0.026	0	0.050
4	0.300	591.2	1.180	0.033	0	0.038

Seen from Table 6.3 the throat area varies by ± 2% of the original diffuser flow area (Diffuser 1) and all four diffusers are designed very close to their choke limit.

The reason for the increased vane angle resulting in a larger incidence angle for Diffuser 3 was due to the fact that the effective throat area is very close to the sonic throat area for an incidence angle of -1˚, i.e. $A_{th}/A^* = 1.04$.

The shape of the leading edge of Diffuser 4 should contribute to the reduction in flow losses and boundary layer growth in the downstream diffuser throat.

b) Vane camberline and blade thickness

Once the leading and trailing edge geometry have been established in VDDESIGN the vane thickness distribution on the blade mean camberline is specified. The mean camberline is determined from the analysis and procedures described in Chapter 9 of Aungier (2000). VDDESIGN offers various choices to specify the vane thickness distribution. The option whereby the vane thickness distribution is specified by a constant thickness with a linear taper to a smaller leading edge thickness over the length of the camberline is used. According to Aungier (2000) a thick vaned diffuser requires a substantially larger discharge-to-

inlet radius ratio (r_4/r_3) to achieve the same pressure recovery as the conventional thin-vaned or airfoil type diffusers.

Diffuser 1 has a straight camberline from inlet to discharge with a length of 18.5 mm and a discharge vane thickness ($t_{b,4}$) of 7.5 mm. A point of concern in Diffuser 1 is the assumption that air revolves behind the radial vanes in the diffuser prior to being directed into the axial direction, due to the 90˚ vaneless bend between the exit of the radial vanes and inlet of the axial blades. The abrupt or sudden area expansion (90˚ vaneless bend) behind the radial vanes contributes to a reduction in the air velocity prior to entering the combustion chamber. However, the expansion can also lead to extended boundary layer growth behind the islands creating rotating stall and increase the swirl component of the flow, reducing the operating flow range. The diffuser passage lengths (camberline length) of Diffuser 2 and 3 are slightly decreased due to the increased inlet blade angles and vane geometry. It was therefore decided to increase the diffuser discharge radius (r_4) from 46.5 mm to 48 mm for Diffuser 2 and 3. This resulted in camberline lengths of 21.4 mm and 16.1 mm for Diffuser 2 and 3 respectively. Diffuser 4 has a camberline length of 19.5 mm and a discharge radius of 46.5 mm. The vane pitch-to-chord ratio and depth-to-chord ratio for each Diffuser are indicated in Table 6.4.

Table 6.4: Diffuser pitch-to-chord and depth-to-chord ratios

Diffuser	h_{th}/c	b/c
1	0.32	0.36
2	0.14	0.31
3	0.19	0.41
4	0.24	0.34

Both the pitch-to-chord and depth-to chord ratios are relatively small as seen in Table 6.4 and will therefore be well approximated by 1-D flow theory as stated by Au (1991), bearing in mind that Diffuser 4 should rather be investigated using a 3-D (CFD) approach, due to its twisted vane geometry.

The diffuser discharge vane thickness ($t_{b,4}$) is subject to the vane divergence angle and area ratio. The diffuser vane thicknesses are included in Table E.2 for each diffuser.

c) Diffuser area ratio, blade loading and pressure recovery coefficient

The static pressure recovery in the conventional vaned diffuser depends on two basic diffusion mechanisms, namely, (1) the effective passage area increase from inlet to discharge which is augmented by (2) the fluid turning or blade loading effect, (Aungier, 2000). The best diffuser performance is achieved when both these basic diffusion mechanisms operate close to their maximum limits and will substantially deteriorate if these limits are exceeded (Aungier, 2000). These limits are indicated in Equations 6.10 and 6.11. The blade passage length (L_B) and effective passage width (W) are defined by

$$L_B = \int_{r_3}^{r_4} \frac{dr}{sin\,\beta} \tag{6.5}$$

$$W = \frac{2\pi r sin\beta}{z} \tag{6.6}$$

The radial diffuser discharge sizing is based on three parameters, namely the equivalent divergence angle ($2\theta_C$), the blade loading parameter (L) and the area ratio (A_R). The equation that defines each parameter is given below.

$$tan\theta_C = \frac{\pi(r_4 sin\beta_4 - r_3 sin\beta_3)}{ZL_B} \tag{6.7}$$

$$L = \frac{2\pi(r_3 C_{U3} - r_4 C_{U4})}{ZL_B(C_3 - C_4)} \tag{6.8}$$

$$A_R = \frac{r_4 sin\beta_4}{r_3 sin\beta_3} \tag{6.9}$$

The recommended design limits for Equations 6.7 and 6.8 are

$$2\theta_C \leq 11° \tag{6.10}$$

$$L \leq \frac{1}{3} \tag{6.11}$$

These design limits provide guidance in the diffuser design process. The respective parameters for each diffuser are included in Tables 6.3 and 6.4. It should be noted that for the given diffuser constraints (Section 6.3) the various trade-offs between parameters to achieve these design limits prove to be very important when designing for maximum pressure recovery. Not all the design constraints can be satisfied, since there are simply not enough degrees of freedom in the flow domain. Different values for R, A_R and z are simulated in VDDESIGN to determine the best combination of $2\theta_C$, L and A_R. VDDESIGN allows the designer to specify alternate values for specific design parameters.

The blade loading parameter is evaluated by the blade-to-blade flow analysis of Chapters 12 through 14 in Aungier (2000). The blade loading magnitude should be limited by the following criteria

$$\frac{|C_s - C_p|}{C_{avg}} < 0.4 \tag{6.12}$$

where C_s and C_p are the vane surface velocities on the suction and pressure surfaces and C_{avg} is an average of these two values (Aungier, 2000). Aungier states that this is regarded as a maximum limit and that a limit of 0.35 is preferred if possible. Diffuser 2, 3 and 4 all comply with this criteria as seen in Table 6.5.

Reneau et al. (1967) provided two-dimensional diffuser performance maps that indicate an area ratio of between 2.2 – 2.4 to be optimum for the inlet blockage

that is expected in a vaned diffuser. The area ratios for diffuser 2, 3 and 4 vary between 2 and 3 as seen in Table 6.6.

Table 6.5: Blade loading criteria

Diffuser	L	$\lvert C_s - C_p \rvert / C_{avg}$		
		Vane inlet	Vane discharge	Vane Average
1	0.69	1.30	0.04	0.67
2	0.39	0.44	0.01	0.23
3	0.63	0.77	0.02	0.40
4	0.77	0.7	0.05	0.38

The static pressure recovery coefficient is given by

$$c_p = \frac{p_4 - p_3}{p_{t,3} - p_3} \tag{6.13}$$

As aforementioned the goal of this thesis is to design an efficient diffuser with a maximum pressure recovery. From Table 6.6 it can clearly be seen that the 3 new diffusers all have a much higher static pressure recovery, often at the expense of the blade loading limit. However, when considering the pressure recovery and blade loading of Diffuser 1, the 3 new diffusers outperform Diffuser 1 based on these two parameters.

Aungier (2000) also introduces a design parameter (*E*) which evaluates the effectiveness of the vaned diffuser design as opposed to that of a vaneless diffuser. The effectiveness is defined by

$$E = \frac{R^2(A_r^2 - 1)}{A_r^2(R^2 - 1)} \tag{6.14}$$

This parameter illustrates the practical merit of using vaned diffusers. R is defined as the radius ratio r_4/r_3.

Table 6.6 indicates the divergence angle of each diffuser as modelled in SolidWorks, the effective divergence angle predicted by VDDESIGN, as well as the blade loading, area ratio, discharge Mach number, diffuser effectiveness and total loss coefficients over the diffusers.

The divergence angle for Diffuser 3 is 8.4˚ for the section between the vane leading edge ($r_3 = 38\,mm$) up to a radius of 43 mm, thereafter the vanes are turned into the radial direction as seen in Figure 6.4 and the divergence angle varies accordingly along the camberline. Also note the drop in discharge Mach number (Ma_4) for Diffusers 2, 3 and 4 relative to Diffuser 1.

Table 6.6: Design point parameters as predicted by VDDESIGN

Diffuser	Divergence angle (SolidWorks) $[2\theta_C]$ in ˚	Effective divergence angle (VDDESIGN) [˚]	L	A_R	c_p	Ma_4	E	*Total LC*
1	9.0	10.6	0.69	2.85	0.48	0.47	2.7	0.16
2	8.5	7.0	0.39	2.00	0.61	0.38	2.6	0.15
3	8.4	18.8	0.63	3.06	0.73	0.25	3.1	0.16
4	11.3	16.3	0.77	2.50	0.62	0.37	2.6	0.14

d) Number of Vanes Selection

The number of diffuser vanes selected is based on both aerodynamic and resonance considerations. Resonance is more likely to occur when the number of diffuser vanes equal the number of impeller blades, $z_{VD} = z_I$. If the number of vanes is not calculated correctly the amplitude of pressure pulsations will increase in the vaneless space, causing an increase in static pressure field distortions (Bennett, Tourlidakis & Elder, 2000). The preferred choice for selecting the number of diffuser vanes is stated as $z_{VD} = z_I \mp 1$ according to Aungier (2000). Aungier recommends between 10 and 20 vanes. However, if the preferred number of vanes is not in this range Aungier provides the following criteria:

$$|z_{VD} - z_I| \geq 8 \qquad 6.15$$

The effective number of impeller blades is calculated to be, $z_I = 13$, by using Equation 6.16. Diffuser 1 has 15 radial diffuser vanes which comply with Aungier's recommended choice. However, a maximum pressure recovery coefficient was observed in VDDESIGN when 30 vanes were selected for both Diffuser 2 and 3 designs. The temptation to design passages with a gradual increase in passage width was avoided since this raises the risk of separation on the vane walls that cause flow instability. By selecting more vanes the diffusion process was improved due to a reduced passage divergence angle that reduces the boundary layer growth on the vane walls.

$$z_I = z_{FB} + \frac{z_{SB} L_{SB}}{L_{FB}} \qquad 6.16$$

Diffuser 4 is designed with 15 radial vanes to make machining of the part with a 5-axis machine with small tool bits possible. Diffuser 4 was also investigated in VDDESIGN with 13 vanes, but this proved to deteriorate the blade loading and divergence angle parameters.

Diffuser 1 has 42 axial blades downstream of the radial vanes. The function of the axial blades is to redirect the whirling flow exiting the radial vanes into the axial direction prior to entering the combustion chamber.

Diffusers 2, 3 and 4 are all designed with 30 axial blades. The reason for decreasing the number of blades was to increase the flow area which further initiates diffusion by decreasing the blade solidity.

e) Vaned Diffuser Stall and losses

Aungier (2000) developed the following stall criterion for vaned diffusers:

$$K + K_0 = 0.39 \tag{6.17}$$

K represents an average value between the vane inlet and throat which is approximated by Equation 6.18, and K_0 (Equation 6.19) is an "unguided" value that includes Mach number effects which is derived from the basic fluid dynamics equation of motion in a radial, vaneless space of constant width with a flow angle equal to the vane inlet angle (Aungier, 2000).

$$K = \frac{r_3}{h_{th}}\left[\frac{cos\alpha_3}{cos\alpha_{th}} - 1\right] \tag{6.18}$$

$$K_0 = \frac{M_3^2 sin^2\beta_3 cos\beta_3}{1 - M_3^2 sin^2\beta_3} \tag{6.19}$$

The inlet flow angle (α_3), inlet blade angle (β_3) and the number of vanes (z_D) are the dominant factors affecting diffuser stall. The stall incidence angle is also determined from Equation 6.17 and is shown in Figures F.1 to F.4. Diffuser 1 is well below the stall limit as seen in Figure F.1. Diffusers 2 and 4 also fall below the stall limit; however Diffuser 3 falls in the stall limit predicted by Aungier (2000). This is due to trade-off decisions made between blade loading, divergence angle and the stall limit to achieve a maximum pressure recovery. The incidence angle for Diffuser 3 is predicted by VDDESIGN to be 1.95 and the limiting stall incidence angle is computed to be 1.74. Vaned diffusers designed with low inlet blade angles and a low number of vanes will tend to show a wider stable operating range (Aungier, 2000). More successful vaned diffusers will generally have an inlet blade angle between $16° \leq \beta_3 \leq 22°$ (Aungier, 2000). All the diffuser inlet blade angles are more or less in this range as seen in Table 6.2.

The loss models used in CompAero are defined in Chapter 5 of Aungier (2000), and will not be discussed here.

The total pressure at the vaned diffuser outlet as computed in VDDESIGN is given by:

$$p_{t,4} = p_{t,3} - (p_{t,3} - p_3)\sum_i \bar{\omega}_i \tag{6.20}$$

Where $\bar{\omega}$ is the total pressure loss coefficient.

7 VANED DIFFUSER PERFORMANCE EVALUATION

7.1 Analysis of the Designs and Discussion

The performance of each diffuser design was firstly evaluated in CompAero by predicting the aerodynamic performance of each compressor configuration and then simulated in FINE™/Turbo. The 1-D and CFD overall performance predictions, from impeller inlet (1) to radial diffuser discharge (4) of each diffuser is supplied in Table 7.1 and shown in Figures 7.11 and 7.12. From the figures it can clearly be seen that Diffuser 2, 3 and 4 all predict a higher total-to-static pressure recovery at a higher mass flow rate. The 1-D and CFD results at the design point for the new diffusers differ slightly. The CFD results predict a lower total-to-static pressure recovery when compared to the 1-D results. The same trend was observed for the results of Diffuser 1 during validation of the 1-D and CFD analyses, as seen in Figure 5.2, with the 1-D total-to-static predictions performing better than the CFD results. Nonetheless Diffusers 2, 3 and 4 still predict a higher pressure recovery for both numerical approaches, with Diffuser 3 delivering the best pressure recovery in both instances, (Table 6.6 and 7.1).

Table 7.1: Overall compressor performance predictions

Diffuser	**1**		**2**		**3**		**4**	
	1-D	CFD	1-D	CFD	1-D	CFD	1-D	CFD
$PR_{TS,0-4}$	2.69	2.60	2.78	2.68	2.93	2.74	2.82	2.62
$PR_{TT,0-4}$	3.12	3.15	3.07	3.09	3.06	3.13	3.09	3.18
$\eta_{TT,0-4}$ [%]	80.6	80.7	80.2	79.9	80.0	80.1	80.9	81.1

When considering the results of the numerical analyses, it was clear that the three new diffuser designs predicted a higher total-to-static pressure recovery at a higher mass flow rate, i.e. 0.3 kg/s. Diffuser 2 was found to operate the closest to its choke limit, i.e. $A_{th}/A^* = 1.122$, but even this value proved to be more than acceptable, whilst the choke criteria for Diffuser 3 was found to be the furthest from the choke limit when comparing the 4 diffusers. Not one of the four diffusers predicted a value for the choking loss coefficient (LC), i.e. choking LC = 0. VDDESIGN predicted the lowest total loss coefficient for Diffuser 4 (total LC = 0.14) and the largest total loss coefficient predicted was similar for Diffuser 1 and 3 (total LC = 0.16).

Diffuser 1 had an incidence loss coefficient of 0.0409 with a blockage loss coefficient of 0.0243. The three new diffusers matched the flow better than Diffuser 1, with Diffuser 2 having the lowest incidence loss coefficient of 0.0205. However, the improved incidence angles resulted in slightly larger blockage loss coefficient predictions. Diffusers 2 and 3 had an improved blade loading

parameter when compared to Diffuser 1, yet the predicted blade loading value still exceeded Aungier's (2000) recommended blade loading criteria of 0.33.

VDDESIGN predicted the smallest area ratio for Diffuser 2 ($A_R = 2$) and the largest for Diffuser 3 ($A_R = 3.06$). The larger area ratio also resulted in the greatest pressure recovery ($c_P = 0.73$). Japikse and Baines (1998) stated that a static pressure recovery of between 0.2 and 0.5 is considered acceptable for turbomachinery with a restricted radial length. Therefore a pressure recovery for Diffuser 3 of 0.73 is considered very good. Diffuser 1 predicted a pressure recovery of 0.48. In addition to the pressure recovery the absolute Mach number was also reduced for the three new diffusers. Figures D.20 to D.23 indicate the absolute Mach number distribution for Diffusers 1 to 4 respectively.

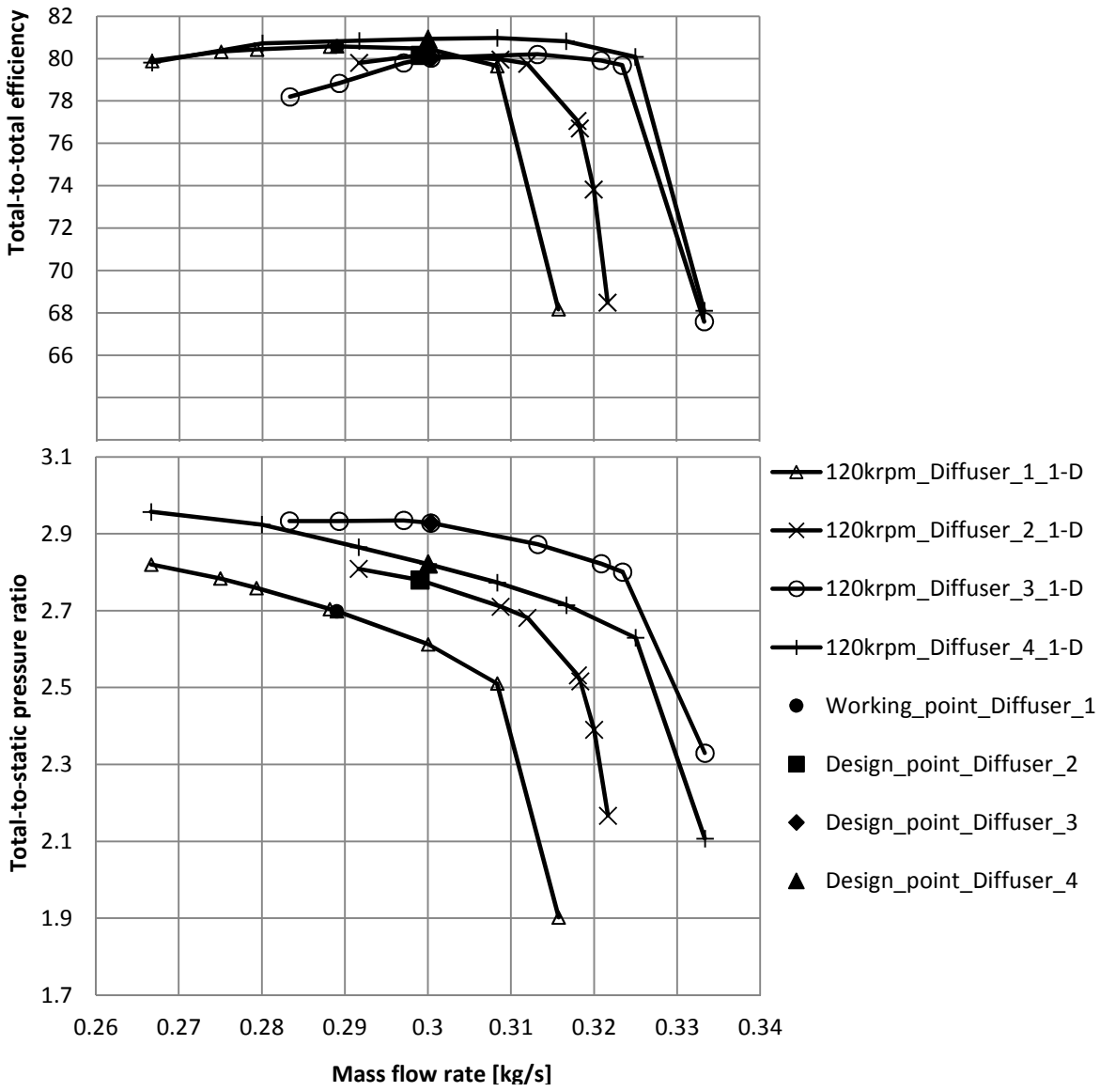

Figure 7.1: 1-D total-to-static pressure ratio and total-to-total efficiency

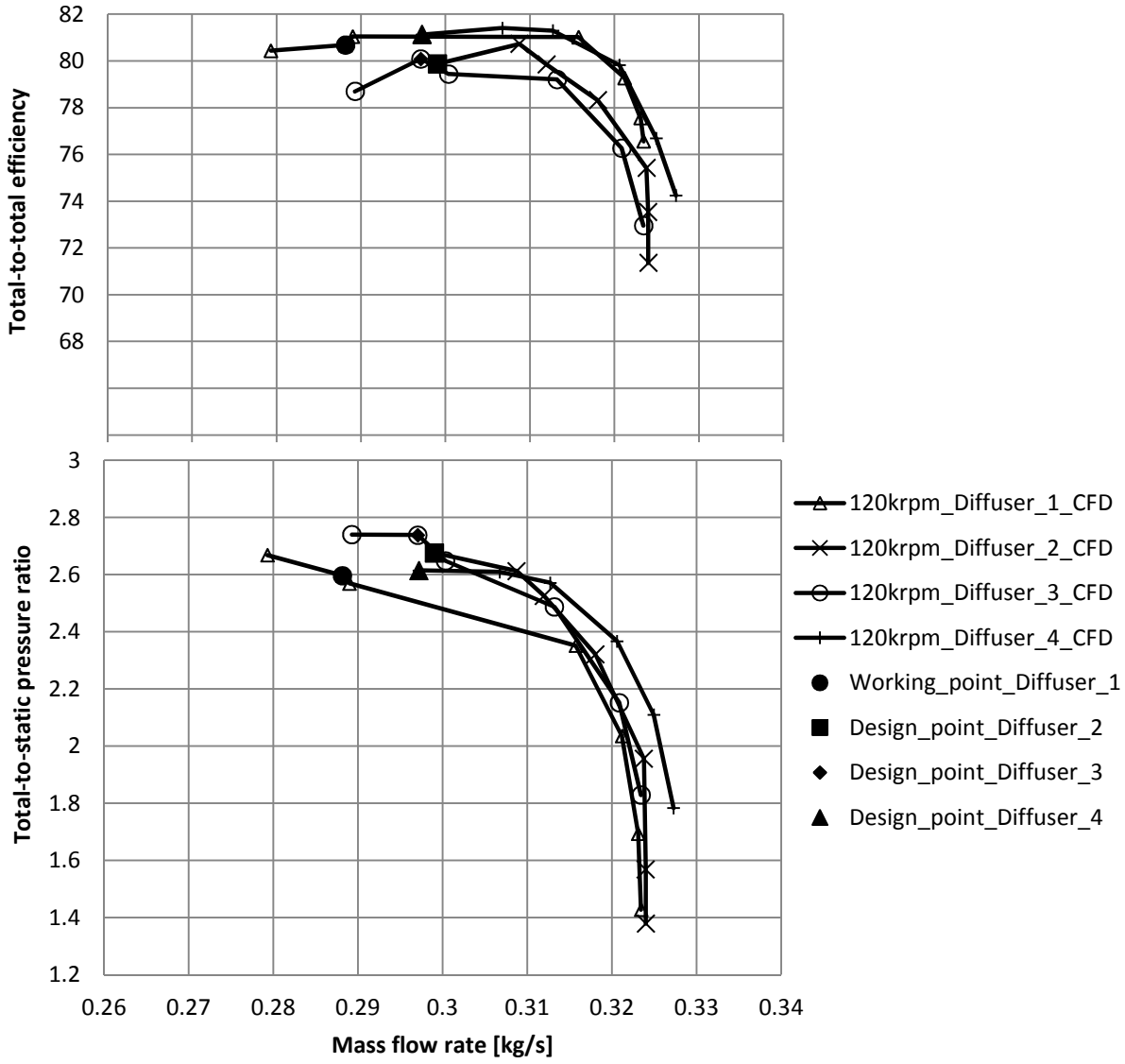

Figure 7.2: CFD total-to-static pressure ratio and total-to-total efficiency

Aungier (2000) states that when designing a vaned diffuser for maximum pressure recovery, the vaned diffuser will always be designed for a diffusion level that shows substantial separation in the vane surface boundary layers (Figure 6.8) as was the case in all the diffuser configurations.

Since the vane geometry of Diffuser 4 varies from hub to shroud, the CFD performance predictions were assumed to be more accurate for these twisted flow passages. Therefore based on the total-to-static pressure recovery results (Figure 7.2), it was decided to machine and test the two best performing diffusers, namely Diffusers 2 and 3.

7.2 Experimental Results

The experimental tests were performed on Diffusers 1, 2 and 3. The working line of each compressor configuration, operating at its respective ambient temperature and pressure conditions as recorded in the test facility, is indicated in Figures 7.3 and 7.4. Figure 7.4 displays the working line of each diffuser for rotational speeds between 100 krpm and 125 krpm. Included on the performance maps in Figures 7.3 and 7.4 are the 1-D and CFD design point predictions for Diffusers 2 and 3, i.e. design mass flow rate of 0.3 kg/s and rotational speed of 120 krpm at ambient conditions of 283 K and 100 kPa. The mass flow rates for the three respective diffusers are presented as non-dimensional values in Figures 7.3 to 7.6. A non-dimensional mass flow rate is used to account for variations in ambient temperature and pressure conditions between tests. The ambient temperature and pressure for the tests performed on Diffuser 1 were recorded as $T_{t,0} = 283\ K$ and $p_{t,0} = 100\ kPa$ respectively. These conditions were also used for the validation of the 1-D and CFD analyses. The ambient temperature and pressure for Diffusers 2 and 3 were recorded as $T_{t,0} = 294\ K$ and $p_{t,0} = 100\ kPa$. From the results indicated in Figure 7.3 Diffuser 3 (at ambient conditions of 294 K and 100 kPa) achieved a higher mass flow rate than Diffuser 1 (at ambient conditions of 283 K and 100 kPa), as well as an improved static pressure recovery at the recorded operating points between the engine idling speed (34 krpm) and 110 krpm. This resulted in increased thrust delivered by the engine at the respective operating points between 50 krpm and 110 krpm as seen in Figures 7.5 and 7.6. This also contributes to improved acceleration of the engine from idling speed to maximum thrust in a reduced time, adding to the attractiveness of using a gas turbine in UAV's or hobby jets.

When comparing the engine test data of each diffuser configuration at its respective ambient operating conditions, Diffuser 1 (at ambient conditions of 283 K and 100 kPa) delivered the highest total-to-static pressure recovery, 2.62, at 120 krpm, at the expense of a high mass flow rate (Table 7.2). The gas turbine assembled with Diffuser 2 and 3 (at ambient conditions of 294 K and 100 kPa) produced a higher thrust than the Diffuser 1 configuration at 120 krpm and 125 krpm, with Diffuser 3 producing the highest thrust, 120.9 N, at 125 krpm, compared to 117.4 N thrust produced by Diffuser 1. During the experimental investigation it was observed that both Diffuser 2 and 3 achieved a higher static-to-static pressure ratio over the radial diffuser, i.e. between the impeller tip and the radial diffuser exit, p_4/p_2, as seen in Tables 7.2 and 7.3. Diffuser 3 obtained the highest static-to-static pressure ratio over the radial diffuser, improving the static-to-static pressure ratio from 1.39 for Diffuser 1 to 1.44 for Diffuser 3 at 120 krpm and from 1.41 for Diffuser 1 to 1.50 for Diffuser 3 at 125 krpm (Table 7.2 and 7.3). However, despite these results, the variation of the ambient conditions in the test facility was further investigated to determine the effect of the temperature and pressure variations on the engine performance. The difference in the ambient pressure between tests was recorded to be 200 Pa and therefore considered negligibly small. However, the effect of the temperature variation on the engine performance was examined to determine the effective engine rotational speed, thrust and total-to-static pressure ratio of Diffuser 2 and 3 relative to Diffuser 1, if it were tested at the same operating conditions as that of Diffuser 1.

The following calculations were performed to determine the effective difference in engine performance due to the variations in the ambient conditions between tests in the test facility. The ratio (R_{amb}) between the impeller Mach numbers, based on the ambient temperature conditions is calculated by:

$$R_{amb} = \sqrt{\frac{T_{t,0\ (294\ K)}}{T_{t,0\ (283\ K)}}} = 1.019 \tag{7.3}$$

Correcting for this ratio results in an corrected rotational speed (Equation 6.4) of 117.7 krpm for Diffuser 2 and 3 at 294 K, compared to the 120 krpm for Diffuser 1 at 283 K; and an corrected rotational speed of 122.6 krpm for Diffuser 2 and 3 at 294 K compared to 125 krpm for Diffuser 1 at 283 K.

$$Corrected\ RPM = \frac{RPM_{(120\ krpm)}}{R_{amb}} = 117.7\ krpm \tag{7.4}$$

Figures 7.7 and 7.8 indicate the engine thrust against a non-dimensional rotational speed. The engine delivers a thrust of 108.7 N with the assembled Diffuser 3 configuration, at an ambient temperature of 294 K and a rotational speed of 120 krpm (Figure 7.8), however if the engine with the same diffuser configuration operates at an ambient temperature of 283 K with the adjusted 120 krpm, a thrust of 114 N can be expected. This is achieved by using a curve fit through the data points from 50 krpm up to 125 krpm and interpolating between points, as seen in Figure 7.8 and 7.9. Therefore the engine, assembled with the new diffuser configurations, will perform much better at the same ambient conditions as that of Diffuser 1, i.e. at 283 K and 100 kPa, resulting in an improved total-to-static pressure ratio as seen in Figure 7.9 and engine thrust as seen in Figure 7.8. In addition, the Mach number over the radial diffuser is lower for Diffusers 2 and 3, allowing the engine to be operated at higher rotational speeds.

When considering the results of Figure 7.4 and Table 7.2 it is seen that both Diffuser 2 and 3 could not obtain the design mass flow rate of 0.3 kg/s at a rotational speed of 120 krpm when tested at ambient conditions of 294 K and 100 kPa. A mass flow rate of 0.297 kg/s and 0.296 kg/s were achieved at a rotational speed of 125 krpm for Diffuser 2 and 3 respectively at the same ambient conditions. However, when considering the predicted performance of the engine with the new diffuser configurations at ambient conditions of 283 K and 100 kPa; and judging by the gradient of the compressor working lines in Figure 7.3, the design mass flow rate of 0.3 kg/s would be achieved, since the effective rotational speed of 117.7 krpm would be increased to 120 krpm, increasing both the mass flow rate and total-to-static pressure ratio. Therefore the design point conditions are likely to be reached if the engine operates at the same ambient conditions as that of Diffuser 1, i.e. 283 K and 100 kPa.

It can therefore also be concluded that care should be taken when testing the micro gas turbine at different ambient conditions, since this will have an effect on the overall engine performance.

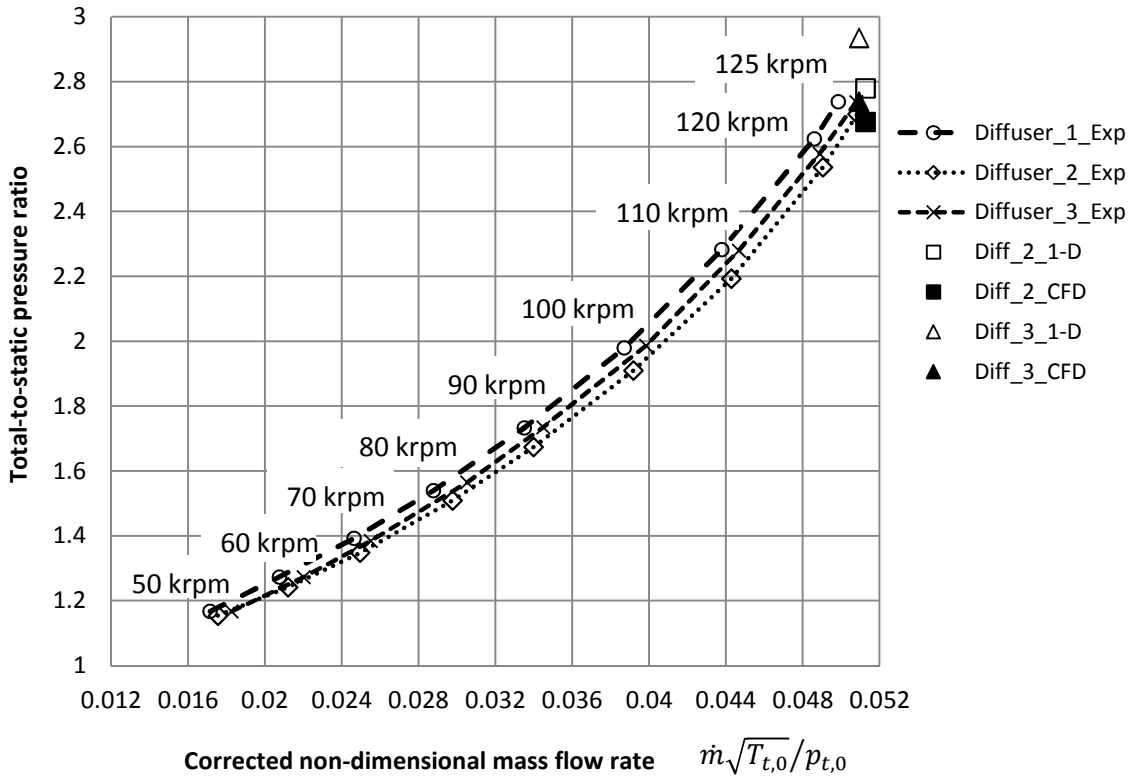

Figure 7.3: Total-to-static performance map

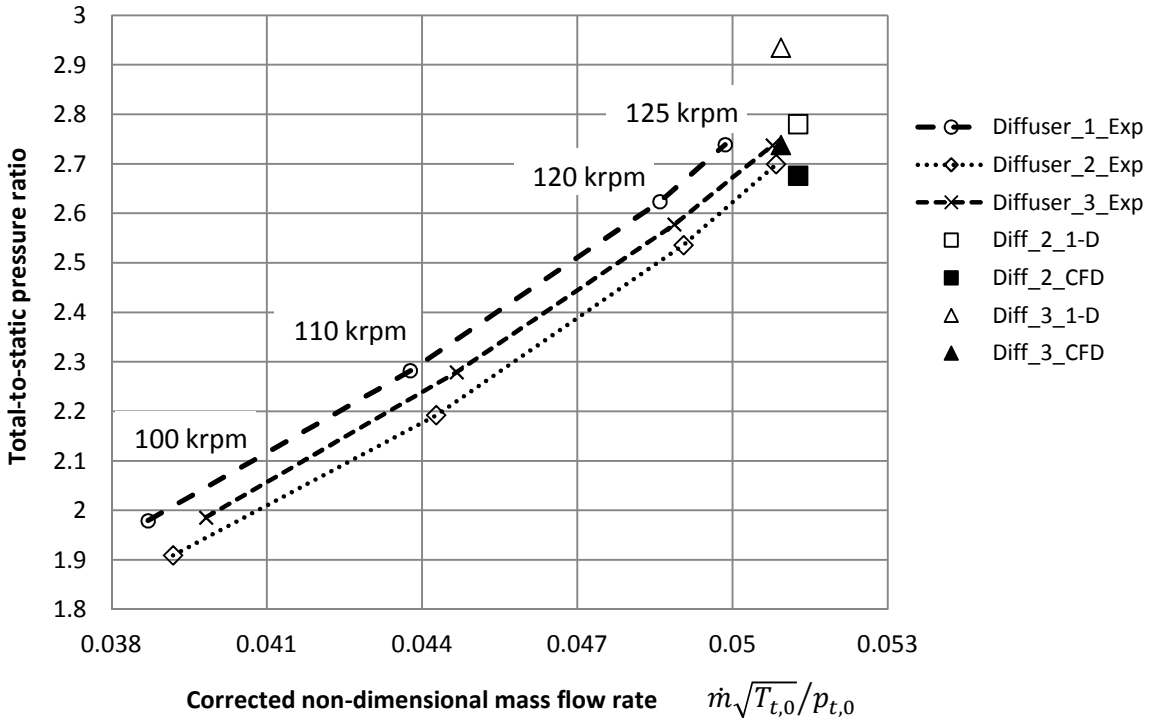

Figure 7.4: Total-to-static performance map for rotational speeds between 100 krpm to 125 krpm

Table 7.2: Data comparison of Diffuser 1,2 and 3 at 120 krpm

Diff 1	**kRPM**	$N/\sqrt{T_{t,0}}$	$\dot{m}$ **[kg/s]**	$\dot{m}\sqrt{T_{t,0}}/p_{t,0}$	$p_4/p_{t,1}$	p_4/p_2	**Thrust**
1-D	120	7.13	0.289	0.0486	2.69	1.27	
CFD	120	7.13	0.288	0.0486	2.60	1.25	
Exp	120	7.13	0.288	0.0486	2.62	1.39	107.3
Diff 2	**kRPM**		$\dot{m}$ **[kg/s]**	$\dot{m}\sqrt{T_{t,0}}/p_{t,0}$	$p_4/p_{t,1}$	p_4/p_2	
1-D	120	7.00	0.299	0.0513	2.78	1.33	
CFD	120	7.00	0.299	0.0513	2.68	1.32	
Exp	120	7.00	0.286	0.0491	2.54	1.42	107.9
Diff 3	**kRPM**		$\dot{m}$ **[kg/s]**	$\dot{m}\sqrt{T_{t,0}}/p_{t,0}$	$p_4/p_{t,1}$	p_4/p_2	
1-D	120	7.00	0.297	0.0509	2.93	1.40	
CFD	120	7.00	0.297	0.0509	2.74	1.32	
Exp	120	7.00	0.285	0.0489	2.58	1.44	108.7

Table 7.3: Performance comparison of Diffuser 1,2 and 3 at 125 krpm

Diff	**kRPM**	$N/\sqrt{T_{t,0}}$	$\dot{m}$ **[kg/s]**	$\dot{m}\sqrt{T_{t,0}}/p_{t,0}$	$p_4/p_{t,1}$	p_4/p_2	**Thrust**
1	125	7.43	0.296	0.0499	2.74	1.41	117.4
2	125	7.29	0.297	0.0508	2.70	1.49	120.8
3	125	7.29	0.296	0.0508	2.73	1.50	120.9

Based on Table 7.2 a deviation of 11.9% exists between the experimentally recorded total-to-static pressure ratio and the predicted 1-D design point for Diffuser 3. The 1-D analyses over predict the total-to-static pressure ratio for the diffuser when compared to the experimental and CFD results. When comparing the experimental total-to-static pressure ratio of Diffuser 3 with the actual 1-D prediction at the same mass flow rate, i.e. 0.285 kg/s, the deviation in the results reduces to 9%. The reason for the deviation in the results can be assigned to the fact that the blade loading criteria during the design process are not within the required limits that are provided by Aungier (2000) and thus a deterioration in performance can be observed. The CFD design point predictions compare better to the experimental data at 120 krpm than the 1-D predictions.

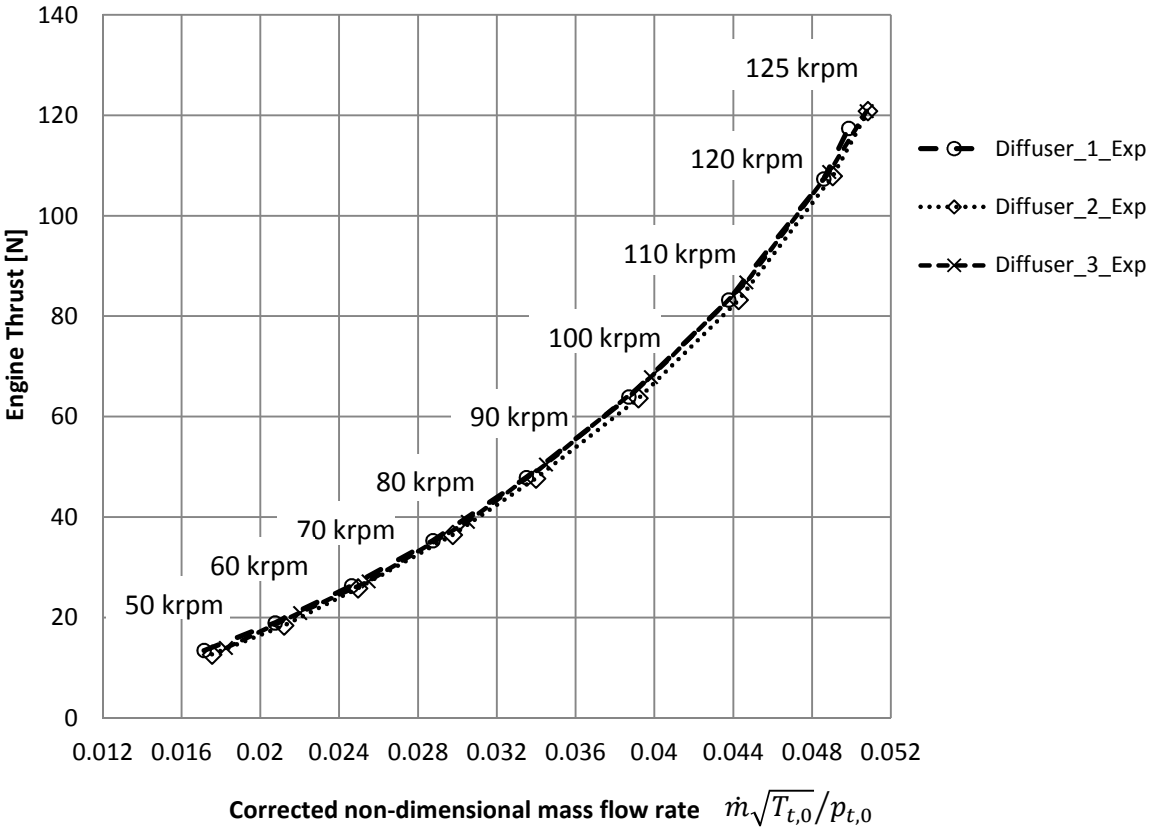

Figure 7.5: Engine thrust comparison

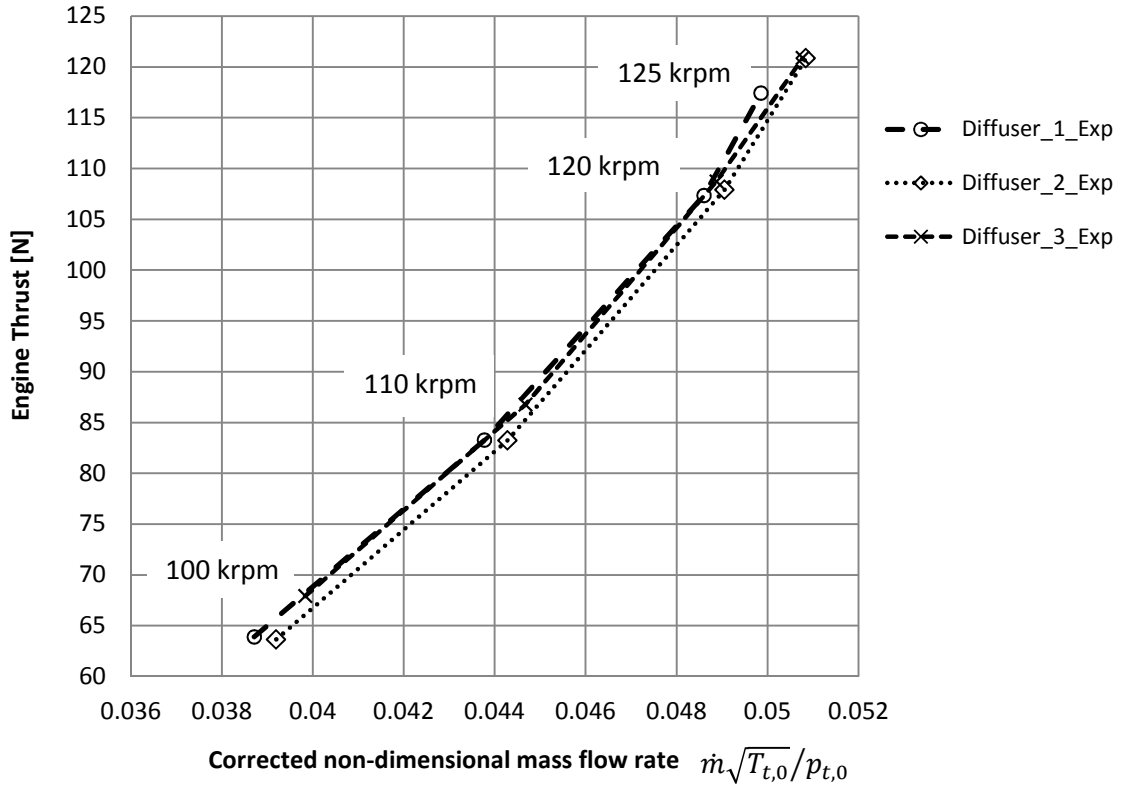

Figure 7.6: Engine thrust for rotational speeds between 100 krpm and 125 krpm

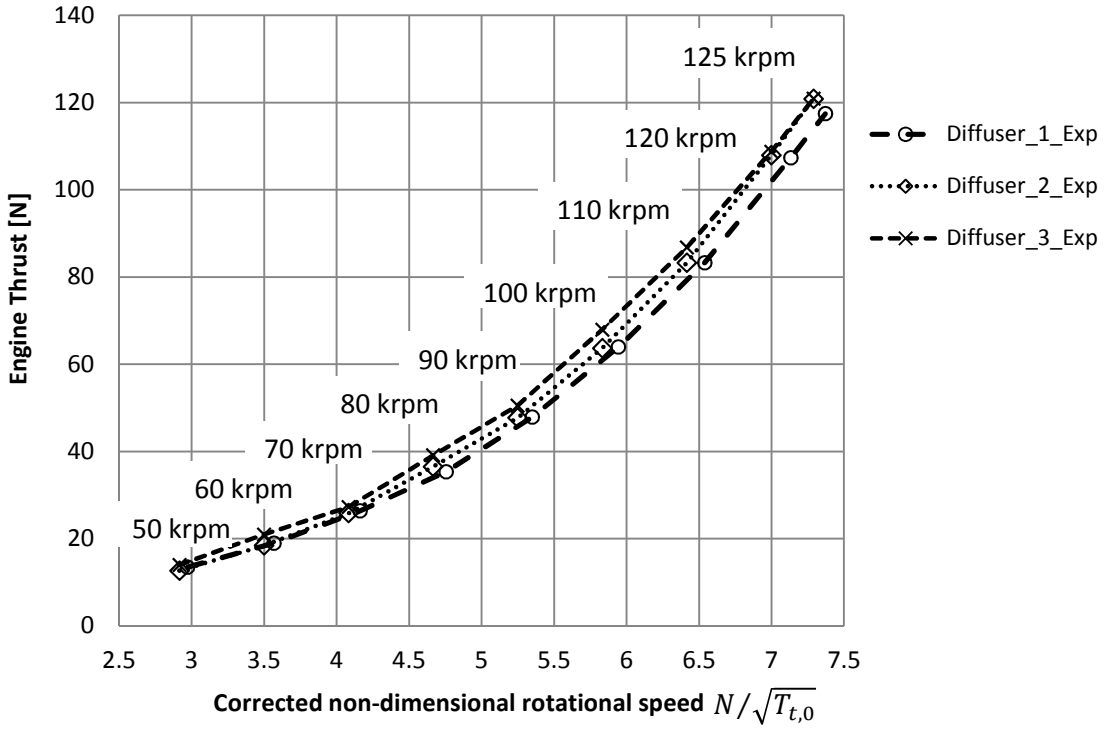

Figure 7.7: Engine thrust with non-dimensional rotational speed

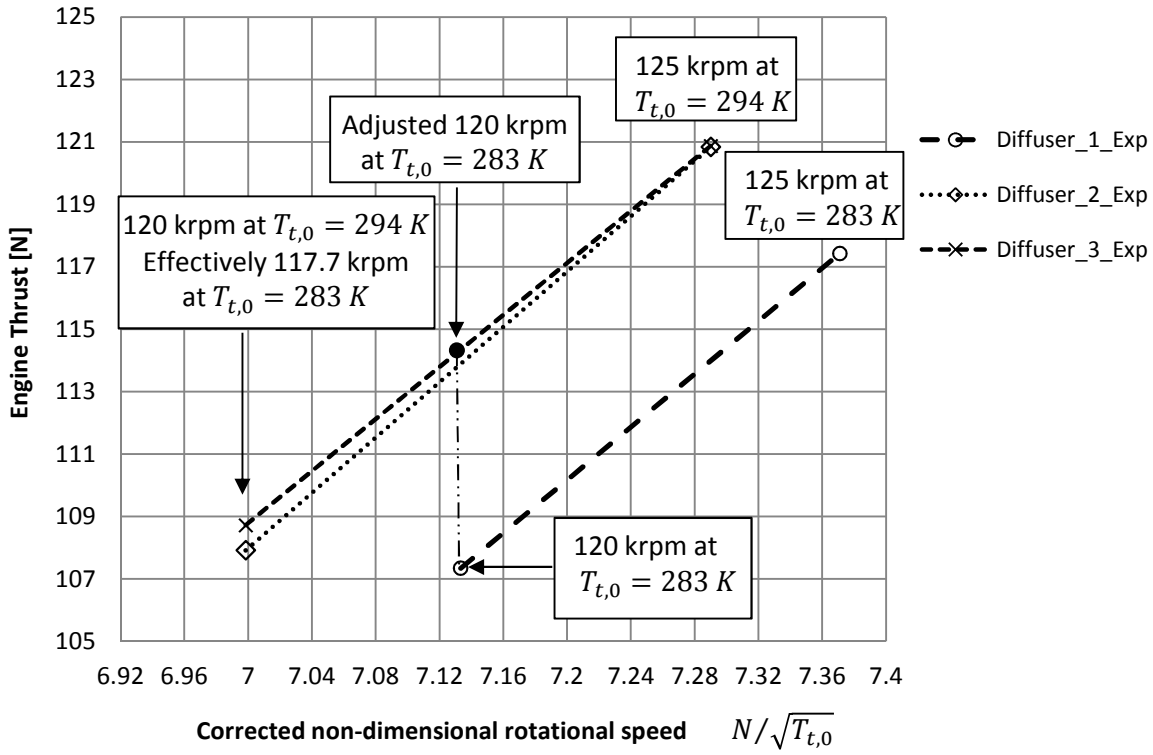

Figure 7.8: Engine thrust for non-dimensional rotational speeds between 120 krpm and 125 krpm

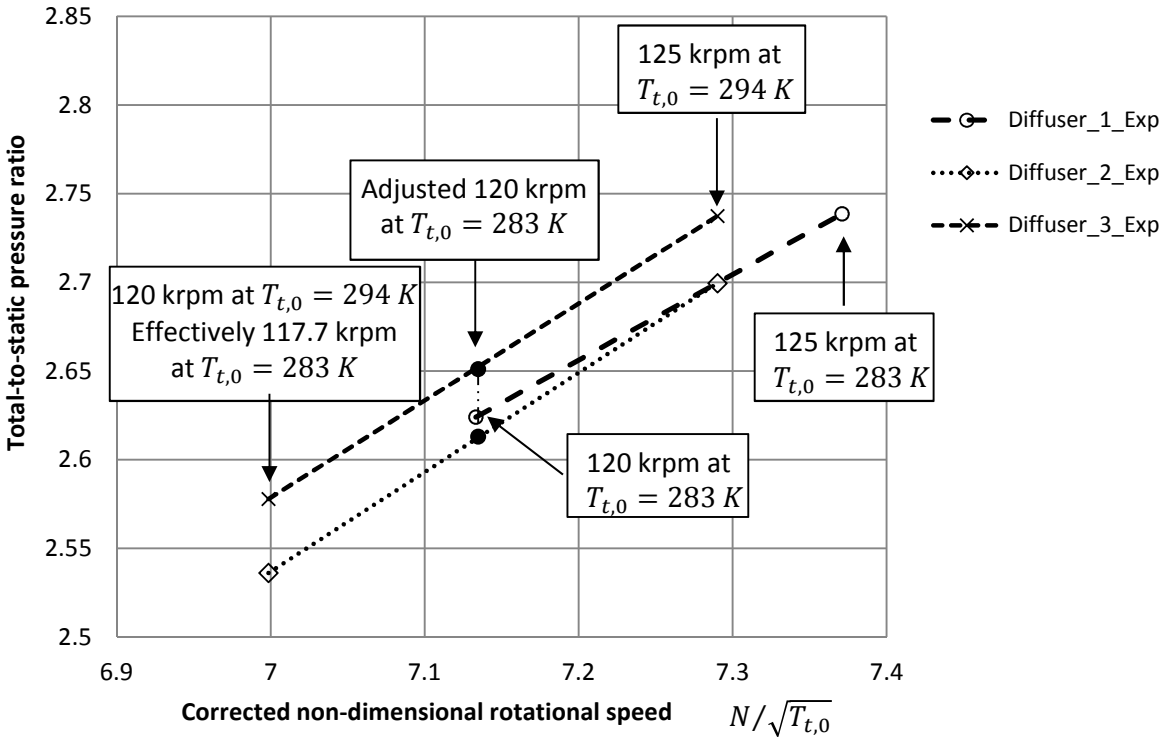

Figure 7.9: Total-to-static pressure ratio for non-dimensional rotational speeds between 120 krpm and 125 krpm

7.3 Experimental Evaluation Conclusion

From the results and data obtained during the experimental investigations, it is clear that special care need to be taken when constructing a micro gas turbine test bench with all necessary measuring equipment and testing the gas turbine in the test facility. Errors during testing, may it be round off errors or errors in the measuring equipment can easily creep in if not thoroughly checked. These may affect the validity of the results as well as the 1-D and CFD validation processes. Good repeatability of the recorded results is also crucial to the justification of the test bench. As aforementioned, the micro gas turbine is very sensitive to variations in ambient conditions and clearly affects the results if tests are not performed at the same ambient conditions.

Nonetheless an improvement over the original diffuser configuration (Diffuser 1) was achieved by Diffusers 2 and 3, more specifically Diffuser 3, by increasing the mass flow rate, engine thrust and static-to-static pressure ratio.

8 CONCLUSION AND RECOMMENDATIONS

In the presented study, a set of numerical simulations and experimental tests have been performed to assess the effect of changing the diffuser vane geometry and evaluate its influence on the compressor stage performance. The following section summarizes the findings of the investigation and offer future recommendations for further work to continue developing the micro gas turbine.

8.1 Conclusions

Through the CompAero and Fine™/Turbo software packages the development of a computer model of the centrifugal compressor have shown that, by combining the principles of thermodynamics and mechanics and relating it to measured data, it is possible to obtain meaningful results, despite the lack of comprehensive measurement locations on the micro gas turbine due to limited space. The VDDESIGN program assists the designer to achieve the best possible diffuser configuration if the designer adheres to the diffuser design criteria stipulated by Aungier (2000). The critical design parameters or criteria include: the effective divergence angle, the blade loading parameter and the area ratio. A vast deterioration in compressor performance can be expected if this criterion is not met.

The combined experimental and numerical analysis of the centrifugal compressor showed that flow predictions over the compressor give the designer an opportunity to estimate accurately the effects of different factors on the compressor performance and operating range. This allows the designer to match flow paths and new requirements without considerable effort.

Experimental tests were performed on Diffusers 1, 2 and 3 and compared to the 1-D and CFD predictions. Concluding from the compressor maps in Figures 7.3 and 7.4, the results listed in Tables 7.2 and 7.3, and the experimental data Tables in Appendix E, it is clear that Diffuser 3 achieves the best static pressure ratio, p_4/p_2, over the radial diffuser, with an increase from 1.39 to 1.44 at 120 krpm and an increase from 1.41 to 1.50 at 125 krpm. However, Diffuser 1 obtained the highest static pressure recovery, $p_4/p_{t,1}$, at 120 krpm and ambient conditions of 283 kPa and 100 kPa, at the expense of mass flow rate. According to Baird (2011), the original diffuser, Diffuser 1, with the respective KKK K27.2 impeller is already operating near its optimum point at 120 krpm. This was confirmed with the experimental tests. Both CompAero and Fine™/Turbo predicted an improved static pressure recovery for Diffuser 2 and 3. The CFD predictions are however slightly more accurate when compared to the experimental results as seen in Figures 7.3 and 7.4.

Both Diffuser 2 and 3 achieve a higher mass flow rate than Diffuser 1 and the engine delivers a greater thrust for both new diffuser configurations. This is due to the improved incidence between the flow angles and diffuser inlet vane angles.

The thrust delivered by the engine for Diffuser 2 and 3 are recorded to be 107.9 N and 108.7 N respectively at 120 krpm and 120.8 N and 120.9 N at 125 krpm (at ambient conditions of 294 K and 100 kPa). This is an improvement of 3.5 N over the 117.4 N delivered by the engine at 125 krpm with Diffuser 1. However, an improvement of 6.7 N over Diffuser 1 can be expected for Diffuser 3 when tested at the same ambient conditions of 283 K and 100 kPa at a rotational speed of 120 krpm.

The engine with Diffuser 2 produced the lowest exhaust gas temperature (EGT) at maximum thrust.

The CFD predicts the total-to-static pressure ratio for both Diffuser 2 and 3 better than the 1-D software. The 1-D analyses slightly overpredicted the total-to-static pressure ratio at the design point as seen in Figure 7.4. The reason for this can be attributed to the fact that the blade loading criterion during the design process are not within the required limits provided by Aungier (2000). Nonetheless as seen throughout the design procedure and experimental results, the 1-D CompAero software program together with the 3-D CFD Fine^{TM}/Turbo software package form a very powerful tool for designing a new centrifugal compressor. Both software programs predict the performance of a centrifugal compressor configuration relatively well and speeds up the design process by using the 1-D CompAero software program as the preliminary design process followed by a 3-D CFD analysis. The combination of these two software tools speeds up the design time and reduces manufacturing costs.

The choke and stall margins predicted by CompAero are rather conservative to ensure a proper diffuser design. Care should be taken when these limits are excessively or unnecessarily exceeded since this will result in an abrupt deterioration in compressor performance and may lead to engine failure.

It was observed that the designer should keep as close to the lower limit for the radial vaneless space as suggested by Aungier (2000) in Equation 6.1. The static pressure measured behind the impeller tip and in the diffuser throat were the highest for Diffuser 1. Diffuser 1 has the smallest radius ratio, i.e. $r_3/r_2 = 1.057$. From this observation it is clear that there exists an optimum radial vaneless space between the impeller tip and diffuser vane inlet for a specific rotational speed.

The larger geometric throat in Diffuser 1 results in a larger operating flow range with a reasonably good efficiency at the expense of static pressure recovery. It was observed that the diffusers with 30 radial vanes improve the rate of diffusion, but reduce the operating range of the compressor as seen in Figure 7.1.

The compressor map or performance graph shifts to the left when the diffuser stagger angle is smaller than the design angle, resulting in a reduced efficiency and pressure ratio for a large mass flow rate.

When considering the effectiveness and efficiency delivered by the new diffuser designs, and bearing the highly constrained radial space of the diffuser in mind, it is clear that no major improvements (when comparing results to that of the GR

180) can be expected over the compressor by only redesigning the diffuser. It can be said that for the given radial space the compressor operates near its optimum for the selected K27.2 impeller.

8.2 Recommendations

Further work can be done on the diffuser configuration by specifically focusing on the 3-D flow interaction between the impeller tip and diffuser vane leading edge to find the optimum diffuser vane geometry for the specific K27.2 impeller. The aim would be to design a diffuser vane leading edge that is sloped and machined to the exact flow angles that exit the impeller tip. This would be achievable by varying the hub-to-shroud leading edge angles as suggested by Figure 6.9, 6.10 and to a certain extent the sloped or tilted vane of Diffuser 4.

Based on the results obtained by the GR 180 micro gas turbine, (Rutten 2008), the author recommends a new centrifugal impeller design for this specific micro gas turbine. To observe major improvements over the compressor section, i.e. rotational speed, mass flow rate, static pressure recovery, the centrifugal impeller needs to be redesigned with a matching diffuser. In addition, the author also recommends investigating a mixed flow compressor, to achieve a higher mass flow rate with a high static pressure recovery, as observed for the TJ-50 (Harris et al., 2003).

Due to the small scale of the micro gas turbine and its relatively sensitive operating range, the author would recommend a diffuser with a lower solidity, i.e. decrease the number of radial vane passages, as suggested by Aungier (2000), i.e. $Z_{VD} = Z_I \mp 1$.

Since different diffuser stagger angles have a large influence on the performance of the compressor at various flow rates, the author would ultimately advise a diffuser with adjustable vanes during operation to accommodate the entire operating flow angles of the compressor from idle to maximum rotational speed; achieving better incidence over the entire flow range and not only at the design point.

LIST OF REFERENCES

Abdelwahab, A., Baker, R.L. and Gerber, G.J. (2007). Leaned Centrifugal Compressor Airfoil Diffuser, Patent Application Publiction, US 2007/0036647 A1.

Al-Mudhafar, M.M., Ilyas, M. and Bhinder, F.S. (1982). Investigation of flows in rectangular diffusers with inlet flow distortion. ASME Paper No. 82-GT-67.

Ashford, G., and Powell, K. (1996). An unstructured grid generation and adaptive solution technique for high Reynolds number compressible flows. *27th Computational Fluid Dynamics*, *VKI LS 199*, pp. 1-84.

Ashjaee, J. and Johnston, J.P. (1979). Transitory stall in diffusers, presented at the *Symposium on Flow in Primary, Non rotating Passages in Turbomachines*. ASME Winter Annual Meeting.

Au, W.C. (1991). Numerical Investigation of the Campbell Diffuser Concept, Massachusetts Institute of Technology.

Aungier, R.H. (2000). Centrifugal Compressors - A Strategy for Aerodynamic Design and Analysis, ASME PRESS. New York.

Aungier, R.H. (2009). CompAero Software User's Guide.

Aungier, R.H. (2011). Personal Communication.

Baghdadi, S., Mcdonald, A.T. (1975). Performance of Three Vaned Radial Diffusers with Swirling Transonic Flow. Journal of Fluids Engineering.

Baird, A. (2011). Personal Communication.

Bammert, K., Jansen, M. and Rautenberg, M. (1983). On the influence of the diffuser inlet shape on the performance of a centrifugal compressor stage. ASME Paper No. 83-GT-9.

Benini, E., Toffolo, A. and Lazzaretto, A. (2006). Experimental and Numerical Analyses to Enhance the Performance of a Microturbine Diffuser, Experimental Thermal and Fluid Science.

Bennett, I., Tourlidakis, A. and Elder, R.L. (2000). The Design and Analysis of Pipe Diffusers for Centrifugal Compressors. Bury St Edmonds ROYAME-UNI.

Campbell, K. (1978). Sawtoothed Diffuser, Vaned, for Centrifugal Compressors. Us patent no. 4099891.

Cengel, Y.A., Boles, M.A. (2006). *Thermodynamics,* 5th Edition. New York. McGraw-Hill.

Cumpsty, N., (1983). Compressor Aerodynamics, Longman Scientific and Technical, Essex, England.

Dean, R.C. Jr., Wright, D.D. and Runstadler, P.W. Jr. (1970). Fluid mechanics analysis of high pressure ratio centrifugal compressor data. USAAVLABS TR-69-76

Discrete Passage Diffuser, S.a, [Online], [Cited June 20th, 2010], Available from: http://www.freepatentsonline.com/6589015.html

Dixon, S. L. (1979), Fluid Mechanics and Thermodynamics of Turbomachinery,3rd Edition, Elsevier Butterworth – Heinemann.

Dixon, S. L. (2005). Fluid Mechanics and Thermodynamics of Turbomachinery,5th Edition, Elsevier Butterworth – Heinemann.

Fox, R.W. and Kline, S.J. (1960). Flow regime data and design methods for curved subsonic diffusers. Stanford University, Department of Mechanical Engineering, PD-6.

Harris, M.M., Jones, A.C. and Alexander, E.J. (2003). Miniature turbojet development at Hamilton Sundstrand, the TJ-50, TJ-120 and TJ-30 turbojets. San Diego, California: AIAA.

Higashimori, H. (2005). Diffuser for Centrifugal Compressor and Method of Producing the same, Birch Stewart Kolasch & Birch.

van Helvoirt, J. (2007). Centrifugal Compressor Surge, Modelling and Identification for Control. Technische Universiteit Eindhoven.

High Precision Flow Field Calculations, 2009, [Online], [Cited August 15th, 2010], Available from www.numexp.com/profile_eng.html

Inoue, M. and Cumpsty, N.A. (1984). Experimental Study of Centrifugal Impeller Discharge Flow in Vaneless and Vaned Diffusers. Journal of Engineering for Gas Turbine and Power 106, pp. 455.

Japikse, D. and Baines, N.C. (1998). Diffuser Design Technology, Edwards Brothers Incorporated.

Kenney, D.P. (1970). Supersonic radial diffusers. Lecture Series on Advanced Compressors, AGARD.

Kenny, D.P. (1972). A comparison of the predicted and measured performance of high pressure ratio centrifugal compressor diffusers. ASME Paper No 72-GT-54.

Krige, D.S. (2009). Performance Evaluation of a Micro Turbine Centrifugal Compressor. BEng Engineering Final Year Project. Stellenbosch University, South Africa.

Launder, B.E. and Spalding, D.B. (1974). The Numerical Computation of Turbulent Flow. Computer Methods in Applied Mechanics and Engineering, vol. 3, pp. 269-289.

Loringer, D.E., Dillen, E.R., Furman, A.H. and Swenson, K.R. (2006). *Diffuser for Centrifugal Compressor,* United States Patent. Patent No. US 7101151 B2.

Moore, A.E. (1976). Design data and guide for curved diffusing passages. Report No RR1380, British Hydromechanics Research Association, the Fluid Engineering Centre, Cranfield, UK.

Moroz, L. (2010). Centrifugal Compressor Design and Rerating in Turbochargers. SoftInWay Inc.

Numeca International. (2011a). NUMECA CFD. Retrieved from http://www.numeca.be/

Numeca International. (2011b). User Manual for IGG v8. Brussels: NUMECA International

Numeca International. (2011c). User Manual for AutoGrid5 v8. Brussels: NUMECA International

Numeca International. (2011d). User Manual for Fine/Turbo v8. Brussels: NUMECA International.

Osborne, C. (1979). Turbocharger Compressor Design and Development, Creare Science and Technology.

Osborne, C. and Japikse, D. (1982). Comprehensive evaluation of a small centrifugal compressor. Creare TN-347.

Pipe Flow Calculations, [Online], [Cited August 2011], Available from: www.pipeflowcalculations.com

Rayan, M.A. and Yang, T.T. (1980). An Investigation of Vane-Island Diffusers at high swirl. ASME.

Reneau, L., Johnston, J. and Kline, S. (1967). Performance and design of straight two-dimensional diffusers. Transaction ASME, Journal of Basic Engineering, Mar., pp. 141-150.

Roache, P. (1997). Quantification of uncertainty in computational fluid dynamics, Ann. Rev. Fluid Mech., Vol. 29, pp. 123-160.

Roberts, D.A., LeBlanc, A.D., Kacker, S.C., Townsend, P.R. and Sasu, I. (2003). *Discrete Passage Diffuser,* Pratt & Whitney Canada Corp.

Rodgers, C. (1982). The performance of centrifugal compressor channel diffusers. ASME Paper No. 82-GT-10.

le Roux, F.N (2010). The CFD simulation of an axial flow fan. MSc Engineering Thesis, Stellenbosch University.

Runstadler, P.W. Jr. (1969). Pressure recovery performance of straight channel, single-plane divergence diffusers at high Mach numbers. USAAVLABS Technical Report No. 69-56.

Runstadler, P.W. Jr. and Dolan, F.X. (1973). Further data on the pressure recovery of straight channel, plane-divergence diffusers at high subsonic Mach numbers. *Trans ASME Journ Fluids Eng 95*, pp. 373-384.

Rutten, G. (2011). Personal Communication.

Sagi, C.J. and Johnson, J.P. (1967). The Design and Performance of Two-Dimensional Curved Diffusers ASME.

Saravanamuttoo, H.I.H., Rogers, C.F.C. and Cohen, H. (2001). Gas Turbine Theory, 5th edition, Pearson Education.

Sayers, A. T. (1990). Hydraulic and compressible flow turbomachines. Cape Town, McGraw-Hill London. Retrieved from http://www.getcited.org/pub/102780284.

Shum, Y.K. (2000). Impeller-Diffuser Interaction in Centrifugal Compressors, Massachusetts Institute of Technology.

Smith, P.E.S. (1997). Theoretical Design of a Centrifugal Compressor for Use in a Miniature Gas Turbine.

Stratford, B.S., Tubbs, H. (1965). The maximum pressure rise attainable in subsonic diffusers. *Journ Royal Aero Soc* 69, pp. 275.

Sullerey, R.K., Chandra, B. and Muralidhar, V. (1983). Performance Comparison of Straight and Curved Diffusers India Institute of Technology.

Tamaki, H., Unno, M., Kawakubo, T., and Hirata, Y. (2009). Aerodynamic design to increase pressure ratio of centrifugal compressors for turbochargers. *Proceedings Of The Asme Turbo Expo 2009: Power for Land, Sea and Air*, Vol. 2175, pp. 1171-1184. Orlando, Florida. ASME.

Teipel, I. and Wiedermann, A. (1987). Three-Dimensional Flowfield Calculation of High-Loaded Centrifugal Compressor Diffusers,Journal of Engineering for Gas Turbine and Power.

Van der Merwe, B.B. (2012). Design of a Centrifugal Compressor Impeller for Micro Gas Turbine Application. MSc Engineering Thesis, Stellenbosch University.

Vaned Shroud for Centrifugal Compressor, (1994). [Online], [Cited July 29th, 2010], Available from: http://www.patentstorm.us/patents/5277541.html

Verdonk, G. (1978). Vaned diffuser inlet flow conditions for a high pressure ratio centrifugal compressor. ASME Paper No 78-GT-50.

Versteeg, H.K. and Malalasekera, W. (2007). Computational Fluid Dynamics, Second Edition. Pearson Education Limited.

de Wet, A. (2011). Performance Investigation of a Turbocharger Compressor. MSc Engineering Thesis, Stellenbosch University.

de Wet, A.L. (2011). Personal Communication.

White, F.M. (2006). Fluid Mechanics, vol. Sixth Edition. McGraw Hill.

Whitfield, A. and Baines, N.C. (1990). Design of Radial Turbomachines, Pearson Education Limited.

Wolf, S. and Johnston, J.P. (1969). Effects of non-uniform inlet velocity profiles on flow regimes and performance in two-dimensional diffusers. *Trans ASME Journ Basic Eng* 91, pp. 462-474.

Xi, G., Zhou, L., Ding, H., Yuan, M. and Zhang, C. (2007). Investigation into the Influence of Diffuser Stagger Angle on the Flow Field and Performance of a Centrifugal Compressor, Front Energy Power Eng. China.

Ziegler, K.U., Gallus, H.E., Niehaus, R. (2003). A Study on Impeller-Diffuser Interaction ASME.

APPENDIX A: NUMERICAL ANALYSIS

A detailed description of the 1-D and 3-D CFD software package environments, as well as the modelling criteria of each program, is included in this Appendix.

A.1 Review of the 1-D Software Package

Aungier's (2000) one-dimensional centrifugal compressor software program, CompAero, is used to perform the 1-D analyses. CompAero is an aerodynamic design and analysis software system for centrifugal and axial flow compressors (Aungier, 2009) based on the theory of Aungier (2000). It uses basic thermodynamic and fluid dynamic principles, empirical models and key numerical methods to execute computations along a mean stream surface through each of the compressor stage components.

CompAero has a variety of programs to use for compressor design, however only the CENCOM (**CEN**trifugal **COM**pressor) and VDDESIGN (**V**aned **D**iffuser **DESIGN**) programs were of interest for this thesis.

A.1.1 Overview of CENCOM

CENCOM can be used for the "*mean-line aerodynamic performance analysis for single- or multi-stage centrifugal compressors*" (Aungier, 2009). The program uses the procedures as described in Chapter 5 of Aungier (2000). CENCOM collects and saves performance prediction results and uses them to display various performance maps for the compressor as well as the performance of each stage.

All compressor geometries, i.e. impeller, vaneless space and radial vaned diffuser, are specified in CENCOM as well as the initial flow conditions as discussed below.

a) Inlet flow and rotational speed data

The inlet flow, total pressure, total temperature, swirl and rotational speed parameters are required for a specific compressor test case. There are however alternate options for three of the input parameters that can be selected. The options are, (Aungier, 2009):

- Inlet swirl: mass flow, volume flow or flow coefficient (φ).
- Swirl parameter: absolute tangential velocity or absolute flow angle with respect to the tangent, on the mean streamline at the inlet of the first component.
- Rotational speed: rotational speed, rotational Mach number (tip speed/inlet total sound speed), equivalent tip speed or actual tip speed.

The three parameters used for the compressor analysis in this thesis are mass flow rate ($\dot{m}$), absolute tangential velocity (C_U) and rotational speed (N). CompAero allows the user to specify 8 points for a specific compressor operating range at which performance computations are executed.

b) Impeller geometry input data

The impeller geometry is based on conditions at the mean stream surface as indicated in Figure 2.2. The mean stream surface divides the annulus into two equal areas. It is typically defined by the root-mean-square (rms) of the hub and shroud radii (Aungier, 2009). The required values on the mean stream surface are at the impeller leading edge, a mid-passage location (typically the throat) and trailing edge locations. The blade angles are measured relative to the tangential direction in the relevant stream surface.

Impeller diameters at the impeller leading and trailing edge are required on the hub and shroud contours as well as the relevant passage widths, blade thicknesses, the blade-shroud clearance gaps, mean stream surface cone angles (α_C) and the throat area. The required throat area (A_{th}) is computed in SolidWorks (a CAD software program). The KKK K27.2 impeller geometry required for the 1-D modelling is supplied in Table E.1.

c) Vaneless diffuser/vaneless passage input data

Similar to the impeller input data, the vaneless passage input data is also based on conditions at the mean stream surface. A minimum of three equally spaced stations along the length of the passage are required for the analysis. The respective axial and radial coordinates as well as hub-to-shroud-widths are specified at each station and a flow path is generated by the program's mean of interpolation. The vaneless passage geometry for Diffuser 1 (original BMT 120 KS diffuser), specified in CENCOM, is supplied in Table A.1.

Table A.1: Vaneless passage geometry used in CENCOM

r $[mm]$	b $[mm]$
35	6
36	6
37	6

d) Vaned diffuser input data

It should be mentioned that Aungier (2000) details the 1-D performance analysis for conventional thin-vaned or airfoil style vaned diffusers. He however mentions that during occasional use for vane-island type diffusers (thick vaned diffusers) the analysis gave reasonable results.

Again the vaned diffuser follows the mean stream surface. The input data required are indicated in Figure 2.7, including the leading and trailing edge radii (r_3, r_4), the passage inlet and outlet depths (b_3, b_4), blade angles (β_3, β_4) and throat width (h_{th}). Additional parameters required by VDDESIGN include the number of diffuser vanes, leading and trailing edge vane thicknesses and the vane mean camberline at a location mid-way along the vane. Table E.2 includes the geometry for Diffuser 1 (original BMT 120 KS diffuser).

CompAero does not allow the user to specify data output points along the vane camberline and only outputs the vane inlet and discharge conditions. The radial diffuser discharge is therefore placed at a radius of 45 mm in CompAero to predict results at this location since the experimental data is measured at this radius.

e) Gas model

Various ideal and non-ideal fluid equation-of-state models are available in CENCOM namely:

- Aungier's modified Redlich-Kwong equation of state
- Original Redlich-Kwong equation of state
- Ideal (thermally perfect) gas equation of state
- Pseudo-perfect gas equation of state

The thermally perfect gas equation of state is used as the thermodynamic model. The ideal/non-ideal gas database uses a catalog of various gas properties to set up gas or gas mixture equations of state (Aungier, 2009).

A.1.1 Overview of VDDESIGN

VDDESIGN is a "*vaned diffuser detailed aerodynamic design, performance analysis and blade-to-blade flow analysis program*" (Aungier, 2009). The program uses the approach as described in Chapter 9 of Aungier (2000).

VDDESIGN forms part of the new diffuser design procedure. It has the option to perform design point or off-design performance analyses as well as blade-to-blade flow analyses for direct evaluation of the blade loading.

The flow chart of the design procedure followed in VDDESIGN is shown in Figure A.1. The vaned diffuser design and analysis is accomplished in a single design system in an iterative fashion as indicated in the flow chart.

The vaned diffuser inlet, component sizing techniques and vane design are processed in an interactive fashion. CompAero allows the user to export the relative vane design geometry in VDDESIGN to CENCOM to execute the overall compressor performance analyses over each stage. The impeller tip geometry and flow conditions are required by VDDESIGN to design a proper diffuser for the particular impeller configuration.

a) Vaned diffuser component sizing

Various important design parameters are specified in this section of VDDESIGN that determine the final diffuser design and its design point performance. These parameters will briefly be discussed in the following section. An in-depth discussion follows in Chapter 5. VDDESIGN requires the following input parameters: diffuser inlet radius (r_3), inlet passage depth (b_3), inlet blade angle (β_3), diffuser discharge radius (r_4), discharge passage depth (b_4), discharge blade angle (β_4), the average vane surface finish and the number of diffuser vanes to perform an analysis.

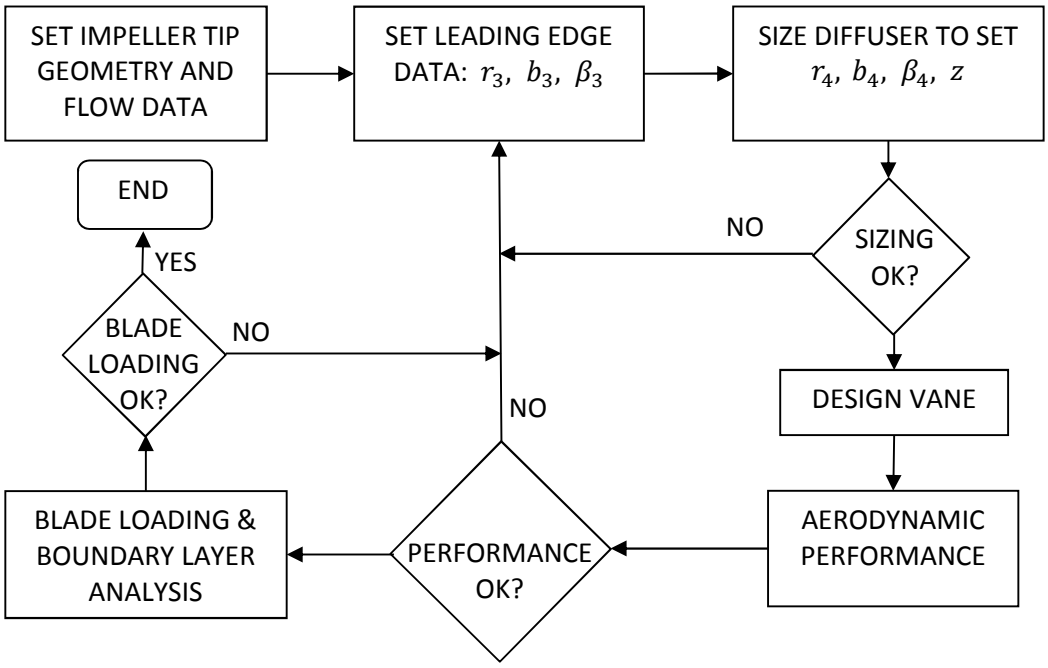

Figure A.1: Flow chart of the design procedure in VDDESIGN

One of the following vaned diffuser sizing parameters can be constrained during the design procedure:

- Discharge blade angle (β_4).
- Divergence angle ($2\theta_C$).
- Area Ratio (A_R).

Aungier (2000) recommends the following values for the vaned diffuser design parameters:

- Equivalent Divergence Angle ($2\theta_C$): 10 to 11 degrees (when vane data have been supplied an effective divergence value is also listed, which corrects for vane thickness and passage width variations; this is more relevant in many cases).
- Blade loading parameter (*L*): 0.3 to 1/3.
- Area Ratio (A_R): approximately 2.4.
- Vane Inlet Radius / Impeller Tip Radius (r_3/r_2): 1.06 to 1.12

These are preferred values and as mentioned before have been investigated and qualified for conventional thin-vaned or airfoil type vaned diffusers. The first two parameters should be as close to their maximums as possible, but not exceed the maximum value (Aungier, 2009). Aungier observed an abrubt deterioration in vaned diffuser performance when $L > \frac{1}{3}$ or when $2\theta_C > 11°$. However Aungier (2011) mentions that for thick-vaned diffusers the divergence angle is slightly less than the value indicated above. With regard to the fourth parameter, it should be

attempted to keep the value as close to the lower limit as possible while still maintaining reasonable vane inlet Mach number levels, (Aungier, 2009).

Low inlet blade angles are desirable to achieve a wide stall free operating range, where angles around 18˚ are usually a good choice, if impeller matching constraints permit (Aungier, 2009). Similarly, a small number of vanes will benefit a wider operating range. Aungier recommends between 12 and 16 vanes where design constraints permit.

A.2. Review of the CFD Software Package

FINE™/Turbo v8.9-1 by NUMECA™ International (Intl.) is the CFD software used in this thesis. Three separate software systems are used in FINE™/Turbo for the CFD analysis as follows:

4. The *pre-processor* is a combination or integration of two separate programs, namely **I**nteractive **G**eometry modeller and **G**rid generator (IGG™) and **Auto**mated **Grid** generator (AutoGrid5™).
5. The *solver* system in FINE™/Turbo uses EURANUS™ (**EUR**opean **A**erodynamic **N**umerical **S**imulator) to solve computations.
6. The *post-processor* is a Computational Field Visualisation software program known as CFView™.

All three systems have been integrated into one package by NUMECA Intl. called **F**low **IN**tegrated **E**nvironment (FINE™/Turbo). The three systems mentioned above will be discussed in the following section.

A.2.1 Overview of NUMECA FINE™/Turbo

This section briefly describes the capabilities and functions of the NUMECA FINE™/Turbo CFD environment used in the design and investigation of the BMT 120 gas turbine.

IGG™ is a program designed to create arbitrary shapes and multi-block structured grids on 2-D or 3-D geometries (Numeca International, 2011b). All the required CFD models are created in Solidworks, a Computer Aided Design (CAD) program and exported to AutoGrid5™ in a **.geomTurbo* file format. This replaces the use of IGG™, for geometric modelling of the compressor, since AutoGrid5™ generates its own **.igg* file from the imported CAD geometries. However IGG™ is still used to connect full non matching planes between stator-stator interfaces, e.g. connecting the interfaces between the radial and axial diffuser vanes. This is discussed further in Section 3.3.4.

AutoGrid5™ is an automatic hexahedral grid generating program that produces complex structured meshes for axial and centrifugal turbomachinery components. It involves the "*geometrical description of the studied model and the discretization (mesh generation) of the studied domain*", (Numeca International, 2011c). The method that AutoGrid5™ uses to create 3-D meshes is based on conformal mapping between the 2-D cylindrical blade-to-blade surfaces in the dm/r-θ plane and the 3-D cartesian coordinate system. Surfaces of revolution, i.e. hub and shroud, are projected onto the meridional plane (*r-z*) to create spanwise (hub-to-

shroud) streamlines. The 2-D blade-to-blade mesh generation allows control of the mesh topology prior to a lengthy 3-D mesh generation.

A large limitation on CFD simulations is the computational time required for a fine mesh to reach convergence. Accordingly, the least amount of vanes required to represent the full mesh is used in all three compressor stages to reduce the computational time. Various parameters can be adjusted in AutoGrid5™ to set the rotational periodicity required to execute the entire compressor mesh. AutoGrid5™ has a number of internal features that help to recreate the actual geometry or component accurately, such as hub and shroud clearance gaps, splitter blades and sharp or rounded treatment at the leading edge, to mention a few.

FINE™/Turbo is executed by the flow solver EURANUS. EURANUS is a "*3-D multiblock flow solver able to simulate Euler or Navier-Stokes (laminar or turbulent) flows*" (Numeca International, 2011d). It involves the setting up of a flow field with its respective turbulence models and boundary conditions by solving a set of discretized equations for either steady or unsteady flow models. FINE™/Turbo is also used to define multiple computations with different solver setups from the same IGG™ or AutoGrid5™ CGNS model. The residual convergence throughout solving a set of discretized equations can be viewed by using NUMECA's Monitor™ interface.

CFView™ is an interactive visualization program that displays the solved flow domain results. Various outputs accustomed to turbomachinery terminology, executed in FINE™/Turbo, can be represented in CFView™ by local values, vector averages, weighted integrals, isolines, streamlines or contour plots.

A.2.2 Mesh Quality and Convergence

AutoGrid5™ has numerous features to evaluate the mesh quality during the 2-D blade-to-blade (B2B) meshing process from hub to shroud. Three distinctive AutoGrid5™ parameters that adequately represent the quality of the mesh are checked after every B2B generation, namely the mesh orthogonality (skewness), aspect ratio and expansion ratio. These parameters are described below:

- The orthogonality represents the 'skewness' of each control volume (CV) in a 2-D plane, more specifically it is a measure of the angle between the edges of an element (Numeca International, 2011c). The smaller the angle, the lower the quality of the mesh. The angle varies between 0˚ and 90˚.
- The aspect ratio is a measure of how thin and long a CV is in a 2-D plane. It is defined as the ratio between the maximum averages of opposite lengths over the shortest average of opposite lengths of a CV.
- The expansion ratio is a measure of the size variation in a specific direction between two adjacent cells in 3-D.

The author aimed to achieve a grid orthogonality greater than *24˚*, an aspect ratio lower than *2000* and an expansion ratio of less than *2.5*. In addition the angular variation between adjacent cells are also monitored and checked to be below *40˚* at all times. This is known as the angular deviation.

The mesh quality of each stage of the compressor, i.e. impeller, radial vanes and axial blades, can be adjusted and improved individually in AutoGrid5™. One means of improving the mesh quality is to adjust the selected stage topology. Three predefined B2B topologies exist in AutoGrid5™ for a centrifugal compressor, namely: default (O4H) topology, HOH topology and H&I topology. The default (O4H) topology consists of 5 control blocks as follows (indicated in Figure 3.2):

1. O-block, around the blade called the *skin block*
2. H-block-upstream, upstream of the blade called the *inlet block*
3. H-block-downstream, downstream of the blade called the *outlet block*
4. H-block up, above the blade section called the *up block*
5. H-block down, below the blade section called the *down block*

The HOH topology consists of three blocks that define the B2B mesh, i.e. *inlet block*, *O-block* and the *outlet block*. The O-block is typically used to enhance the control of the boundary layers on the blade surfaces. The HOH topology is used to obtain high grid quality, but does however have some limitations, e.g, it cannot be applied to a row with splitter blades, (Numeca International, 2011c). H&I topology is used to obtain better mesh quality with multiblades, i.e. in the case where splitter blades are present. The number of nodes in these blocks can be adjusted to improve the quality of the mesh. Care should be taken when adjusting the number of nodes of each block since AutoGrid5™ creates multiple mesh levels from these parameters, known as multigrids. Multigrids allow for quick convergence of simulations on coarser grids and the converged solutions are then used to initialize finer grids. This process is known as *Course Grid Initialisation* and is further discussed in Section 3.4.5.

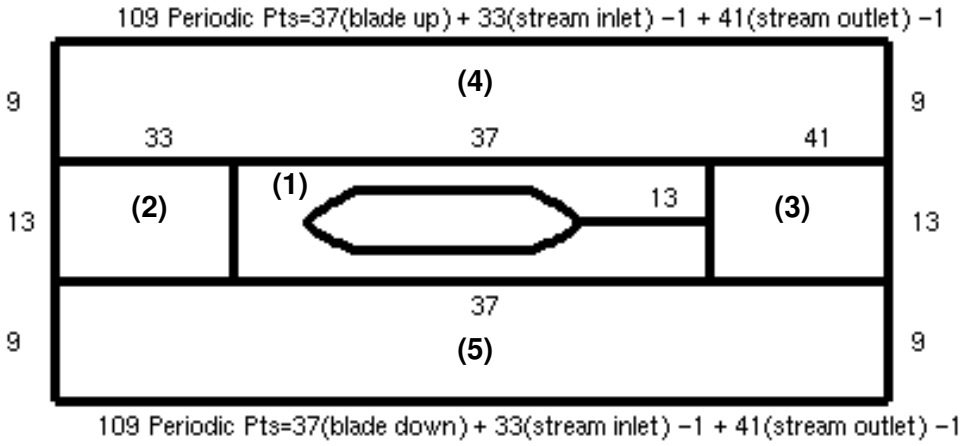

Figure A.2: Blade topology in AutoGrid5™

A 3-D mesh is generated once all mesh properties are appropriately or satisfactorily adjusted. This is achieved by generating blade-to-blade meshes on streamlines in the meridional plane. The span interpolation is set to 2% by

default. This option allows the user to determine the size of the optimized blade-to-blade mesh increments from hub to shroud, and can be adjusted as required. Before exiting AutoGrid5™ a check for negative cells is performed. The mesh quality criteria are indicated for each mesh stage in its respective section in Chapter 3.

A.2.3 Turbulence Modelling

FINE™/Turbo makes use of three mathematical models to model the flow state in the discretized domain, (Numeca International, 2011d). The models are as follows:

- The Euler model.
- The Laminar Navier-Stokes model.
- The Turbulent Navier-Stokes model.

Several turbulence models are supplied by FINE™/Turbo such as, the algebraic Baldwin and Lomax (1978) model, the Spalart-Allmaras (1992) model, and variations of the k-ε, k-ω and v^2-f models, (Numeca International, 2011d). The turbulence model determines how well the simulation approximates the solid surface boundary layers. This is evaluated by computing the y^+ parameter for the model in FINE™/Turbo. The y^+ parameter is defined by Equation A.1.

$$y^+ = \frac{\rho u_\tau y_{wall}}{\mu} \tag{A.1}$$

with y_{wall} being the height of the grid node near the wall. The friction velocity, u_τ, is defined by Equation A.2.

$$u_\tau = \sqrt{0.5 \cdot V_{ref}^2 \cdot C_f} \tag{A.2}$$

where V_{ref} is the reference velocity and C_f the shear coefficient.

For low-Re models NUMECA Intl. (2011d) suggests an acceptable y^+ range between 0 and 10, depending on the turbulence model used. This region is referred to as the viscous sub-layer. White (2006) defines the viscous sub-layer as $y^+ \leq 5$. It is good practice to evaluate the y^+ value on all surfaces after a computation to determine whether the grid near the walls is well defined. The y^+ value can be changed by adjusting the height (y_{wall}) of the grid nodes near the solid walls. The y^+ value is also dependent on the velocity component (u_τ) and it is therefore necessary to evaluate the y^+ value at the highest mass flow rate computation.

De Wet (2011) investigated two turbulent models namely the Spalart-Allmaras (1992), (S-A) model and the standard *k-ε* with extended wall function model by Launder and Spalding (1974) on identical meshes of the Eckardt O-Rotor, to justify the decision to use a single turbulence model throughout his study. De Wet (2011) found satisfactory convergence for both turbulence models, however a distinct reduction in convergence time for the S-A model was observed and it

required much less memory usage during computation. It was therefore decided to use the S-A turbulence model throughout this thesis. The author aimed at achieving y^+ values less than 10 for this thesis. It should also be mentioned that an overshoot of this value can be expected on surfaces where a high degree of separation may occur, for example at the impeller tip.

APPENDIX B: AIR PROPERTIES, CHARACTERISTICS AND SAMPLE CALCULATIONS

Various sample calculations are provided in this Appendix to illustrate how the experimental compressor performance characteristics were determined from the measured data, as well as certain air properties and characteristics.

B.1 Air properties

The ambient pressure and temperature used to validate the numerical results were measured to be $p_{t,amb} = 100\,kPa$ and $T_{t,amb} = 283\,K$ in the test facility, resulting in a density of, $\rho_{t,amb} = 1.23\,kg/m^3$. The well-known perfect gas equation of state (Equation B.1) is used to determine the initial gas density:

$$\rho = \frac{P}{RT} \tag{B.1}$$

The gas mixture used in the thermodynamic equation of state in CompAero is 100% air with the following properties:

Table B.1: Summary of the thermodynamic gas properties

Parameter	Units	Value
Molecular weight	[kg.kmol]	28.96
Critical temperature	[K]	131.76
Critical pressure	[kPa]	3685.39
Critical compressibility factor	[-]	0.2896
Acentric factor	[-]	0.0357

The specific heat at constant pressure (C_p) used in CompAero is determined from the following formula (Aungier, 2009):

$$C_p = 1.050 + (-3.6506 \cdot 10^{-4} + (8.4823 \cdot 10^{-7} + -3.9184 \cdot 10^{-10} \cdot T) \cdot T) \cdot T \tag{B.2}$$

B.2 Sample calculations

The mass flow rate through the engine is determined by measuring the pressure drop between the inlet bell-mouth and the atmosphere. The mass flow rate at 120 krpm is calculated as follows, where C_d (Equation B.4) is the discharge flow coefficient and β is d_2/d_1:

$$\dot{m} = \rho_{duct} C_d A_{duct} \left[\frac{2\Delta p/\rho_{duct}}{1-\beta^4}\right]^{1/2} \quad \text{B.3}$$

$$\dot{m} = 1.2 \cdot 0.988 \cdot \pi \cdot 0.051^2 \sqrt{\frac{2 \cdot 520/1.2}{1-0.364^4}}$$

$$\dot{m} = 0.288\ kg/s$$

$$C_d = 0.9965 - 0.00653\sqrt{\frac{1 \cdot 10^6 \cdot \beta}{Re_D}} \quad \text{B.4}$$

$$Re_D = \frac{V_2 d_2}{\nu} \quad \text{B.5}$$

The density in the inlet duct is calculated to be 1.2 kg/m^3 due to the drop in total pressure in the inlet duct. The discharge flow coefficient is calculated to be 0.988.

The total temperature and pressure in Equation B.6 is determined iteratively from the static measurements by means of isentropic relationships.

$$\frac{p_4}{p_{t,4}} = \left(\frac{T_4}{T_{t,4}}\right)^{\frac{\gamma}{\gamma-1}} \quad \text{B.6}$$

The total temperature and pressure at the diffuser discharge of the original BMT 120 KS compressor assembly (with Diffuser 1) amounted to $T_{t,4} = 410.16\ K$ and $p_{t,4} = 315.4\ kPa$ respectively.

The total temperature and pressure at the compressor inlet and discharge were used to compute the total-total isentropic efficiency over the compressor (Equation B.7) and total-to-total pressure ratio (Equation B.8). The isentropic efficiency over the diffuser is calculated using Equation B.9.

$$\eta_{TT,0-4} = T_{t,0}\left[\left(\frac{p_{t,4}}{p_{t,0}}\right)^{\frac{\gamma-1}{\gamma}} - 1\right] \Big/ \left(T_{t,4} - T_{t,0}\right) \quad \text{B.7}$$

$$PR_{TT,0-4} = \frac{p_{t,4}}{p_{t,0}} \quad \text{B.8}$$

$$\eta_D = T_2\left[\left(\frac{p_3}{p_2}\right)^{\frac{\gamma-1}{\gamma}} - 1\right] \Big/ \left(T_3 - T_2\right) \quad \text{B.9}$$

The Mach number in the inlet duct is calculated to determine whether the flow should be treated as compressible or incompressible upstream of the impeller inlet. The velocity component through the inlet duct (C_{duct}) is initially determined by measuring the static pressure difference (Δp) between the bell-mouth and the ambient pressure, and solving for the velocity component in Equation B.10.

$$\Delta p = \frac{1}{2}\rho C_{duct}^2 \quad \text{B.10}$$

The static temperature in the duct (T_{duct}) is determined by Equation B.11 and the Mach number follows for adiabatic flow in Equation B.12.

$$T_{duct} = T_{t,duct} - \frac{C_{duct}^2}{2 \cdot C_p} \quad \text{B.11}$$

$$M_{duct} = \sqrt{\left(\frac{T_{t,duct}}{T_{duct}} - 1\right) / \left(\frac{\gamma - 1}{2}\right)} \quad \text{B.12}$$

The value for $T_{t,duct}$ is taken as T_{amb}.

B.3 Critical values at the sonic point

Aerodynamic choking is evaluated in both the impeller and diffuser throat and will occur when the relative Mach number in the impeller and the absolute Mach number in the diffuser equals 1 ($Ma = 1$), i.e. at sonic conditions. Aungier (2000) predicts impeller and diffuser choke when the aerodynamic throat area is smaller than the required area for a sonic velocity at a specific mass flow rate. The sonic flow area is determined as follows (Aungier, 2000):

$$A^* = \frac{\dot{m}}{\rho^* V^*} \quad \text{B.13}$$

The critical density (ρ^*), temperature (T^*) and velocity (V^*) are based on the total thermodynamic conditions and is determined by Equations B.14 through B.16 (White, 2006).

$$\rho^* = \rho_t \left(\frac{2}{\gamma + 1}\right)^{1/(\gamma - 1)} \quad \text{B.14}$$

$$T^* = T_t \left(\frac{2}{\gamma + 1}\right) \quad \text{B.15}$$

$$V^* = a^* = \sqrt{\gamma R T^*} \quad \text{B.16}$$

$$= \sqrt{\frac{2\gamma}{\gamma + 1} R T_t}$$

APPENDIX C: 1-D MEAN STREAM SURFACE CALCULATIONS

Calculations performed on the mean stream surface in CompAero are illustrated in this Appendix. Only a selected few equations for the vaneless annular passage and vaned diffuser are illustrated. For further information and detailed explanations on the theory used in CompAero see Aungier (2000) and (2009).

C.1 Vaneless passage sizing

The size of the vaneless annular passage may be determined as follows, with reference to Figure 2.5. At any given radius *r* the mass flow rate is given by

$$\dot{m} = \rho A C_r = 2\pi r b \rho C_r \qquad \text{C.1.1}$$

where *b* is the width of the vaneless annular passage perpendicular to the peripheral area of the impeller and is usually the same as the impeller width (Sayers, 1990). Now from continuity

$$r b \rho C_r = r_2 b_2 \rho_2 C_{r2} \qquad \text{C.1.2}$$

where the unsubscripted variables represent conditions at any radius *r* in the vaneless annular passage. By the conservation of angular momentum and assuming frictionless flow, the tangential velocity C_U is given by

$$C_U = C_{U2} r_2 / r \qquad \text{C.1.3}$$

The absolute velocity C is approximately equal to the tangential velocity C_U since the tangential velocity is usually much larger than C_r (Sayers, 1990). Therefore the absolute velocity can be approximated as

$$C = C_{U2} r_2 / r \qquad \text{C.1.4}$$

To obtain a large reduction in kinetic energy the absolute velocity component needs to be as small as possible. This requires *r* to be large and therefore results in a vaneless space with a large radius, (Sayers, 1990). However, the vaneless space criteria (Equation 5.1) supplied by Aungier (2000) was used to achieve the best possible size for the vaneless space.

C.2 Vaneless passage performance

The total thermodynamic conditions at the diffuser leading edge such as the mass flow rate and angular momentum are determined from the upstream impeller conditions. The vaneless annular passage analysis in CENCOM is evaluated by integrating Equations C.2.1 through C.2.4 along the passage length, subject to auxillary relations as presented in Chapter 5 of Aungier (2000). The governing equations for one dimensional flow along a mean stream surface in a vaneless annular passage are indicated below (Aungier, 2000):

$$\dot{m} = 2\pi r \rho b C_m (1 - B) \quad \text{C.2.1}$$

$$b C_m \frac{d(rC_U)}{dm} = -rCC_U c_f \quad \text{C.2.2}$$

$$\frac{1}{\rho}\frac{dp}{dm} = \frac{C_U^2 sin\alpha_C}{r} - C_m \frac{dC_m}{dm} - \frac{CC_m c_f}{b} - \frac{dI_D}{dm} - I_C \quad \text{C.2.3}$$

$$h_t = h + \frac{1}{2}C^2 \quad \text{C.2.4}$$

The last two terms in Equation C.2.3 address loss contributions due to flow diffusion (I_D) and passage curvature (I_C). The maximum, stall-free, local area at each computing station is estimated by Equation C.2.5 which is equivalent to a diffuser divergence angle ($2\theta_C$) of 9˚.

$$(rb)_m = (rb)_1 \left[1 + \frac{0.16m}{b_1}\right] \quad \text{C.2.5}$$

Aungier (2000) uses a simple boundary layer growth model based on a 1/7th power law for velocity profiles (Equations C.2.6 and C.2.7) in the boundary layer to compute the area blockage and skin friction coefficients.

$$C_m = C_{me}\left(\frac{y}{\delta}\right)^{\frac{1}{7}} \quad \text{C.2.6}$$

$$C_U = C_{Ue}\left(\frac{y}{\delta}\right)^{\frac{1}{7}} \quad \text{C.2.7}$$

Subscript *e* refers to a value at the boundary layer edge. If the boundary layers are identical and the boundary layer thickness (δ in Equation C.3.15) is known an expression for the area blockage (B), Equation C.2.9 as a function of $2\delta/b$ can be determined by integrating across the passage for mass flow in Equation C.2.8.

$$\int_0^b \rho C_m dy = \rho b C_{me}\left[1 - \frac{2\delta}{8b}\right] = \rho b C_{me}(1 - B) \quad \text{C.2.8}$$

$$B = \frac{2\delta}{8b} \quad \text{C.2.9}$$

In a similar fashion the average angular momentum flux can be determined by integrating Equation C.2.10. Equation C.2.11 relates the predicted angular momentum to the boundary layer edge value.

$$\int_0^b \rho C_m C_U dy = \rho b C_{me} C_{Ue}\left[1 - \frac{2\delta}{4.5b}\right] \quad \text{C.2.10}$$

$$rC_U = rC_{Ue}\left[1 - \frac{2\delta}{4.5b}\right] \quad \text{C.2.11}$$

Equation C.2.9 and C.2.11 provide means for calculating the boundary layer growth to yield local values of δ and B, where the limit $2\delta \leq b$ must be imposed, (Aungier, 2000).

C.3 Radial vaned diffuser performance

Flow calculations are performed at three locations along the diffuser vane passages, namely the leading edge (*3*), throat (*th*) and trailing edge (*4*). The total thermodynamic conditions, mass flow rate and angular momentum at the diffuser leading edge are determined from the upstream components (Aungier, 2000) in CENCOM. Therefore the vaneless space discharge conditions are used for the radial diffuser inlet conditions. Note that CompAero evaluates flow criteria in the diffuser throat, i.e. A_{th}/A^*, but does not supply the user with pressure and temperature predictions in the diffuser throat and can therefore not be used to validate CompAero against the experimental throat measurements.

C.3.1 Diffuser Choke

The viscous area blockage in the vane throat is estimated as a throat contraction ratio given by

$$c_r = \sqrt{\frac{A_3 sin\beta_3}{A_{th}}} \tag{C.3.1}$$

The sonic flow area is given by Equation B.13. Aungier (2000) predicts choke in the vaned diffuser when the effective throat area ($c_r A_{th}$) is equal to the sonic flow area (A^*), i.e. $A^* = c_r A_{th}$.

C.3.2 Diffuser Stall

Aungier (2000) supplied the following criterion that approximates stall in vaned diffusers:

$$K + K_0 = 0.39 \tag{C.3.2}$$

The vaned diffuser stall parameter (K), Equation C.3.3, is evaluated between the diffuser inlet and throat, whereby an average value between the inlet and throat is used.

$$K = \frac{r_3}{h_{th}}\left[\frac{cos\alpha_3}{cos\alpha_{th}} - 1\right] \tag{C.3.3}$$

α_{th} in Equation C.3.3 is given by

$$sin\alpha_{th} = \frac{A_{th}}{A_3} \tag{C.3.4}$$

The Mach number is significant for the onset of vaned diffuser stall resulting in the following expression for K_0 in Equation C.3.2:

$$K_0 = \frac{M_3^2 sin^2\beta_3 cos\beta_3}{1 - M_3^2 sin^2\beta_3} \tag{C.3.5}$$

C.3.3 Radial vaned diffuser performance criteria

The optimum or minimum loss incidence angle is defined as

$$sin\alpha_3^* = \frac{C_{m3}}{C_3^*} = \sqrt{sin\beta_3 sin\alpha_{th}} \tag{C.3.6}$$

The diffuser divergence angle and the blade loading parameter is defined as

$$2\theta_C = 2tan^{-1}\left\{\left[\frac{(w_4 - t_{b4})b_4}{b_3} - w_3 + t_{b3}\right]/2\,L_B\right\} \tag{C.3.7}$$

$$L = \frac{\Delta C}{C_3 - C_4} \tag{C.3.8}$$

Where $w = (2\pi r sin\beta)/z$ in Equation C.3.7 and the average blade-to-blade velocity difference is defined by Aungier (2000) as

$$\Delta C = 2\pi \frac{r_3 C_{U3} - r_4 C_{U4}}{z_D L_B} \tag{C.3.9}$$

The discharge area blockage is defined as

$$B_4 = \frac{K_1 + K_2(\bar{C}_R^2 - 1)L_B}{w_4} \tag{C.3.10}$$

where $\bar{C}_R$, K_1 and K_2 are defined below

$$\bar{C}_R = \frac{1}{2}\left[\frac{C_{m3} sin\beta_4}{C_{m4} sin\beta_3} + 1\right] \tag{C.3.11}$$

$$K_1 = 0.2\left[1 - \frac{1}{C_L C_\theta}\right] \tag{C.3.12}$$

$$K_2 = \frac{2\theta_C}{125 C_\theta}\left[1 - \frac{2\theta_C}{22 C_\theta}\right] \tag{C.3.13}$$

The vaned diffuser discharge total pressure is given by

$$p_{t,4} = p_{t,3} - (p_{t,3} - p_3)\sum_i \bar{\omega}_i \tag{C.3.14}$$

where $\bar{\omega}_i$ is the total pressure loss coefficient.

The boundary layer thickness in the vaned diffuser is determined by a simple flat plate boundary layer approximation estimated at the midpassage (Aungier, 2000), as shown in Equation C.3.15.

$$\delta = \frac{5.142}{2} c_f L_B \qquad \text{C.3.15}$$

APPENDIX D: AUTOGRID MESH CRITERIA AND NUMERICAL DATA

The numerical data obtained for each diffuser as well as the AutoGrid5™ meshes and mesh quality criteria of each compressor configuration are included in this Appendix. The mesh setup and criteria of the original compressor assembly (with Diffuser 1) is included in Chapter 3; Diffusers 2, 3 and 4 are therefore summarized here. Also note that all the compressor models use the exact same impeller. The impeller meshes differ slightly at the trailing edge due to the different vaned diffuser meshes that need to match that of the impeller in AutoGrid5™. The complete impeller meshes are therefore not discussed here, only the quality criterion of each impeller mesh is given for each case. All diffuser meshes have the same inlet and outlet boundary conditions as described in Section 3.4.4 and are not included here for each diffuser. The visual results for the vane leading edge geometry (Section 6.5.2) and absolute Mach numbers in the diffuser throat provided by CFView™ are also provided in this Appendix.

D.1. NUMECA Fine™/Turbo overview and AutoGrid5™ mesh criteria

The following section describes the mesh layout and criteria of each diffuser configuration modelled in the CFD analysis. Indicated in Figure D.1 is a screenshot of the AutoGrid5™ user interface.

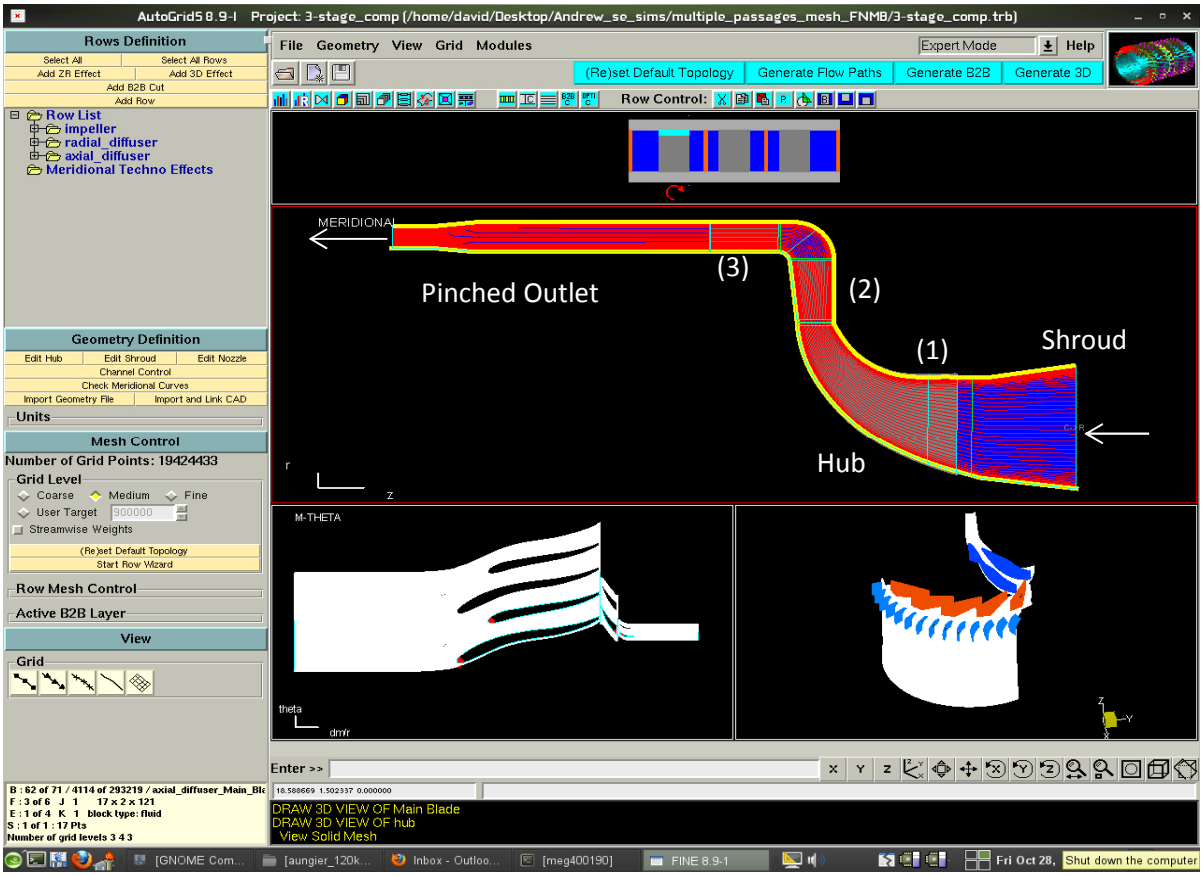

Figure D.1: Screenshot of AutoGrid5™

Figure D.2 indicate the mesh layout for a pair of main- and splitter- blades of the centrifugal impeller and Figures D.3 and D.4 indicate the mesh layout for the radial diffuser vanes and axial blades respectively. Figure D.5 indicate the combined compressor mesh as modelled in AutoGrid5™.

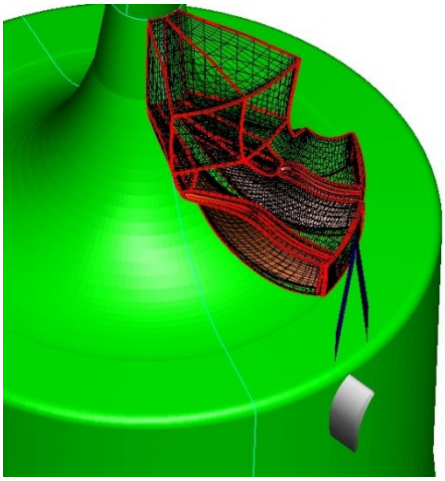

Figure D.2: Screenshot of the impeller mesh in AutoGrid5™ with a coarse (222) grid level

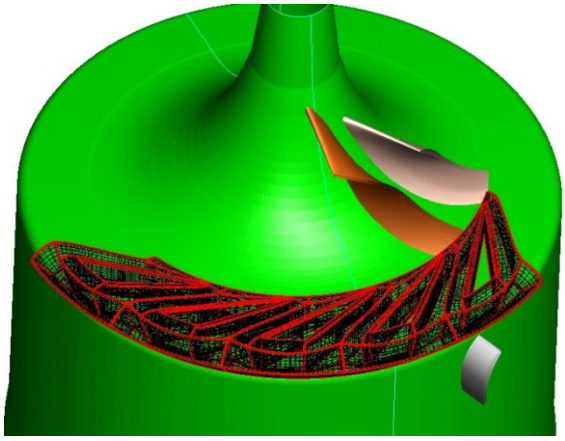

Figure D.3: Screenshot of the radial diffuser mesh in AutoGrid5™ with a coarse (222) grid level

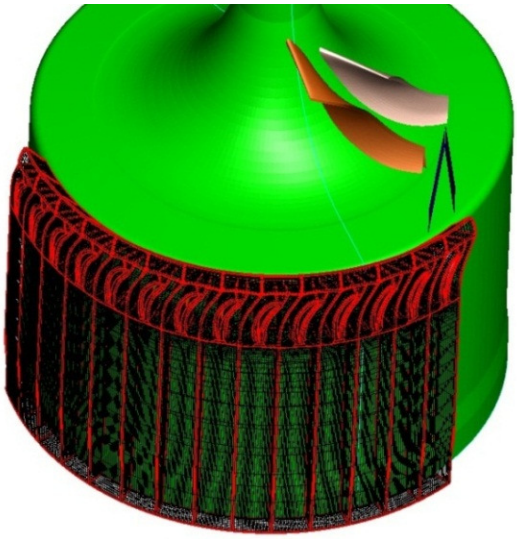

Figure D.4: Screenshot of the axial blade mesh in AutoGrid5™ with a coarse (222) grid level

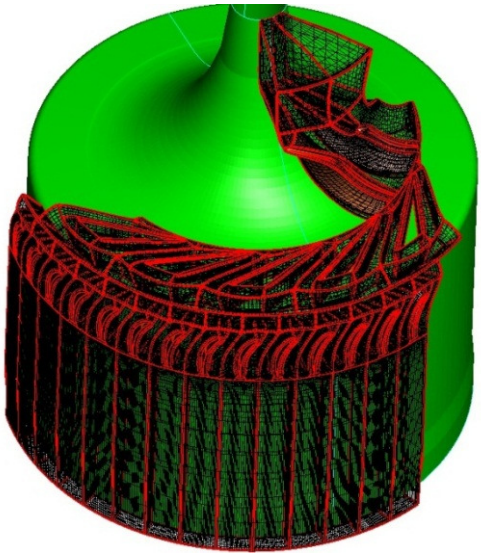

Figure D.5: Screenshot of the combined compressor mesh in AutoGrid5™ with a coarse (222) grid level

D.2. Diffuser 2 compressor mesh

The impeller mesh consists of 2333952 grid points with the following mesh quality criteria:

Table D.1: Impeller mesh quality criteria

	Mesh quality criteria	Impeller Mesh
Orthogonality	> 24˚	26.81˚
Aspect Ratio	< 2000	213.38
Expansion Ratio	< 2.5	2.53
Angular Deviation	< 40˚	13.13˚

Diffuser 2 consists of 30 radial vanes with 30 downstream axial blades. Only the radial vane and axial blade hub and shroud geometries are required by AutoGrid5^{TM} since both geometries are relatively simple. The mesh for Diffuser 2 is created with 57 flow paths from hub to shroud on the surfaces of revolution. The *default* B2B mesh topology is used in AutoGrid5^{TM} with a *high inlet type* angle and *low outlet type* angle. The radial diffuser mesh consists of 638628 grid points with the following mesh quality criteria. The grid layout is shown in Figure D.6.

Table D.2: Radial diffuser (Diffuser 2) mesh quality criteria

	Mesh quality criteria	Radial diffuser mesh
Orthogonality	> 24˚	28.84˚
Aspect Ratio	< 2000	89.92
Expansion Ratio	< 2.5	1.88
Angular Deviation	< 40˚	44.72˚

Only 46 cells out of the possible 10714368 cells do not adhere to the angular deviation criteria. This amounts to $4.3 \cdot 10^{-4}$% of all the cells and is therefore considered acceptable. A FNMB mixing plane is created between 1 radial vane and 1 axial blade to connect the two non-matching mesh boundaries.

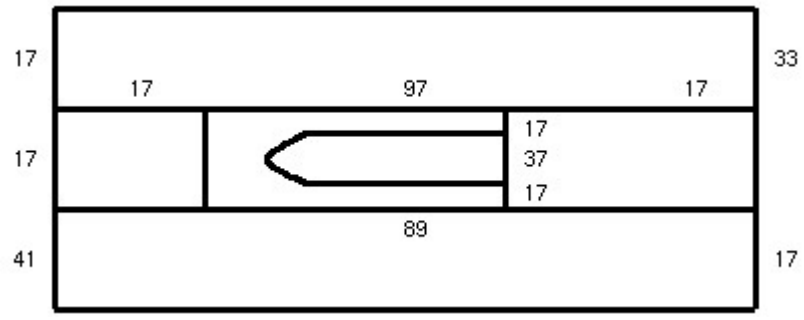

Figure D.6: Radial diffuser B2B grid layout

The axial blade mesh consists of a structured mesh with 57 flow paths from hub to shroud on the surfaces of revolution. The *default* B2B mesh topology is used in AutoGrid5™ with a *high inlet type* angle and *normal outlet type* angle. The axial blade grid layout is shown in Figure D.7 and its mesh consists of 893475 grid points with the following mesh quality criteria:

Table D.3: Axial blade mesh quality criteria

	Mesh quality criteria	Axial blade mesh
Orthogonality	> 24˚	30.5˚
Aspect Ratio	< 2000	100.56
Expansion Ratio	< 2.5	2.55
Angular Deviation	< 40˚	9.12˚

Only 79 cells out of the possible 10714368 cells do not adhere to the expansion ratio criteria. This amounts to $7.4 \cdot 10^{-4}$% of all the cells and is therefore considered acceptable.

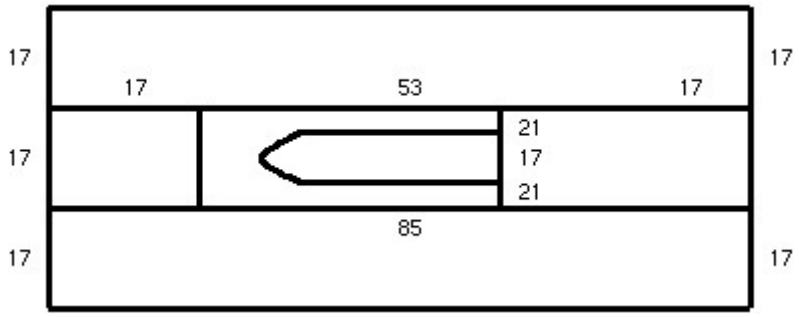

Figure D.7: Axial blade B2B grid layout

D.3. Diffuser 3 compressor mesh

The impeller mesh consists of 2333952 grid points with the following mesh quality criteria:

Table D.4: Impeller mesh quality criteria

	Mesh quality criteria	Impeller Mesh
Orthogonality	> 24˚	26.9˚
Aspect Ratio	< 2000	218.59
Expansion Ratio	< 2.5	2.81
Angular Deviation	< 40˚	16.77˚

1271 cells exceed the expansion ratio criteria of 2.5. This represents 0.01% of the total amount of cells and was found to be acceptable.

Diffuser 3 consists of 30 radial vanes with 30 downstream axial blades. Again only the radial vane and axial blade hub and shroud geometries are required by AutoGrid5^{TM}. The mesh for Diffuser 3 is created with 57 flow paths from hub to shroud on the surfaces of revolution. The *default* B2B mesh topology is used in AutoGrid5^{TM} with a *high inlet type* angle and *low outlet type* angle. The radial diffuser mesh consists of 744819 grid points with the following mesh quality criteria. The grid layout is shown in Figure D.8.

Table D.5: Radial diffuser (Diffuser 3) mesh quality criteria

	Mesh quality criteria	Radial diffuser mesh
Orthogonality	> 24˚	29.7˚
Aspect Ratio	< 2000	83.1
Expansion Ratio	< 2.5	2.1
Angular Deviation	< 40˚	8.41˚

A FNMB mixing plane is created between one radial vane and one axial blade to connect the two non-matching mesh boundaries.

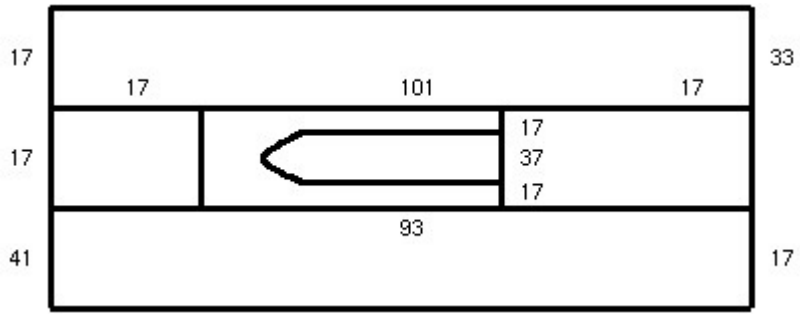

Figure D.8: Radial diffuser B2B grid layout

The axial blade mesh consists of a structured mesh with 57 flow paths from hub to shroud on the surfaces of revolution. The *default* B2B mesh topology is used in AutoGrid5™ with a *high inlet type* angle and *normal outlet type* angle. The axial blade grid layout is shown in Figure D.9 and its mesh consists of 1056495 grid points with the following mesh quality criteria:

Table D.6: Axial blade mesh quality criteria

	Mesh quality criteria	Axial blade mesh
Orthogonality	> 24˚	31.14˚
Aspect Ratio	< 2000	244.3
Expansion Ratio	< 2.5	2.49
Angular Deviation	< 40˚	12.42˚

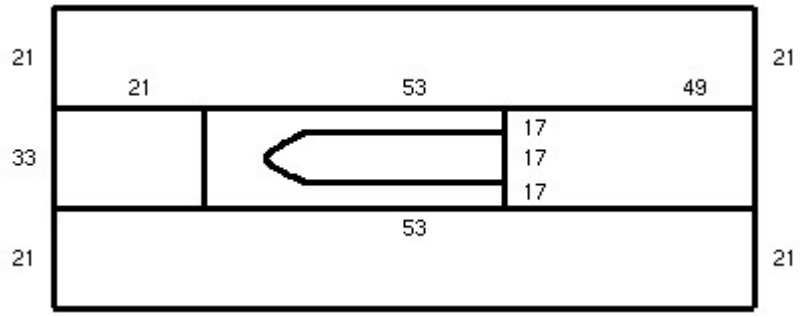

Figure D.9: Axial blade B2B grid layout

D.4. Diffuser 4 compressor mesh

The impeller mesh consists of 1713088 grid points with the following mesh quality criteria:

Table D.7: Impeller mesh quality criteria

	Mesh quality criteria	Impeller Mesh
Orthogonality	> 24˚	24.47˚
Aspect Ratio	< 2000	244.11
Expansion Ratio	< 2.5	2.7
Angular Deviation	< 40˚	10.51˚

430 of the 14861568 cells do not adhere to the expansion ratio criteria, this represents only $2.9 \cdot 10^{-3}$% of the total number of cells.

Diffuser 4 consists of 15 curved radial vanes with 30 downstream axial blades. The mesh for Diffuser 3 is created with 57 flow paths from hub to shroud on the surfaces of revolution. The *default* B2B mesh topology is used in AutoGrid5™ with a *high inlet type* angle and *low outlet type* angle. The radial diffuser mesh consists of 1302507 grid points with the following mesh quality criteria. The grid layout is shown in Figure D.10.

Table D.8: Radial diffuser (Diffuser 4) mesh quality criteria

	Mesh quality criteria	Radial diffuser mesh
Orthogonality	> 24˚	27˚
Aspect Ratio	< 2000	68.64
Expansion Ratio	< 2.5	2.33
Angular Deviation	< 40˚	13.75˚

A FNMB mixing plane is created between 1 radial vane and 2 axial blades to connect the non-matching mesh boundaries.

The axial blade mesh consists of a structured mesh with 57 flow paths from hub to shroud on the surfaces of revolution. The default B2B mesh topology is used in AutoGrid5™ with a high inlet type angle and normal outlet type angle.

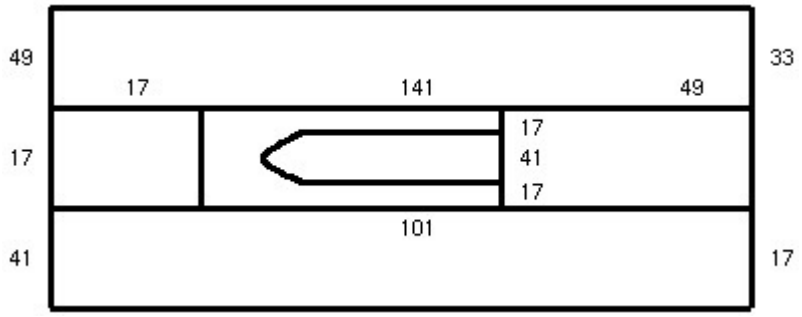

Figure D.10: Radial diffuser B2B grid layout

The axial blade grid layout is shown in Figure D.11 and its mesh consists of 2311350 grid points with the following mesh quality criteria:

Table D.9: Axial blade mesh quality criteria

	Mesh quality criteria	Radial diffuser mesh
Orthogonality	> 24˚	31.12˚
Aspect Ratio	< 2000	244.11
Expansion Ratio	< 2.5	1.56
Angular Deviation	< 40˚	8.83˚

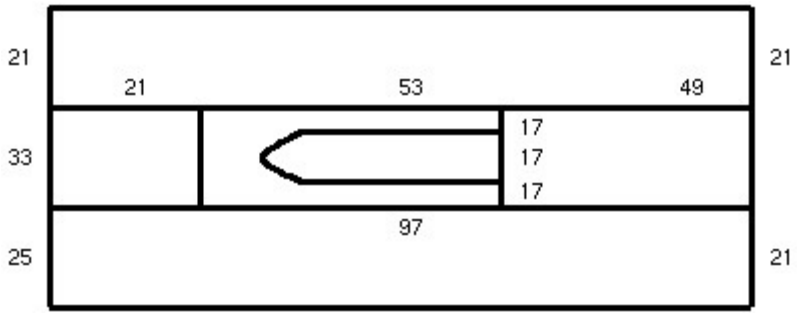

Figure D.11: Axial blade B2B grid layout

Mesh refinement

Indicated in Figures D.12, D.13 and D.14 is the original diffuser (Diffuser 1) compressor mesh B2B meridional views for the coarse (222), medium (111) and fine (000) mesh grid levels.

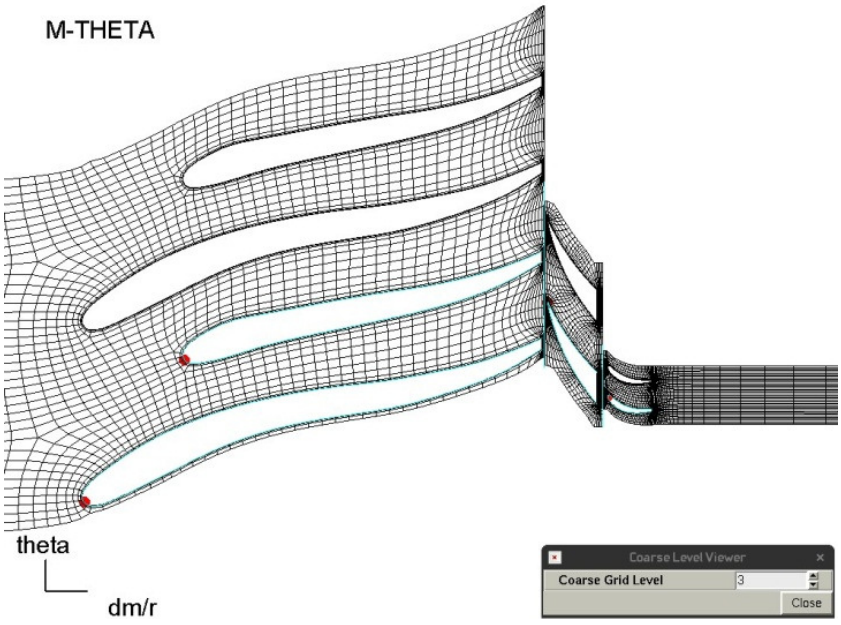

Figure D.12: Coarse (222) mesh layout

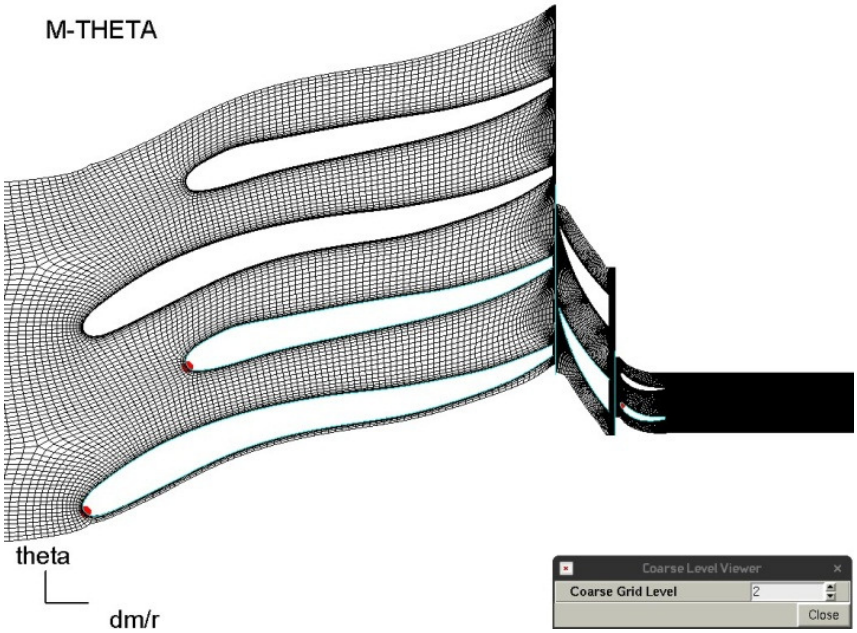

Figure D.13: Medium (111) mesh layout

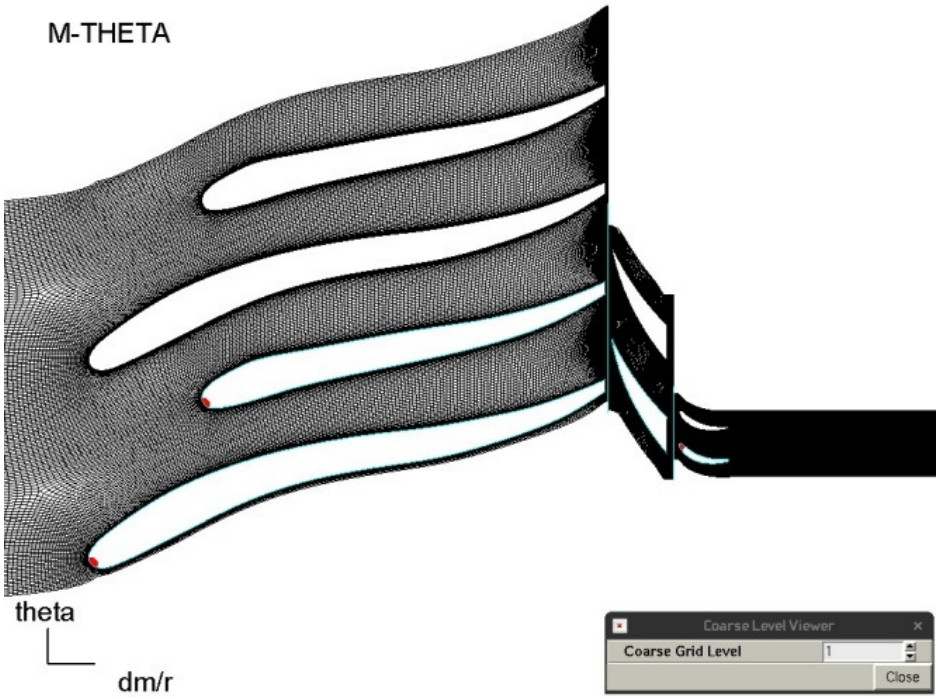

Figure D.14: Fine (000) mesh layout

D.5 Absolute velocity streamline distribution

The absolute velocity streamline vectors from the impeller tip to radial diffuser discharge of Diffuser 1 are indicated in Figures D.15 to D.19 at 20% span intervals from hub to shroud. The effect of a mismatched leading edge from hub to shroud can clearly be seen as the flow breaks away from the vane pressure or suction surfaces, resulting in a reduced flow area.

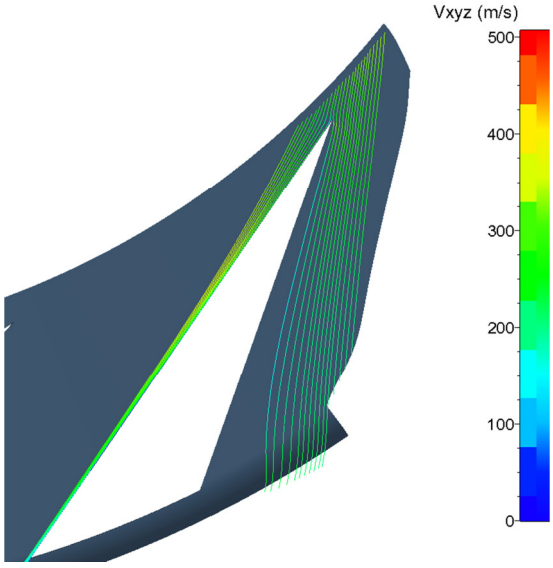

Figure D.15: 10% span

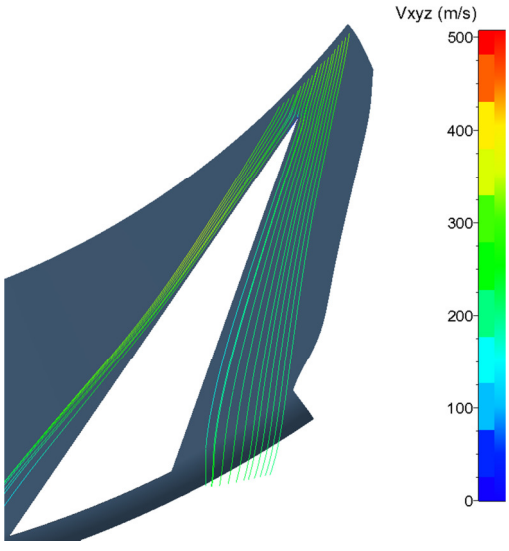

Figure D.16: 30% span

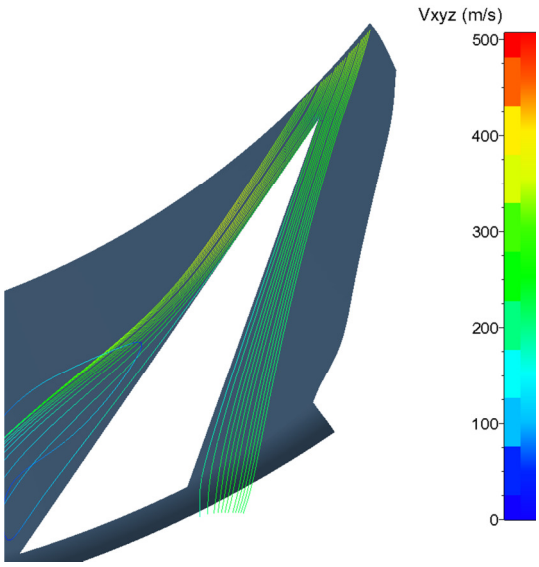

Figure D.17: 50% span

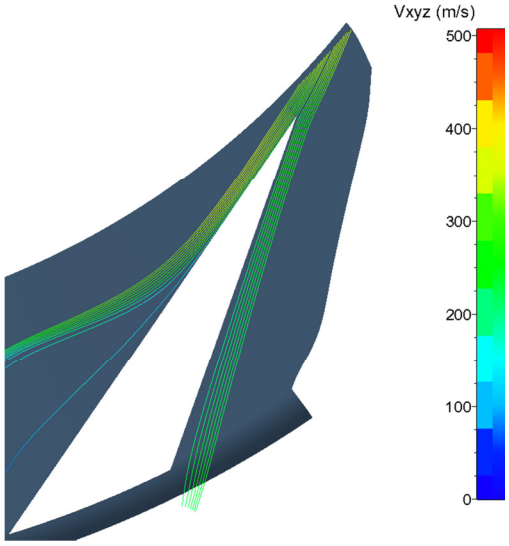

Figure D.18: 70% span

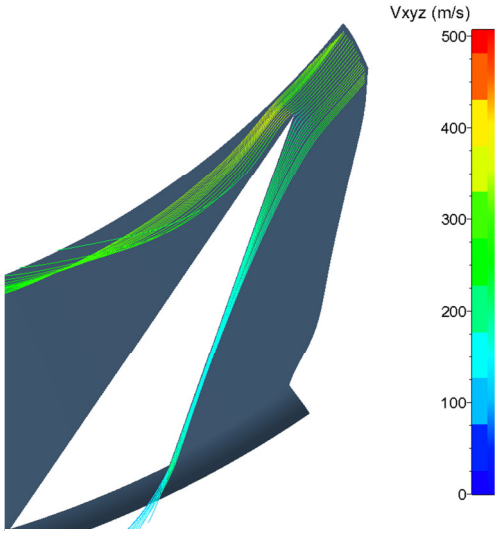

Figure D.19: 90% span

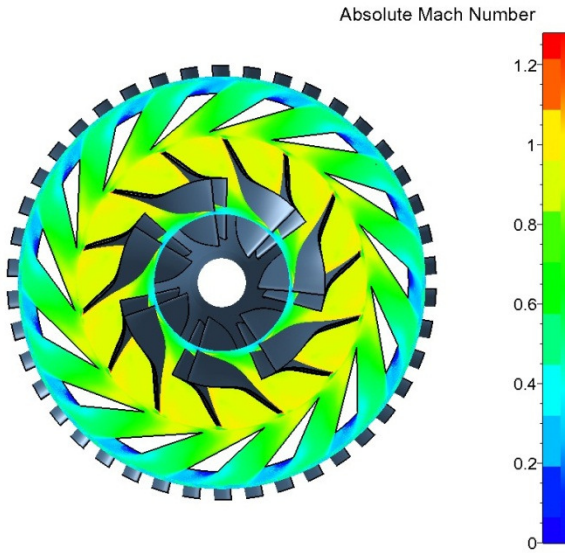

Figure D.20: Absolute Mach number distribution for Diffuser 1

The absolute Mach number as viewed in CFView™ for each diffuser is indicated in Figures D.20 to D.23 respectively.

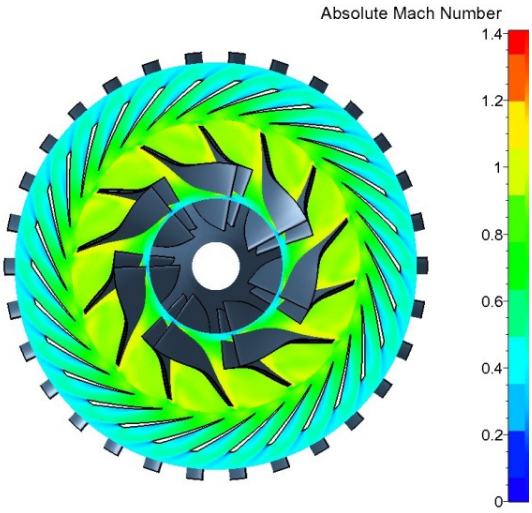

Figure D.21: Absolute Mach number distribution for Diffuser 2

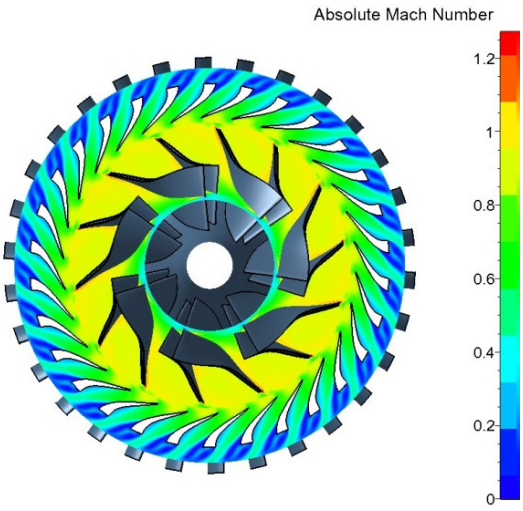

Figure D.22: Absolute Mach number distribution for Diffuser 3

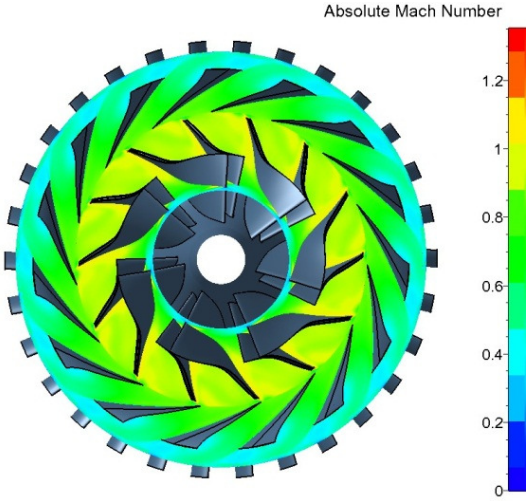

Figure D.23: Absolute Mach number distribution for Diffuser 4

APPENDIX E: EXPERIMENTAL DATA

The four diffuser geometries as well as the experimental procedure, calibration of the measuring equipment and experimental data for Diffusers 1, 2 and 3 are included in this Appendix.

E.1 Geometrical parameters

Table E.1 supplies the KKK K27.2 impeller geometry used for the numerical analyses.

Table E.1: KKK K27.2 Impeller geometry

			K27.2
Inlet	$r_{1,h}$	[mm]	9.1
	$r_{1,s}$	[mm]	26.1
	r_1	[mm]	19.5
	$\beta_{1,h}$	[˚]	56.3˚
	$\beta_{1,s}$	[˚]	21.8˚
	β_1	[˚]	40.0˚
	t_1	[mm]	0.8
	$\alpha_{C,1}$	[˚]	8.0˚
Throat	A_{th}	$[mm^2]$	1277
	β_{th}	[˚]	45.6˚
Tip	r_2	[mm]	35.0
	b_2	[mm]	6.0
	β_2	[˚]	59.6˚
	t_2	[mm]	1.0
	$\alpha_{C,2}$	[˚]	75˚
Overall	L_{FB}	[mm]	30.9
	L_{SB}	[mm]	26.48
	z_{FB}	[-]	7.0
	z_{SB}	[-]	7.0
	Fillet blockage	[-]	0.1

The major geometrical parameters of the 4 diffusers are indicated in Table E.2. Note that the blade radii and blade angles are taken on the mean stream surface.

Table E.2: Geometrical parameters of the 4 diffusers

		Diffuser 1	Diffuser 2	Diffuser 3	Diffuser 4
Inlet	r_3 (mm)	37.0	38.0	38.0	37.0
	β_3	18.54˚	21.50˚	23.60˚	22.00˚
	b_3 (mm)	6.00	6.20	6.20	6.00
	$t_{b,3}$ (mm)	0.01	0.01	0.20	0.01
Throat	r_{th} (mm)	40.0	39.3	39.4	39.0
	h_{th} (mm)	6.4	3.1	3.1	4.7
	A_{th} (mm^2)	581.9	586.5	576.9	591.2
Outlet	r_4 (mm)	46.5	48.0	48.0	46.5
	β_4	40.7˚	35.0˚	81.0˚	60.0˚
	b_4 (mm)	7.2	9.0	9.0	7.2
	$t_{b,4}$ (mm)	7.5	0.3	3.3	6.4
Overall	Number of Vanes	15	30	30	15
	L (mm)	18.5	21.4	16.1	19.5

E.2 Experimental procedure

The experimental procedure is identical for each test case and is briefly discussed below:

- Firstly, the gas turbine is assembled and mounted on the test bench.
- Turbine fuel (paraffin) is mixed with the appropriate amount of turbine oil for engine combustion and lubrication. The fuel mixture is used to lubricate the ceramic ball bearings during operation.
- The bell-mouth is attached to the engine cowl and sealed with an O-ring type rubber seal.
- The fuel pipes are connected to the engine fuel tubes through the bell-mouth.
- The HBM spider 8 data logger is set up with its appropriate input/output measuring equipment and connected to a personal computer for digital feedback and recording.
- The test facility is cleared of all objects that could pose a problem during engine tests and the laboratory's doors are closed to prevent any disturbed airflow into the engine.

- The Ground Support Unit, GSU, is turned on and a pre-run check is done, i.e. the fuel pump's voltage is adjusted, the bearings lubricated and the electric starter is checked.
- Ambient air conditions are measured in the laboratory. The HBM Spider software program, Catman, is started on the personal computer and all initial values are zeroed.
- The engine is then started using the GSU. It is started by an electric motor that spools the impeller up to a rotational speed of around 8 krpm, after which the fuel is injected into the combustion chamber and ignited by the glow plug. The impeller automatically spools up to a rotational speed of around 34 krpm. This is set as the engine's idling speed and is taken as 0% of maximum speed.
- For testing and engine performance comparisons the fuel pump voltage is firstly stepped up in steps of 10 percent from 0 to maximum voltage, i.e. 10 %, 20 %, 30 % etc. and then brought back down to idling speed (34 krpm). The impeller rotational speed is then stepped from 50 krpm to 120 krpm in 10 krpm steps. This is used as reference speeds for performance comparisons to numerical analyses. The speed is kept constant at each specific step interval until the flow has stabilized.
- The engine is then brought down to idling speed and shut down.
- All recorded performance data is stored on the personal computer and processed for further investigation and comparison.

E.3 Calibration of the measurement equipment

All measurement equipment that is calibrated is connected to a personal computer (PC) via a Spider8 data logger. Catman is the software program used on the PC to convert the voltage outputs supplied by the data logger to the required units, i.e. Pascal, kg etc. Catman records and saves the measured data that is used for further processing in Microsoft Excel.

Once the calibration of the measurement equipment is finished the Catman setup is saved and can be used for testing whenever it is required without having to recalibrate the measurement equipment before every test.

E.3.1 Pressure calibration

The four HBM P8AP 10 bar pressure transducers are connected to the Spider8 data logger and calibrated using an analog pressure gauge as seen in Figure E.1. Compressed air supplied at a steady rate to the pressure transducer and analog pressure gauge is used for the calibration procedure. The compressed air valve is connected to a Festo tube with a T-fitting that is connected on the one side to the pressure transducer and the other to the analog pressure gauge. The compressed air can be adjusted by opening or closing the feeding tap as required. The compressed air is stepped in 1 bar (100 kPa) steps up to 5 bar and the corresponding value measured by Catman is adjusted such that the user interface in Catman measures and displays the exact same pressure value as the analog gauge for each step. This procedure is performed for each pressure

transducer on a separate channel in Catman and saved. Each channel in Catman is linked to a specific output port on the Spider8 data logger.

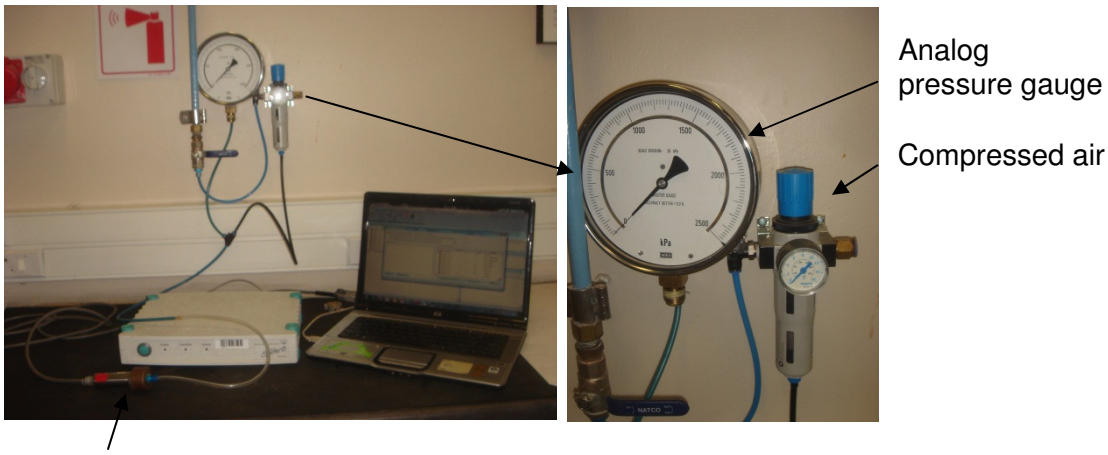

Figure E.1: Pressure transducer calibration setup

The HBM PD1/0.1 bar differential pressure transducer is calibrated in a similar fashion as described above. However, the differential pressure transducer has two pressure taps, namely a positive and negative tap. During calibration the positive tap is connected to the compressed air supply feed whilst the negative tap is left open to the atmosphere. The compressed air is stepped in 1 kPa steps and adjusted in Catman as required to match the analog pressure readings.

E.3.2 Thrust calibration

The HBM RSCC S-type 50 kg load cell (see Figure E.2) used to measure the engine thrust is calibrated by means of a spring loaded weight scale. The load cell is connected to the spider8 data logger and the displaced measurement data is displayed digitally on the Catman user interface. The one side of the spring loaded weight scale is connected to the runner bed whilst the other side is pulled. As the scale is pulled it provides a reading in kilogram which is used to adjust the load cell value in Catman. The scale is pulled in increasing steps of 1 kg, i.e. 1, 2, 3, 4 kg etc. The relationship between the voltage output and corresponding weight measurement is linear. Therefore the load cell is calibrated in 1 kg steps up to 6 kg.

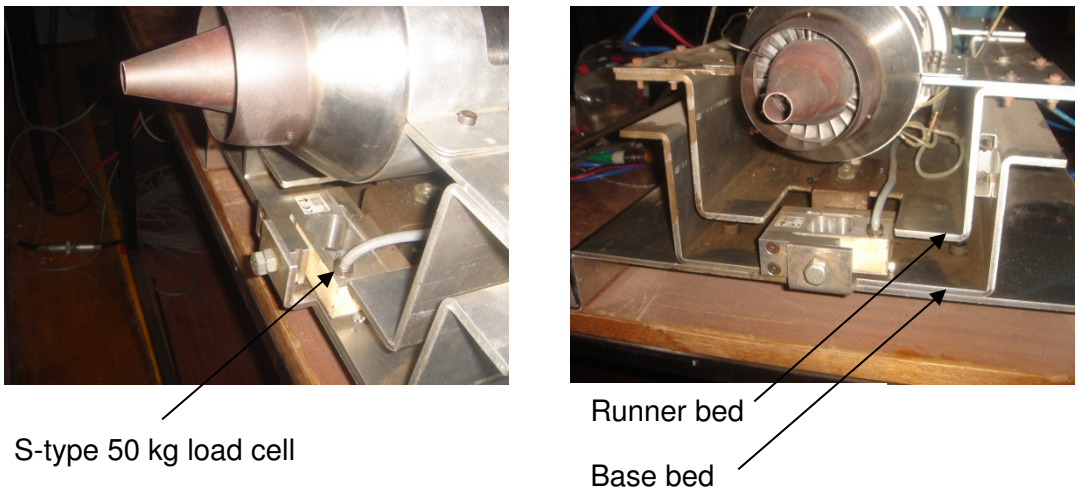

Figure E.2: Thrust measurement, *HBM RSCC S-type 50 kg load cell*

E.3.3 Temperature calibration

The K-type thermocouples used for temperature measurement are calibrated with a digital temperature probe. Each thermocouple is connected to a data acquisition (DAQ) logger which is connected to the PC. A heat gun is used to heat both the K-type thermocouple and the needle of the temperature probe simultaneously and the measurement displayed on the PC is adjusted such that the digital probe reading and K-type thermocouple outputs the same temperature values. Again a linear relationship exists between the voltage output and temperature measurement.

E.3.4 Fuel consumption calibration

The fuel consumption is measured by hanging a container with the turbine fuel from an HBM U2A 50 kg load cell. The load cell is calibrated by suspending various predefined weights from it. The suspended weight is increased by 1 kg weights and the corresponding output in Catman is adjusted accordingly to match the specified weight.

E.4 Experimental data

The experimental performance of the BMT 120 KS with the different diffuser configurations is indicated in the respective tables below. The rotational speed is kept constant at a specific speed until the flow has stabilized for each test run. The tabulated results are therefore averages of the “stabilized” flow results at each speed. The data logger records data every 0.02 seconds (50 Hz).

Table E.3: Experimental data of the original BMT 120 KS compressor (Diffuser 1)

RPM [krpm]	$\dot{m}$ [kg/s]	Static Pressure [kPa]			Thrust [N]	EGT [K]
		p_2	p_{th}	p_4		
50	0.102	101.39	113.379	116.708	13.45	635
60	0.123	119.42	124.618	127.301	18.96	615
70	0.146	126.441	134.773	139.191	26.34	605
80	0.171	135.468	148.027	153.923	35.34	597
90	0.199	146.569	165.73	173.328	47.89	600
100	0.230	159.177	188.403	197.936	63.91	615
110	0.260	173.379	217.031	228.223	83.28	643
120	0.288	189.366	250.687	262.405	107.34	703
125	0.296	194.319	261.703	273.870	117.42	736

Table E.4: Experimental data of the BMT 120 KS compressor with Diffuser 2

RPM	$\dot{m}$ [kg/s]	Static Pressure [kPa]			Thrust [N]	EGT [K]
		p_2	p_{th}	p_4		
50	0.102	112.313	112.154	115.361	12.65	528
60	0.124	118.679	117.743	124.141	18.42	510
70	0.146	125.528	124.909	134.773	25.83	500
80	0.174	135.144	136.075	150.890	36.49	499
90	0.198	144.780	147.521	167.313	47.7	500
100	0.229	156.453	168.186	190.948	63.66	492
110	0.258	168.597	190.631	219.263	83.23	520
120	0.286	178.894	223.329	253.618	107.92	610
125	0.297	181.003	242.443	269.947	120.84	669

Table E.5: Experimental data of the BMT 120 KS compressor with Diffuser 3

RPM	$\dot{m}$ [kg/s]	Static Pressure [kPa]			Thrust [N]	EGT [K]
		p_2	p_{th}	p_4		
50	0.106	111.667	113.246	116.708	13.97	501
60	0.128	118.054	120.821	127.255	20.95	522
70	0.149	125.061	129.796	138.436	27.25	520
80	0.178	135.373	143.575	156.480	39.11	513
90	0.201	144.240	156.604	173.479	50.51	528
100	0.232	157.065	179.064	198.608	67.92	545
110	0.261	169.377	204.569	227.953	86.76	584
120	0.285	179.327	233.089	257.786	108.73	643
125	0.296	182.853	248.928	273.742	120.87	730

APPENDIX F: 1-D COMPAERO PERFORMANCE PREDICTIONS

Chapter 5 involves the design procedures of a radial vaned diffuser at a certain design point. Included in this Appendix are "off-design performance" plots of each Diffuser as predicted by Aungier's (2000) 1-D program VDDESIGN. The plots supplied by VDDESIGN indicate both the pressure recovery coefficient (c_p) and loss coefficient (LC) as well as the design and stall points.

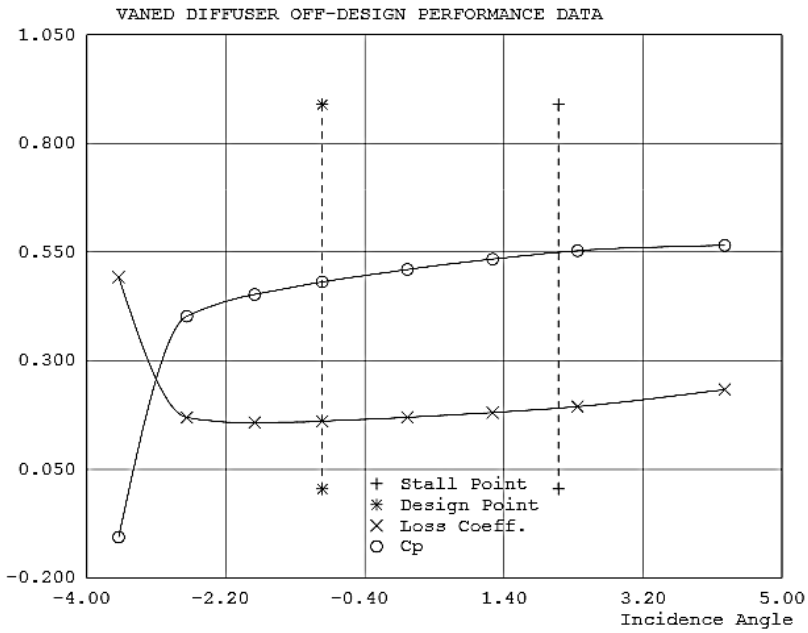

Figure F.1: Diffuser 1

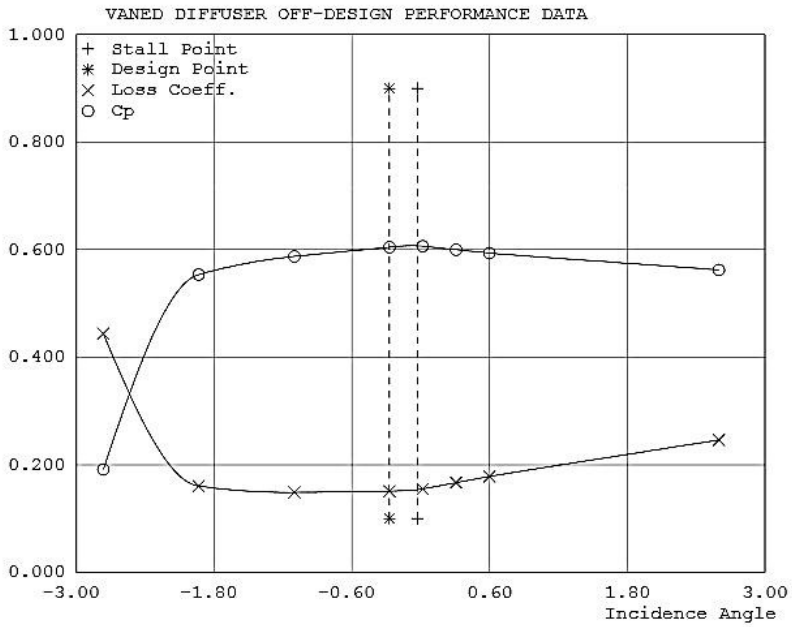

Figure F.2: Diffuser 2

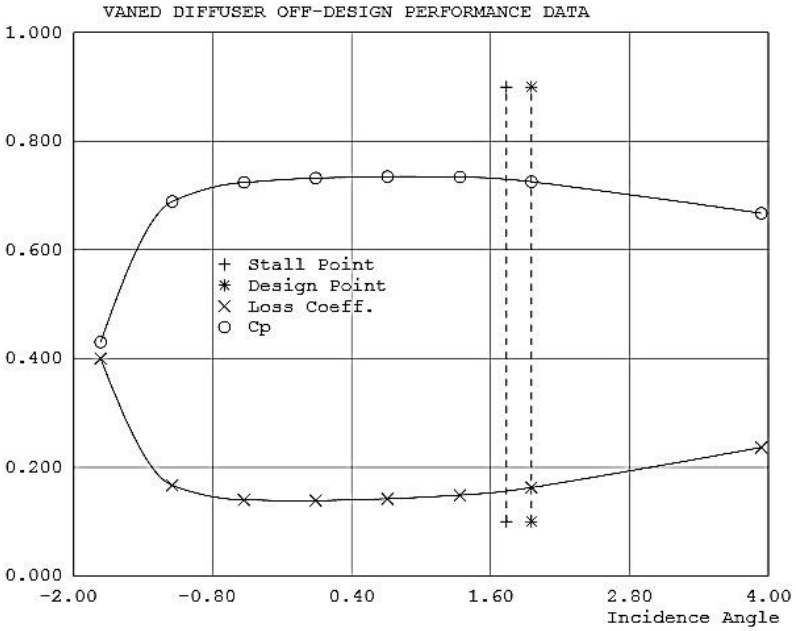

Figure F.3: Diffuser 3

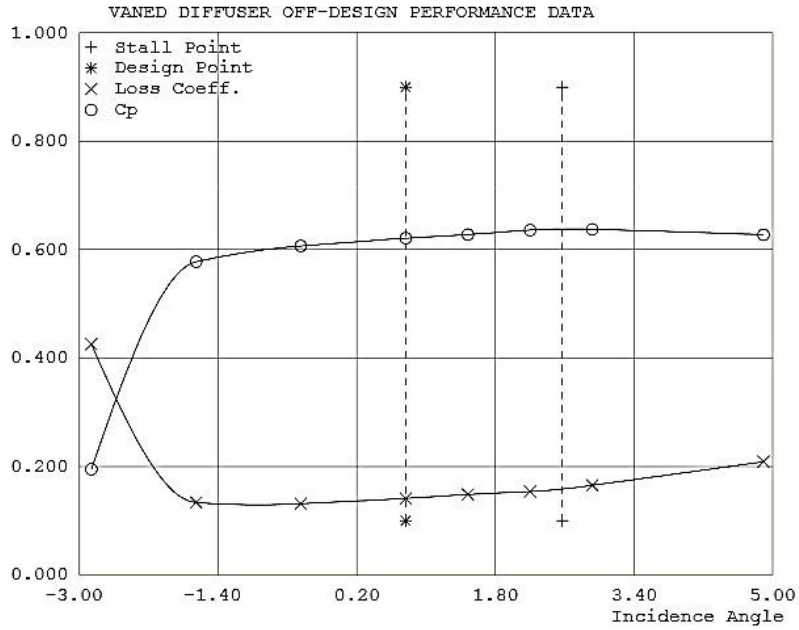

Figure F.4: Diffuser 4